Least Squares 3D Surface Matching

Devrim Akca

This publication is an edited version of:

Diss. ETH No. 17136

Least Squares 3D Surface Matching

A dissertation submitted to the
SWISS FEDERAL INSTITUTE OF TECHNOLOGY ZURICH

for the degree of
Doctor of Sciences

presented by

DEVRIM AKCA
M.Sc., Karadeniz Technical University

born 27th of May, 1975
citizen of Turkey

accepted on the recommendation of

Prof. Dr. Armin Grün, examiner
ETH Zurich, Switzerland

Prof. Dr. Orhan Altan, co-examiner
Istanbul Technical University, Turkey

Zurich 2007

To the wishes of my mother…

(1950-1983)

FOREWORD

Nowadays we dispose of various sensors and automated methods to produce large quantities of point clouds in a relatively short time. Very often an object is built up by a number of point cloud patches, which refer to different datums. Therefore the issue of co-registration of point clouds, representing 3D surfaces, is a serious topic in 3D modeling. Traditionally, some of the system manufacturers suggest to use specific tie points to be put into the scene for co-registration – a very tedious and not so accurate procedure. Progress was achieved with the ICP (Iterative Closest Point) technique, which uses only intrinsic surface information for co-registration. However, the ICP technique has a number of disadvantages, as described in this thesis, which the new method proposed here- 3D Least Squares Surface Matching- has overcome. 3D LS Surface Matching is a generalization of 2D LS image matching and has the same underlying ideas and concepts. In this context it is a generalization, like the previously developed 3D voxel cube matching and the line feature extraction techniques, both based on Least Squares Matching.

The author of this thesis has developed this technique, both in terms of theoretical penetration, practical and efficient computer implementation and has shown in quite a number of different application cases the power of this method.

The proposed method estimates the transformation parameters of one or more fully 3D search surfaces with respect to a template one, using the Generalized Gauss-Markoff model, minimizing the sum of squares of the Euclidean distances between the surfaces. It fully considers 3D geometry. The geometric relationship between the conjugate surface patches is defined as a 7-parameter 3D similarity transformation. This parameter space can be extended or reduced, as the situation demands.

In case of lack of sufficient geometric information the procedure may fail, e.g. in case of matching of two planes or spherical and cylindrical objects. An object surface may have some attribute information attached to it. Intensity and color are well known examples. Devrim Akca proposed an extension that can simultaneously match intensity information and geometry under a combined estimation model.

The mathematical model is flexible. Further conceptual extensions are given, as the Least Squares matching of 3D curves and matching of 3D curves or 3D sparse point clouds (e.g. ground control points) with a 3D surface. Additionally, a general framework for the simultaneous matching and georeferencing of multiple 3D surfaces with their intensity information has been formulated and will be further developed in the near future.

As evidenced by the many projects shown in this thesis the method works fine under a great variety of different conditions (use of satellite, aerial and terrestrial images, structured light systems, laserscanners, very dense and sparse point clouds, integrated image intensity data, simultaneous georeferencing and multi-patch matching).

The method of Multi-Patch 3D Least Squares Surface and Intensity Matching is a very substantial contribution of photogrammetry to the very broad and general problem of 3D Modeling.

Devrim Akca has researched, tested and applied this technique in an exemplary and excellent way. During all the time of hard and diligent work, which also included some other, smaller R&D projects, Devrim has never lost his ambitions and always showed great optimism and dedication. He was always a competent, friendly and solidary team-player. For all this I would like to congratulate him very much!

It is to be expected that this work will serve as a valuable reference for all experts concerned with 3D modeling for quite some years to come.

Zurich, May 2007   Prof. Dr. Armin Gruen

ABSTRACT

Laser scanners can measure directly 3D coordinates of huge amounts of points in a short time period. Most of them also provide an intensity value for every point. This abundant data can be efficiently used to model the scene. In many cases, the object has to be scanned from different viewpoints in order to completely reconstruct it. Because each scan has its own local coordinate system, all the different pointclouds must be transformed into a common system. This procedure is usually referred to as co-registration. Actually, the co-registration is not a problem specific to the laser scanner domain. Also in photogrammetry, we face many similar problems.

The automatic co-registration of pointclouds, representing 3D surfaces, is a relevant problem in 3D modeling. This multiple registration problem can be defined as a surface matching task. In photogrammetry, surface matching was first touched by Gruen (1985a) as a straight extension of the Least Squares image matching. This thesis work gives a generalization of this 2D technique to the 3D surface matching problem. The proposed method estimates the transformation parameters of one or more fully 3D search surfaces with respect to a template one, using the Generalized Gauss-Markoff model, minimizing the sum of squares of the Euclidean distances between the surfaces. It fully considers 3D geometry.

An observation equation is written for each surface element on the template surface patch, i.e. for each sampled point. Each equation functionally relates the observations of the template to the parameters of search surface. The constant term of the adjustment is given by the observation vector whose elements are the Euclidean distances between the template and search surface elements. The matching is achieved by Least Squares minimization of a goal function, which measures the Euclidean distances between the surfaces. The final location of the search surface is estimated with respect to an initial state. The geometric relationship between the conjugate surface patches is defined as a 7-parameter 3D similarity transformation. This parameter space can be extended or reduced, as the situation demands it. Since the functional model is non-linear, the system is linearized by Taylor expansion. The numerical derivative terms are defined as surface normals. The unknown transformation parameters are treated as stochastic quantities using proper a priori weights. This extension of the mathematical model gives control over the estimation parameters. The solution is iterative. After the joint system is solved, the search surface is transformed to a new state using the updated set of transformation parameters, and the design matrix and the discrepancies vector are re-evaluated. The iteration stops if each element of the alteration vector falls below a certain limit.

Besides the mathematical model of the procedure, a comprehensive discussion is given about the implementation details, precision and reliability issues, and convergence behavior. Special attention is paid to the computational aspects. Two strategies in order to decrease the computation time were implemented. The main portion of the computational complexity is to search the correspondent elements between the surfaces, whereas the adjustment part is a small system, and is quickly solved using Cholesky decomposition followed by back-substitution. A rapid space partitioning method is given for searching the correspondences. It is a 3D boxing structure combined with a hierarchical local and adaptive nearest neighborhood search. The local neighborhood is hierarchically updated during the iteration.

The second acceleration strategy is simultaneous matching of sub-surface patches, which are selected in cooperative surface areas. They are joined to the system by the same 3D transformation parameters. The individual patches may not include sufficient information for the matching of whole surfaces, but together they provide a computationally effective solution, since they consist of only relevant information rather than using the full data set.

In case of lack of sufficient geometric information the procedure may fail, e.g. in case of matching of two planes or spherical objects. An object surface may have some attribute information attached to it. Temperature, intensity, and color are well known examples. Most of the laser scanners can supply intensity information in addition to Cartesian coordinates for each point. We propose an extension that

can simultaneously match intensity information and geometry under a combined estimation model. In this approach the intensity image of the pointcloud also contributes observation equations to the system, considering the intensities as supplementary information to the range image.

The mathematical model is flexible. Further conceptual extensions are given as the Least Squares matching of 3D curves and matching of 3D curves or 3D sparse points (e.g. ground control points) with a 3D surface. Additionally, a general framework for the simultaneous matching and georeferencing of multiple 3D surfaces with their intensity information is formulated.

The method derives its mathematical strength from the Least Squares matching concept and offers a high level of flexibility for many kinds of 3D surface correspondence problems. The experiments demonstrate the capabilities of the basic method and the extensions.

ZUSAMMENFASSUNG

Laserscanning ermöglicht die direkte Bestimmung einer grossen Anzahl von 3D Koordinaten in kurzer Zeit, zusätzlich liefern viele dieser Systeme einen Intensitätswert zu jedem gemessenen Punkt. Die so erzeugte Fülle von Informationen wird genutzt, um den aufgenommenen Raum effizient zu modellieren. Für eine vollständige Rekonstruktion des erfassten Raums ist es notwendig, das zu erfassende Objekt von unterschiedlichen Standpunkten aus aufzunehmen. Da jeder Scan in einem eigenen Koordinatensystem vorliegt, ist es notwendig, alle erfassten Punktwolken in ein einheitliches System zu überführen. Dieser Vorgang wird als Co-Registrierung bezeichnet. Dies ist jedoch keine spezifisches Fall des Laserscannings, auch in der Photogrammetrie steht man diesem Problem in vielen Fällen gegenüber.

Die automatische Co-Registrierung von Punktwolken, welche 3D Flächen repräsentieren, ist eine wichtige Aufgabenstellung im Zuge der Modellierung. Dieses Problem der Mehrfachregistrierung kann als Surface-Matching Problem behandelt werden. Im Rahmen der Photogrammetrie wurde diese Aufgabe zum ersten Mal von Grün (1985a), als direkte Erweiterung des Least-Squares Image Matching erwähnt.

Die hier präsentierte Arbeit befasst sich mit der Erweiterung dieses zweidimensionalen Ansatzes, hin zu einem Matchingverfahren dreidimensionaler Flächen. Die hier vorgestellte Methode bestimmt die Transformationsparameter einer oder mehrerer dreidimensionaler Flächen bezüglich einer Referenzfläche (Template), unter Verwendung des allgemeinen Gauss-Markoff Modells, welchem die Minimierung der Summe der Quadrate, des euklidischen Abstandes zwischen den Flächen zugrunde legt. Hierbei wird vollumfänglich die dreidimensionale Information des Objektes berücksichtigt.

Für jedes Element der Referenzfläche, z.B. für jeden Punkt, ergibt sich eine Beobachtungsgleichung. Jede dieser Gleichungen beschreibt den Zusammenhang zwischen Beobachtungen der Referenzfläche und den Transformationsparametern der anzupassenden Fläche (Search-Surface). Das Absolutglied der Ausgleichung ist durch den Beobachtungsvektor gegeben, dessen Elemente den euklidischen Distanzen zwischen den Elementen der Referenzfläche und denen der anzupassender Fläche entsprechen. Das Matching wird mittels Minimierung der Zielfunktion nach kleinsten Quadraten durchgeführt, welches die euklidischen Distanzen zwischen den Oberflächen beschreibt. Die Endposition der anzupassenden Fläche wird bezüglich eines Startwertes bestimmt. Der geometrische Zusammenhang zwischen konjugierten Flächen wird mittels einer 7-Parameter Ähnlichkeitstransformation beschrieben. Dieser Parameterraum kann je nach Anforderung erweitert oder reduziert werden. Das verwendete funktionale Modell ist nichtlinear, somit ist eine Linearisierung nach Taylor notwendig. Die numerisch abgeleiteten Terme sind als Flächennormale definiert. Die unbekannten Transformationsparameter werden als stochastische Grössen mit geeigneter Gewichtung beschrieben. Diese Erweiterung des mathematischen Modells ermöglicht eine bessere Kontrolle über die zu bestimmenden Parameter. Die Bestimmung der Parameter erfolgt iterativ. Nach jeder Lösung des Systems wird die anzupassende Fläche, mittels der bestimmten Parameter, in ihre neue Lage transformiert und die Designmatrix sowie der Vektor der Verbesserungen neu bestimmt. Dieser Iterationsvorgang wird beendet, wenn jedes Element des Unbekanntenvektors einen bestimmten Grenzwert unterschreitet.

Neben dem mathematischen Modell werden Details der Implementation, Präzision, Zuverlässigkeit und des Konvergenzverhaltens ausführlich diskutiert. Besonderes Augenmerk wird hier auf rechentechnische Aspekte gelegt. Um eine Reduktion der Rechenzeit zu erzielen, wurden zwei verschiedene Berechnungsverfahren implementiert. Der grösste Teil des Rechenaufwandes wird für die Suche nach korrespondierenden Elementen zwischen den Oberflächen verwendet, wohingegen die Ausgleichung selbst nur den kleineren Teil einnimmt. Die Ausgleichung wurde mittels Cholesky Algorithmus sehr effizient gelöst. Zum Auffinden der korrespondierenden Oberflächenelemente wurde eine effiziente Unterteilung des Objektraumes durchgeführt. Diese basiert auf einer 3D-Box Struktur

mit hierarchischer lokalen und adaptiver Nearest Neighborhood Suche. Die lokalen Nachbarschaften werden während der Iteration hierarchisch aktualisiert.

Eine weitere Möglichkeit besteht darin, lediglich Teile des Überlappungsbereichs zu nutzen, wobei diese Teile aus kooperativen Teilen des Gesamtmodells stammen. Diese einzelnen Unterteile enthalten unter Umständen nicht genügend Informationen um die gesamten Flächen zu registrieren, jedoch ergibt sich aus der Kombination der einzelnen Lösungen eine korrekte und effektive Lösung des Problems, da die Teilflächen nur relevante Informationen im Gegensatz zur gesamten vorhandenen Fläche aufweisen.

Im Fall fehlender geometrischer Information ist jedoch ein Fehlschlagen des Algorithmus möglich, z.B. beim Matching zweier Ebenen oder Kugeln. Einer Oberfläche kann zusätzliche Informationen enthalten. Temperatur, Intensität und Farbe sind einige der bekanntesten. Die meisten Laserscanner können Intensitätsinformationen bezüglich eines kartesischen Koordinatensystems für jeden gemessenen Punkt zur Verfügung stellen. Wir erweiterten unseren Ansatz, hin zu einer simultanen Auswertung von Intensitätsinformationen und Geometrie, in einem kombinierten mathematischen Modell. Bei diesem Ansatz tragen die Intensitätsbilder, als zusätzliche Information neben den eigentlichen Daten aus dem Laserscanning, weitere Beobachtungsgleichungen zur Ausgleichung bei.

Das vorgestellte mathematische Modell ist flexibel. Konzeptionelle Erweiterungen, wie das Least-Squares Matching von 3D Kurven, sowie das Matching von 3D Kurven oder 3D Punkten (z.B. Passpunkten) bezüglich einer 3D Oberfläche werden erläutert. Zusätzlich wurde das Grundgerüst für simultanes matching und georeferenzieren von mehreren 3D Oberflächen unter Nutzung von Intensitätsinformationen formuliert.

Die dargestellte Methodik erhält ihre mathematische Strenge durch die Ausgleichung nach kleinsten Quadraten und weist eine hohe Flexibilität zur Anwendung auf viele Arten von dreidimensionalen Flächenkorrespondenzproblemen auf. Die aufgezeigten Beispiele spiegeln die Möglichkeiten der grundlegenden Methode und der Erweiterungen wieder.

TABLE OF CONTENTS

LIST OF FIGURES

LIST OF TABLES

1

INTRODUCTION

1.1. Motivation

For 3D object modeling data acquisition must be performed from different standpoints. The derived local pointclouds (or surfaces) must be transformed into a common coordinate system. This procedure is usually referred to as co-registration.

In practice special targets, provided by the terrestrial laserscanning vendors (e.g. Zoller+Fröhlich, Leica, Riegl), are mostly used for co-registration of pointclouds. However, such a strategy has several deficiencies with respect to fieldwork time, personnel and equipment costs, and accuracy. In a recent study, Sternberg et al. (2004) reported that registration and geodetic measurement parts comprise 10-20% of the whole project time. In another study, a collapsed 1000-car parking garage was documented in order to assess the damage and structural soundness of the structure. The scanning took 3 days, while the conventional survey of the control points required 2 days (Greaves, 2005). In our work at Pinchango Alto (details given in Chapter 6.3.3), two persons set the targets to the field and measured with RTK-GPS in 1½ days.

Not only fieldwork time but also accuracy is another important concern. The target based registration methods cannot exploit the full accuracy potential of the data. The geodetic measurement naturally introduces some error, which might exceed the internal error of the scanner instrument. In addition, the targets must be kept stable during the whole scanning campaign. This might be inconvenient with the scanning works stretching over more than one day.

Surface based registration techniques stand as efficient and versatile alternative to the target based techniques. They simply bring the strenuous additional fieldwork of the registration task to the computer in the office while optimizing the project cost and duration and achieving a better accuracy.

In the last decade, the surface based registration techniques have been studied extensively. It is still an active research area. An exhaustive literature review, which gives a large number of research activities on the topic, given in the next chapter, demonstrates the relevance of the problem. Co-registration is crucially needed wherever spatially related data sets can be described as surfaces and have to be transformed to each other. Examples can be given in medicine, computer graphics, animation, cartography, virtual reality, industrial inspection and quality control, spatial data fusion, cultural heritage, photogrammetry, etc.

1.2. Research aims

The Least Squares matching (LSM) concept had been developed in parallel by Gruen (1984; 1985a), Ackermann (1984) and Pertl (1984). It has been applied to many different types of measurement and feature extraction problems due to its high level of flexibility and its powerful mathematical model: adaptive Least Squares image matching (Gruen, 1984; Gruen, 1985a), geometrically constrained multiphoto matching (Gruen and Baltsavias, 1988), image edge matching (Gruen and Stallmann, 1991), multiple patch matching with 2D images (Gruen, 1985b), multiple cuboid (voxel) matching with 3D images (Maas, 1994; Maas and Gruen, 1995), globally enforced Least Squares template matching (Gruen and Agouris, 1994), Least Squares B-spline (LSB) Snakes (Gruen and Li, 1996). For a detailed survey, the author refers to Gruen (1996).

If 3D pointclouds derived by any device or method represent an object surface, the problem should be defined as a surface matching problem instead of 3D pointcloud matching. In particular, we treat it as

Least Squares matching of overlapping 3D surfaces, which are digitized/sampled point by point using a laser scanner device, the photogrammetric method or other surface measurement techniques. This definition allows us to find a more general solution for the problem as well as to establish a flexible mathematical model in the context of the Least Squares matching.

The mathematical model is aimed to be a generalization of the Least Squares image matching, in particular the method given by Gruen (1984; 1985a). The Least Squares image matching estimates the location of a synthetic or natural template image patch on a search image patch, modifying the search patch by an affine transformation, minimizing the sum of squares of the grey level differences between the image patches. Geometric and radiometric differences are simultaneously modeled via image shaping parameters and radiometric corrections.

One decade after, Maas (1994), Maas and Gruen (1995) introduced a straightforward extension of the 2D technique to 3D voxel space, working with volume data rather than image data. The so-called Least Squares cuboid matching method matches and tracks 3D cuboids in 3D image sequences. It has been shown to be very useful in a 3D LIF (laser-induced fluorescence) research project at ETH Zurich. The goal of this project was the measurement and analysis of chemical mixing (reaction) processes under turbulent flow.

This thesis work attempts to give another straightforward extension of the Least Squares matching concept for the 3D surface matching case. The basic estimation model is derived based on those two inspiring works that are Least Squares image matching and Least Squares cuboid matching. It conceptually stands between these two approaches.

Although the registration of 3D pointclouds is a very active research area in many disciplines, there is still the need for a contribution that responds favorably to the following aspects: matching of data sets with higher order spatial transformation models, matching of full 3D surfaces (as opposed to 2.5D), a rigorous mathematical formulation for high accuracy demands, a flexible model for further algorithmic extensions, mechanisms and statistical tools for internal quality control, and capability of matching of data sets in different quality and resolution.

3D object modeling can be a cumbersome task in many cases. The object might be very large or complex, which needs many standpoints for data acquisition. These multiple surfaces should be co-registered under one reference system efficiently, accurately and simultaneously. Some individual pointclouds might not contains sufficient surface information, e.g. for plane or spherical parts of an object surface. The problem can be overcome, if the intensity or color information of object surface is added to the estimation procedure appropriately. The georeferencing, which is the procedure to transform the spatial data from a local system to a higher order object coordinate system, might crucially be needed. As a consequence, we notice that a fully satisfying general solution has still to be found.

This thesis aims to achieve these goals by proposing a method based on 3D Least Squares matching.

1.3. Overview of the thesis contents

Chapter 2 gives an extensive review of previous work on surface matching. It has been classified according to early work on surface matching, acceleration strategies, multiple surface matching, approaches in terrain modeling, combined matching of surface geometry and attributes, and 3D curve matching.

Chapter 3 introduces the basic mathematical model. It is an algorithm for the Least Squares matching of overlapping 3D surfaces, called Least Squares 3D surface matching (LS3D). The LS3D estimates the transformation parameters of one or more fully 3D search surfaces with respect to a template one, using the Generalized Gauss-Markoff model, minimizing the sum of squares of the Euclidean distances between the surfaces. This formulation gives the opportunity of matching arbitrarily oriented 3D surfaces simultaneously, without using explicit tie points. The geometric relationship between the conjugate surfaces is defined as a 7-parameter 3D similarity transformation. This parameter space can be extended or reduced, as the situation demands it. The unknown transformation parameters are treated as stochastic quantities using proper a priori weights.

Apart from the basic estimation model, Chapter 3 touches many execution aspects: surface representation, calculation of numerical derivatives, statistical analysis tools of the estimated parameters, error detection, convergence behavior, computational aspects, and a discussion on the Generalized Gauss-Markoff and Levenberg-Marquardt estimation models with respect to their statistical soundness.

Chapter 3.8 explains the employed acceleration strategies in order to optimize the run-time. The first strategy is a rapid method for searching the correspondences. We opt for a space partitioning method given by Chetverikov (1991), called boxing. In the original publication, it was given for 2D point sets. We straightforwardly extend it to the 3D case. We combine our 3D boxing structure with a hierarchical local and adaptive nearest neighborhood search. The second acceleration strategy is the simultaneous matching of sub-surface patches, which are selected in cooperative surface areas. It provides a computationally effective solution, since it matches only relevant multi-subpatches rather than the whole overlapping areas.

When more than two pointclouds with multiple overlaps exist, we adopt a two step solution. First, pairwise LS3D matchings are run on every overlapping pairs and a subset of point correspondences is saved to separate files. In the global registration step, all these files are passed to a block adjustment by independent models procedure (Ackermann et al., 1973), which is a well known orientation procedure in photogrammetry. Details are given in Chapter 3.9.

Chapter 4 explains the combined matching approach. When the object surface lacks sufficient geometric information, i.e. homogeneity or isotropicity of curvatures, the basic algorithm will either fail or find a side minimum. We propose an extension to the basic algorithm in which available attribute information, e.g. intensity, color, temperature, etc., is used to form quasisurfaces in addition to the actual ones. The matching is performed by simultaneous use of surface geometry and attribute information under a combined estimation model.

Chapter 5 gives further conceptual extensions: Least Squares matching of 3D curves, matching of 3D curves or 3D sparse points (e.g. ground control points) with a 3D surface, and a general framework, which can perform the multiple surface matching, intensity matching and georeferencing tasks simultaneously. Although these extensions have not been implemented and tested yet, they are given here due to their prospective applications, especially in 3D modeling, quality control, and spatial data orientation studies.

The basic algorithm and all other extensions (except the ones given in Chapter 5) were implemented as a stand-alone MS Windows application with a graphical user interface. The software package was developed with the C++ programming language and the OpenGL graphics application programming interface (API) under C++Builder 5 (Borland Inc.) integrated development environment (IDE).

We verified the capabilities of the method in several applications. Some of them are given in Chapter 6: site and object modeling, cultural heritage studies, terrain modeling, fusion of SRTM C-Band Digital Elevation Models (DEM) with local DEMs (SRTM TerrainScape project in cooperation with Swissphoto AG, Zurich), accuracy assessment of automatically generated Digital Surface Models (DSM) by DMC digital airborne camera, change detection of forestry areas, validation of accuracy potential of the SRTM C-Band DEMs.

2

REVIEW OF PREVIOUS WORK ON SURFACE MATCHING

2.1. Early work on surface matching

In the literature, several attempts have been described concerning the registration of 3D pointclouds. One of the most popular methods is the Iterative Closest Point (ICP) algorithm developed by Besl and McKay (1992), Chen and Medioni (1992) and Zhang (1994). The ICP is based on the search for pairs of nearest points in two data sets and estimates the rigid body transformation that aligns them. Then, the rigid body transformation is applied to the points of one set and the procedure is iterated until convergence is achieved.

In Besl and McKay (1992) and Zhang (1994) the ICP requires every point in one surface to have a corresponding point on the other surface. Alternatively, the distance between the transformed points in one surface and the corresponding tangent planes on the other surface was used as a registration evaluation function (Chen and Medioni, 1992; Bergevin et al., 1996; Pulli, 1999). The point-to-tangent plane approach gives a better registration accuracy than the point-to-point approach. It was originally proposed by Potmesil (1983).

The outliers due to erroneous measurements (e.g. points on the object silhouette) and occlusions may significantly impair the quality of the registration. The following strategies have been proposed for localization and elimination of outliers and occlusions: rejection of pairs based on predefined (constant) distance threshold (Turk and Levoy, 1994; Zhang, 1994; Blais and Levine, 1995; Guehring, 2001; Dalley and Flynn, 2002) or variable distance thresholds adapted from Robust Estimation Methods (Masuda and Yokoya, 1995; Neugebauer, 1997; Fitzgibbon, 2001; Gruen and Akca, 2005), rejection of pairs based on the orientation threshold for surface normals (Zhang, 1994; Guehring, 2001), rejection of pairs containing points on mesh boundaries (Turk and Levoy, 1994; Pulli, 1999; Guehring, 2001), rejection of pairs based on the reciprocal correspondence (Pajdla and Van Gool, 1995), rejection of the worst n% of pairs (Pulli, 1999), employing the least median of squares (LMS or LMedS) (Masuda and Yokoya, 1995) and the least trimmed squares estimators (Chetverikov et al., 2005).

In the ICP algorithm and its variants, main emphasis is put on the estimation of a 6-parameter rigid body transformation without uniform scale factor. There are a few reports in which higher order geometric transformations are formulated (Feldmar and Ayache, 1996; Szeliski and Lavallee, 1996).

The parameters of the rigid body transformation are generally estimated by the use of closed-form solutions, mainly singular value decomposition (SVD) (Arun et al., 1987; Horn et al., 1988) and quaternion methods (Faugeras and Hebert, 1986; Horn, 1987). Eggert et al. (1997) and Williams et al. (1999) provide an extensive review and comparison. The closed-form solutions can estimate only 6 parameters of a rigid body transformation or 7 parameters of a similarity transformation.

The closed-form solutions cannot fully consider the statistical point error models. Zhang (1994) and Dorai et al. (1997) weighted the individual points based on a priori noise information. Williams et al. (1999), Guehring (2001) and Okatani and Deguchi (2002) proposed methods that can model the anisotropic point errors.

The gradient descent type of algorithms can support full stochastic models for measurement errors, and assure a substantially lower number of iterations than the ICP variants (Szeliski and Lavallee,

1996; Neugebauer, 1997; Fitzgibbon, 2001). The Levenberg-Marquardt method is usually adopted for the estimation.

Several reviews and comparison studies on surface registration methods are available in the literature (Jokinen and Haggren, 1998; Williams et al., 1999; Campbell and Flynn, 2001; Rusinkiewicz and Levoy, 2001; Gruen and Akca, 2005).

2.2. Related work on acceleration strategies

The ICP, and in general all surface registration methods, require heavy computations. The computational complexity of the original algorithm is of order $O(n^2)$, which can take a lot of time when working with real-size data sets. Using the high performance computers or parallel computing systems (Langis et al., 2001) was proposed as a solution in order to reduce the processing time. However, the main research emphasize has been put on hardware-independent solutions.

The ICP algorithm always converges monotonically to a local minimum with respect to the mean-square distance objective function (Besl and McKay, 1992). This monotonic convergence behavior leads to slow convergence, which means typically 30-50 iterations (Besl and McKay, 1992; Zhang, 1994; Cunnington and Stoddart, 1999; Pottmann et al., 2004), and even more in extreme cases. Reducing the number of iterations is an option to accelerate the ICP. In their original publication Besl and McKay (1992) proposed an accelerated version of the ICP which updates the parameter vector using linear or parabolic types of extrapolations. Pottmann et al. (2004) forced the parameter vector to a helical motion in the parameter space. Both methods change the convergence from monotonic to quadratic type. However, manipulating the parameter vector without any statistical justification may cause two dangers: over-shooting the true solution, and deteriorating the orthogonality of the rotation matrix. The gradient descent types of algorithms guarantee the true quadratic convergence (Szeliski and Lavallee, 1996; Neugebauer, 1997; Fitzgibbon, 2001).

Another acceleration choice is to reduce the number of employed points. The hierarchical coarse-to-fine strategy is a popular approach (Zhang, 1994; Turk and Levoy, 1994; Neugebauer, 1997). They start the iteration using a lower resolution. While the algorithm approaches the solution, the resolution is hierarchically increased. Some authors used only a sub-sample of the data. The following sub-sampling strategies have been proposed: selection of points in smooth surface areas (Chen and Medioni, 1992), random sampling (Masuda and Yokoya, 1995), regular sampling (Guehring, 2001), selection of points with high intensity gradients (Weik, 1997), and selecting the points according to the distribution of surface normals (Rusinkiewicz and Levoy, 2001). Godin et al. (2001) used a feature vector based random sampling. Distance minimization is performed only between pairs of points considered compatible on the basis of their attributes, e.g. intensity, surface normal, curvature, etc. The hierarchical methods usually give satisfactory results. However, sub-sampling based methods are very sensitive to data content, i.e. noise level, occlusion areas, complexity of the object, etc., and may not exploit the full accuracy potential of the registration.

The main computationally expensive part of the ICP is the exhaustive search for the correspondences. For a review of existing surface correspondence algorithms we refer to Planitz et al. (2005). Besl and McKay (1992) reported that 95% of the run-time is consumed for searching the correspondences. Speeding up the correspondence computation is another option in order to accelerate the ICP. Point-to-projection methods provide very fast solutions, since they reduce the problem to a 2D search when the sensor acquisition geometry or calibration parameters are known (Blais and Levine, 1995; Jokinen and Haggren, 1998). Recently, Park and Subbarao (2003) gave a mixed method combining the accuracy advantage from the point-to-plane technique and speed advantage from the point-to-projection technique. In addition, they gave an overview over the three mostly employed techniques, i.e. point-to-point, point-to-(tangent) plane, and point-to-projection. Projection to multi-z-buffers is another technique (Benjemaa and Schmitt, 1997). The multi-z-buffer technique provides a 3D space partitioning by segmenting the overlapping areas into z-buffer zones according to known depth direction. In general point-to-projection methods can solve the correspondence problem very quickly, but the acquisition geometry and the sensor calibration parameters must be known in advance. On the

other hand, they only give approximations, and the resulting registration is not as accurate as the point-to-point or point-to-plane methods.

Searching the correspondence is an algorithmic problem in fact, and can be substantially optimized by employing special search strategies. Search strategies accelerate the registration by restricting the search space to a subpart of the data. The k-D tree (k dimensional binary search tree) was introduced by Bentley (1975), and is likely the most well-utilized nearest neighbor method (Zhang, 1994; Eggert et al., 1998; Greenspan and Yurick, 2003). The k-D tree is a binary search tree in which each node represents a partition of the k-dimensional space. The root node represents the entire space, and the leaf nodes represent subspaces containing mutually exclusive small subsets of the relevant pointcloud. The space partitioning is carried out in a recursive binary fashion, i.e. letting at each step the direction of the cutting plane alternate between yz-, xz- and xy-plane. The average performance of the k-D tree search is of order ($n$log$n$), and the memory requirement is of order O(n). However, constructing a k-D tree is a quite complicated task and consumes a significant amount of time, which is typical for all kind of tree-search algorithms. The Oct-tree, which is the 3D analogy of the quad-tree, was also used (Jackins and Tanimoto, 1980; Szeliski and Lavallee, 1996; Pulli et al., 1997). Brinkhoff (2004) investigated the usage of hash trees and R-trees, which have originally been developed for spatial database systems. Recently, Wang and Shan (2005) applied the space partitioning technique to a relational database for effective management of LIDAR data. They ordered the 3D cells based on the principle of Hilbert space-filling curves, which provides fast access and spatial query mechanisms.

The pre-computed 3D distance map is another solution (Danielsson, 1980). Unfortunately, storing the complete uniform distance map at the desired accuracy can be expensive in terms of memory requirements. Szeliski and Lavalle (1996) used an approximate but efficient pre-computed distance map named octree spline whose resolution increases hierarchically near the surface. Greenspan and Godin (2001) developed a nearest neighbor method, which calculates the spherical neighborhoods of each point in the preprocessing step, and tracks the evolution of point correspondence across the iterations. Jost and Huegli (2003) combined a coarse to fine strategy with a fast closest point search by employing a nearest neighbor algorithm. They gave an extensive overview on the fast implementations of the ICP as well.

2.3. Related work on multiple surface matching

The early approach for the multiple pointclouds registration is to sequentially apply pairwise registrations until all views are combined. Chen and Medioni (1992) propose a method, which registers successive views incrementally with enough overlapping area. Each next view is registered and merged with the topological union of the former pairwise registrations. Later, this approach was equipped with a coarse-to-fine mesh hierarchy (Turk and Levoy, 1994), and the least median of squares estimator with random sampling (Masuda and Yokoya, 1995).

The shortcomings of the incremental solution were recognized early. The registration of a view does not change once it has been added to the integrated model. However, it is possible that a following view brings information that could have improved the registration of previously processed views (Bergevin et al., 1996; Pulli, 1999). Bergevin et al. (1996) proposes a solution in which every view is matched with all other overlapping views. The procedure is iteratively executed over all views. The iteration is stopped when the registration converges. For each view a separate transformation is calculated, and they are applied simultaneously before the next run of iteration. Although it diffuses the registration errors evenly among all views, slow convergence is the main disadvantage. Benjemaa and Schmitt (1997) accelerate the method by applying the new transformation as soon as it is calculated (similar to the Gauss-Seidel method) and employ a multi-z-buffer technique which provides a 3D space partitioning. Pulli's (1999) solution performs pairwise registrations between every overlapping view pairs. Subsequently, these pairwise registrations are incrementally treated as constraints in a global registration step. However, this constraint does not imply a functional constraint in the optimization procedure. Rather, it is a set of virtual points that uniformly subsample the overlapping areas, called "virtual mate". This approach has the capability to handle large data sets, since using the virtual mates from pairwise alignments does not require loading the entire data set into memory. Another version of this method, called "concrete mate", in which a set of corresponding

points themselves rather than the virtual points is used as constraint, is proposed for robot navigation (Lu and Milios, 1997). The subsequent global registration is achieved by employing a sequential estimation procedure.

Alternatively, some works carry out the multiview registration task in the sensor coordinate system. In Blais and Levine (1995), couples of images are incrementally registered. It is based on reversing the range finder calibration process, resulting in a set of equations which can be used to directly compute the location of a point in a range image corresponding to an arbitrary location in the three dimensional space. Another multiview registration method based on inverse calibration, developed independently, called Iterative Parametric Point (IPP), is given in Jokinen (1998). Differently, it simultaneously registers all views using the Levenberg-Marquardt non-linear optimization technique. Although the reverse calibration method, also called point-to-projection technique, provides fast access mechanisms for the point correspondences, it is performed on 2.5D range maps. It is not suitable for certain 3D applications.

Stoddart and Hilton (1996) first find the pairwise correspondences between all the overlapping views, and then iteratively solve the global registration using a gradient descent algorithm. Although it is a two steps procedure, the final transformations are simultaneously solved as one system in the global registration step. A similar approach, developed independently, is given in Eggert et al. (1998). Neugebauer (1997) reduces the problem to only one global registration step, and simultaneously registers all views using the Levenberg-Marquardt method. Correspondence search is performed on the range maps, which is a 2.5D approach. Williams et al. (1999) suggest a further simultaneous solution by including a priori covariance matrices for each individual point. The non-linear system is solved using the Lagrange multipliers method, or so called Gauss-Helmert estimation model.

The closed-form solutions have become very attractive. Although they are straightforward to implement, their stochastic model is of limited capability in comparison to non-linear optimization techniques. Williams and Bennamoun (2001) present a generalization of Arun et al.'s (1987) well known pairwise registration method, which uses the singular value decomposition to compute the optimal registration parameters in the presence of point correspondences. This method is a closed-form solution for the 3D similarity transformation between two 3D point sets. Beinat and Crosilla (2001) propose the Generalized Procrustes Analysis as a solution for the multiple range image registration problem in the presence of point correspondence. The Procrustes Analysis is another kind of closed-form solution, which was introduced by Schoenemann and Carroll (1970). In fact, both of the methods use Gauss-Seidel or Jacobi type of iteration techniques. Further similar methods are given in Sharp et al. (2004) and in Krishnan et al. (2005).

Recently, Al-Manasir and Fraser (2006) propose an alternative technique, called image-based registration (IBR), for digital camera mounted/integrated terrestrial laserscanner systems, based on the photogrammetric image orientation procedure. The network of images is first oriented using the bundle block adjustment, and then the exterior orientations are transferred to the laserscanner stations provided that the camera calibration and spatial relationship between the camera and laserscanner coordinate systems are known. Since it exclusively uses the imagery, registration can be achieved even in the situations where there is no overlap between the pointclouds.

Several review and comparison studies are available in the literature (Jokinen and Haggren, 1998; Williams et al., 1999; Cunnington and Stoddart, 1999; Campbell and Flynn, 2001).

2.4. Related work in terrain modeling

Since 3D pointclouds derived by any method or device represent the object surface, the problem should be defined as a surface matching problem. In photogrammetry, the problem statement of surface patch matching and its solution method was first addressed by Gruen (1985a) as a straight extension of Least Squares matching.

There have been some studies on the absolute orientation of stereo models using Digital Elevation Models as control information. This work is known as DEM matching. The absolute orientation of the models using Digital Terrain Models (DTM) as control information was first proposed by Ebner and

Mueller (1986) and Ebner and Strunz (1988). Afterwards, the functional model of DEM matching has been formulated by Rosenholm and Torlegard (1988). This method basically estimates the 3D similarity transformation parameters between two DEM patches, minimizing the Least Squares differences along the z-axes. Schenk et al. (2000) showed the clear advantage of minimization of the distances along surface normals against the minimization of elevation differences. Several applications of DEM matching have been reported (Karras and Petsa, 1993; Pilgrim, 1996; Mitchell and Chadwick, 1999; Xu and Li, 2000).

Further studies have been carried out to incorporate the DEMs into aerial block triangulation as control information (Ebner et al., 1991; Ebner and Ohlhof, 1994; Jaw, 2000). Jaw (2000) integrated the surface information into aerial triangulation by extending the independent model method to establish a relationship between model points and planar surface patches, with a goal function that minimizes the sum of the squares of the distance along the surface normal.

Maas (2000) presented a formulation of Least Squares matching to register airborne laser scanner strips, among which vertical and horizontal discrepancies generally show up due to GPS/INS accuracy problems. It estimates the three elements of the translation vector on the original data points in a triangular irregular network (TIN) structure. Alternatively, Kraus et al. (2006) used a raster data structure interpolated form the original pointclouds. Another similar method has been presented for registering surfaces acquired using different techniques, in particular, laser altimetry and photogrammetry (Postolov et al., 1999).

Furthermore, techniques for 2.5D DEM surface matching have been developed, which correspond mathematically to Least Squares image matching. The DEM matching concept can only be applied to 2.5D surfaces, whose analytic function can be described in the explicit form as a single valued function, i.e. $z = f(x,y)$. 2.5D surfaces are of limited value in case of generally formed objects. As a result, the DEM matching method is not fully able to solve the correspondence problems of real 3D surfaces.

2.5. Related work on combined matching of geometry and intensity

When the surface curvature is either homogeneous or isotropic, as is the case with all first-order or some of the second-order surfaces, e.g. plane or spherical surfaces, the geometry-based registration techniques will fail.

Ambiguous solutions in a surface matching computation occur, if any of the principal directions of the object surface has zero or constant curvature. For example, along all directions, a plane and a sphere has zero and constant surface curvatures, respectively. Note that this is not the case for all second order surfaces, so called quadrics. Suppose that two ellipsoids E_1 and E_2 with their semi-axes coefficients $\{a_1, b_1, c_1 ; a_1 \neq b_1 \neq c_1\}$ and $\{a_2, b_2, c_2 ; a_2 \neq (b_2 = c_2)\}$. Surfaces given as E_1 type of ellipsoids can be matched uniquely while E_2 type of ellipsoids can not.

In some studies, surface geometry and intensity (or color) information have been combined in order to solve this problem. Maas (2001) used the airborne laser scanner reflectance images as complimentary to the height data for the determination of horizontal shift parameters between the laser scanner strips of flat areas.

Roth (1999) and Vanden Wyngaerd and Van Gool (2003) used feature-based methods in which interest points and regions are extracted from the intensity images. More often the intensity information is processed as an extra distance value under an ICP algorithm in order to reduce the search effort for corresponding point pairs or in order to eliminate the ambiguities due to inadequate geometric information on the object surface (Weik, 1997; Johnson and Kang, 1999; Godin et al., 2001; Yoshida and Saito, 2002).

Wendt and Heipke (2006) introduced a method for the simultaneous orientation of multiple data types (brightness, range and intensity images). It is a combined Least Squares adjustment, and an algorithmic extension of the object space image matching, which was proposed by Ebner et al. (1987), Wrobel (1987) and Helava (1988).

2.6. Related work on curve matching

Objects in the scene can also be delineated by use of space curves instead of surfaces. In many cases the space curves carry valuable information related to the dimension and shape of the object. They can represent boundaries of regions, ridgelines, silhouettes, etc.

Matching of 2D curves is a very active research area in many disciplines. Several algorithms, which are not explained here in detail, have been proposed in the literature. The contour matching is frequently used as another name for the same problem statement. In spite of presence of much work on curve/contour/line segment/arc matching in 2D space, only few works have been done on the problem of 3D curve matching.

As far as the current methods in the computer vision literature are concerned, the problem has mostly been defined as that of matching of 1D feature strings, obtained from higher degree regression splines. The general attempt is to use some derived features (differential invariants, semi-differential invariants, Fourier descriptors, etc.) instead of utilizing the whole data directly (Schwartz and Sharir, 1987; Parsi et al., 1991; Kishon et al., 1991; Gueziec and Ayache, 1994; Cohen and Wang, 1994; Wang and Cohen, 1994; Pajdla and Van Gool, 1995).

Actually the ICP was proposed to solve the curve matching problem as well in both 2D and 3D space, as explained in its original publications (Besl and McKay, 1992; Zhang, 1994). Lavallee et al. (1991) presented a method that matches 3D anatomical surfaces acquired by MRI (Magnetic Resonance Imaging) or CT (Computed Tomography) to their 2D X-ray projections.

In photogrammetry, the topic was first touched by Gruen (1985a): "… It may even be utilized to match and analyze non-sensor data sets, such as digital height models, digital planimetric models and line map information". The LSM has been addressed as the solution, but not developed yet.

Much work has been done on the matching of line segments in image space using feature based matching or relational matching considering the sensor geometry, auxiliary information, etc., using tree-search or relaxation techniques. Most of the work in this context focuses on automatic extraction of buildings and/or roads from aerial images.

Forkert et al. (1995) gave a method that reconstructs free-formed spatial curves represented in cubic spline form. The curve is adjusted to the bundles of rays coming from two or more images. Zalmanson and Schenk (2001) used 3D free form curves for indirect orientation of pushbroom sensors. They addressed the advantage of using these features for providing continuous control information in object space.

An innovative work was introduced in Gruen and Li (1996) with the LSB-Snakes. The method of active contour models (Snakes) was formulated in a Least Squares approach and at the same time the technique of Least Squares template matching was extended by using a deformable contour instead of a rectangle as the template. This elegant method considerably improves the active contour models by using three new elements: (1) the exploitation of any a priori known geometric and photometric information to constrain the solution, (2) the simultaneous use of any number of images, and (3) the solid background of least-squares estimation. Through the connection of image and object space, assuming that the interior and exterior orientation of the sensors are known, any number of images can be simultaneously accommodated and the feature can be extracted in a 2D as well as in a fully 3D mode.

Although the last three references are not directly related to 3D curve matching, they give some examples on the utilization of 3D curves in photogrammetry.

3

LEAST SQUARES 3D SURFACE MATCHING

3.1. The basic estimation model

Assume that two partial surfaces of an object were digitized at different times or from different viewpoints or by different sensors. $f(x, y, z)$ and $g(x, y, z)$ are conjugate regions of the object in the template and search surfaces, respectively. Both of them are discrete 3D approximations of the continuous function of the object surface. The surface representation can be carried out in any piecewise form. $f(x, y, z)$ and $g(x, y, z)$ stand for any surface element of this representation.

The problem is estimating the parameters of a 3D transformation, which satisfies the Least Squares matching of the search surface $g(x, y, z)$ to the template $f(x, y, z)$. In an ideal situation one would have

$$f(x, y, z) = g(x, y, z) \tag{3.1}$$

Because of the effects of random errors, Equation (3.1) is not consistent. Therefore, a true error vector $e(x, y, z)$ is added, assuming that the template noise is independent of the search noise.

$$f(x, y, z) - e(x, y, z) = g(x, y, z) \tag{3.2}$$

Equation (3.2) are observation equations, which functionally relate the observations $f(x, y, z)$ to the parameters of $g(x, y, z)$. The matching is achieved by Least Squares minimization of a goal function, which measures the sum of the squares of the Euclidean distances between the surfaces. The final location is estimated with respect to an initial position of $g(x, y, z)$, the approximation of the conjugate search surface $g^0(x, y, z)$.

To express the geometric relationship between the conjugate surface patches, a 7-parameter 3D similarity transformation is used:

$$
\begin{aligned}
x &= t_x + m(r_{11}x_0 + r_{12}y_0 + r_{13}z_0) \\
y &= t_y + m(r_{21}x_0 + r_{22}y_0 + r_{23}z_0) \\
z &= t_z + m(r_{31}x_0 + r_{32}y_0 + r_{33}z_0)
\end{aligned}
\tag{3.3}
$$

where $r_{ij} = \mathbf{R}(\omega, \varphi, \kappa)$ is the orthogonal rotation matrix, $[t_x \ t_y \ t_z]^{\mathrm{T}}$ is the translation vector, and m is the uniform scale factor. This parameter space can be extended or reduced, as the situation demands it.

In order to perform a Least Squares estimation, Equation (3.2) is expanded using the Taylor series, of which only the linear terms are retained:

$$f(x, y, z) - e(x, y, z) = g^0(x, y, z) + \frac{\partial g^0(x, y, z)}{\partial x}\,\mathrm{d}x + \frac{\partial g^0(x, y, z)}{\partial y}\,\mathrm{d}y + \frac{\partial g^0(x, y, z)}{\partial z}\,\mathrm{d}z \tag{3.4}$$

with

$$\mathrm{d}x = \frac{\partial x}{\partial p_i}\,\mathrm{d}p_i \quad , \quad \mathrm{d}y = \frac{\partial y}{\partial p_i}\,\mathrm{d}p_i \quad , \quad \mathrm{d}z = \frac{\partial z}{\partial p_i}\,\mathrm{d}p_i \tag{3.5}$$

where $p_i \in \{t_x, t_y, t_z, m, \omega, \varphi, \kappa\}$ is the i-th transformation parameter in Equation (3.3). Differentiation of Equation (3.3) gives:

$$d x = d t_x + a_{10} \, d m + a_{11} \, d \omega + a_{12} \, d \varphi + a_{13} \, d \kappa$$
$$d y = d t_y + a_{20} \, d m + a_{21} \, d \omega + a_{22} \, d \varphi + a_{23} \, d \kappa$$
$$d z = d t_z + a_{30} \, d m + a_{31} \, d \omega + a_{32} \, d \varphi + a_{33} \, d \kappa \tag{3.6}$$

where a_{ij} are the coefficient terms. Given the rotation matrix $\mathbf{R}$ as

$$\mathbf{R} = \begin{bmatrix} \cos\varphi\cos\kappa & -\cos\varphi\sin\kappa & \sin\varphi \\ \cos\omega\sin\kappa + \sin\omega\sin\varphi\cos\kappa & \cos\omega\cos\kappa - \sin\omega\sin\varphi\sin\kappa & -\sin\omega\cos\varphi \\ \sin\omega\sin\kappa - \cos\omega\sin\varphi\cos\kappa & \sin\omega\cos\kappa + \cos\omega\sin\varphi\sin\kappa & \cos\omega\cos\varphi \end{bmatrix} \tag{3.7}$$

the coefficient terms a_{ij} are represented as:

$$a_{10} = r_{11}x_0 + r_{12}y_0 + r_{13}z_0$$
$$a_{20} = r_{21}x_0 + r_{22}y_0 + r_{23}z_0$$
$$a_{30} = r_{31}x_0 + r_{32}y_0 + r_{33}z_0$$
$$a_{11} = 0$$
$$a_{12} = m(-\sin\varphi\cos\kappa\, x_0 + \sin\varphi\sin\kappa\, y_0 + \cos\varphi\, z_0)$$
$$a_{13} = m(r_{12}x_0 - r_{11}y_0)$$
$$a_{21} = m(-r_{31}x_0 - r_{32}y_0 - r_{33}z_0)$$
$$a_{22} = m(\sin\omega\cos\varphi\cos\kappa\, x_0 - \sin\omega\cos\varphi\sin\kappa\, y_0 + \sin\omega\sin\varphi\, z_0)$$
$$a_{23} = m(r_{22}x_0 - r_{21}y_0)$$
$$a_{31} = m(r_{21}x_0 + r_{22}y_0 + r_{23}z_0)$$
$$a_{32} = m(-\cos\omega\cos\varphi\cos\kappa\, x_0 + \cos\omega\cos\varphi\sin\kappa\, y_0 - \cos\omega\sin\varphi\, z_0)$$
$$a_{33} = m(r_{32}x_0 - r_{31}y_0) \tag{3.8}$$

Using the following notation

$$g_x = \frac{\partial g^0(x,y,z)}{\partial x}, \quad g_y = \frac{\partial g^0(x,y,z)}{\partial y}, \quad g_z = \frac{\partial g^0(x,y,z)}{\partial z} \tag{3.9}$$

and substituting Equations (3.6), Equation (3.4) results in the following:

$$-e(x,y,z) = g_x \, d t_x + g_y \, d t_y + g_z \, d t_z + (g_x a_{10} + g_y a_{20} + g_z a_{30}) \, d m$$
$$+ (g_x a_{11} + g_y a_{21} + g_z a_{31}) \, d \omega$$
$$+ (g_x a_{12} + g_y a_{22} + g_z a_{32}) \, d \varphi$$
$$+ (g_x a_{13} + g_y a_{23} + g_z a_{33}) \, d \kappa - (f(x,y,z) - g^0(x,y,z)) \tag{3.10}$$

In the context of the Gauss-Markoff model, each observation is related to a linear combination of the parameters, which are variables of a deterministic unknown function. The terms $\{g_x, g_y, g_z\}$ are numeric first derivatives of this function $g(x,y,z)$.

Equation (3.10) gives in matrix notation

$$-e = \mathbf{A}x - l \quad , \quad \mathbf{P} \tag{3.11}$$

where $\mathbf{A}$ is the design matrix, $\mathbf{P} = \mathbf{P}_{ll}$ is the a priori weight matrix, $x^{\mathrm{T}} = [dt_x \ dt_y \ dt_z \ dm \ d\omega \ d\varphi \ d\kappa]$ is the parameter vector, and $l = f(x,y,z) - g^0(x,y,z)$ is the discrepancy vector that consists of the Euclidean distances between the template and correspondent search surface elements. In our implementation, the template surface elements are approximated by the data points. On the other hand, the search surface elements are represented by user selection of one of the two different type of piecewise surface forms (planar and bi-linear). In general, both surfaces can be represented in any kind of piecewise form.

With the statistical expectation operator $E\{\}$ and the assumptions

$$e \sim N(0, \sigma_0^2 \mathbf{Q}_{ll}) \quad , \quad \sigma_0^2 \mathbf{Q}_{ll} = \sigma_0^2 \mathbf{P}_{ll}^{-1} = \mathbf{K}_{ll} = E\{ee^T\} \tag{3.12}$$

the system (3.11) and (3.12) is a Gauss-Markoff estimation model. $\mathbf{Q}_{ll}$ and $\mathbf{K}_{ll}$ stand for a priori cofactor and covariance matrices, respectively.

The unknown transformation parameters are treated as stochastic quantities using proper a priori weights. This extension gives advantages of control over the estimating parameters. We introduce the additional observation equations for the system parameters as

$$-e_b = \mathbf{I}x - l_b \quad , \quad \mathbf{P}_b \tag{3.13}$$

where $\mathbf{I}$ is the identity matrix, l_b is the (fictitious) observation vector for the system parameters, and $\mathbf{P}_b$ is the associated weight coefficient matrix. The weight matrix $\mathbf{P}_b$ has to be chosen appropriately, considering a priori information of the parameters. An infinite weight value (($\mathbf{P}_b)_{ii} \to \infty$) excludes the i-th parameter from the system assigning it as constant, whereas zero weight (($\mathbf{P}_b)_{ii} = 0$) allows the i-th parameter to vary freely assigning it as free parameter in the classical meaning.

The Least Squares solution of the joint system Equations (3.11) and (3.13) gives as the Generalized Gauss-Markoff model the unbiased minimum variance estimation for the parameters

$$\hat{x} = (\mathbf{A}^T \mathbf{P} \mathbf{A} + \mathbf{P}_b)^{-1} (\mathbf{A}^T \mathbf{P} l + \mathbf{P}_b l_b) \qquad \text{solution vector} \tag{3.14}$$

$$\hat{\sigma}_0^2 = (v^T \mathbf{P} v + v_b^T \mathbf{P}_b v_b)/r \qquad \text{variance factor} \tag{3.15}$$

$$v = \mathbf{A}\hat{x} - l \qquad \text{residual vector for surface observations} \tag{3.16}$$

$$v_b = \mathbf{I}\hat{x} - l_b \qquad \text{residual vector for parameter observations} \tag{3.17}$$

where $\wedge$ stands for the Least Squares Estimator, $r = n - u$ is the redundancy, n is the number of observations that is equivalent to the number of elements of the template surface, and u is the number of transformation parameters that is seven here. When the system converges, the solution vector converges to zero ($\hat{x} \to 0$). Then the residuals of the surface observations v_i become the final Euclidean distances between the estimated search surface and the template surface:

$$v_i = \hat{g}(x, y, z)_i - f(x, y, z)_i \quad , \quad i = 1, ..., n \tag{3.18}$$

The function values $g(x, y, z)$ in Equation (3.2) are actually stochastic quantities. This fact is neglected here to allow for the use of the Gauss-Markoff model and to avoid unnecessary complications, as it is typically done in LSM (Gruen, 1985a). This assumption is valid and the omissions are not significant as long as the random errors of the template and search surfaces are normally distributed and uncorrelated. In the extreme case when the random errors of the both surfaces show systematic and dependency patterns, which is most probably caused by defect or imperfectness of the measurement technique or the sensor, it should be an interesting study to investigate the error behavior using the total Least Squares (TLS) method (Golub and Van Loan, 1980). The TLS is a relatively new adjustment method of estimating parameters in linear models that include errors in all variables (Schaffrin and Felus, 2003).

The functional model is non-linear. The solution iteratively approaches a minimum. With the solution of linearized functional models, there is always a danger to find local minima. A global minimum can only be guaranteed if the function is expanded to Taylor series at such a point where the approximate values of the parameters are close enough to their true values ($p_i^0 \approx p_i \in \Re^u; i = 1, ..., u$) in parameter space. We ensure this condition by providing of good quality initial approximations for the parameters in the first iteration:

$$p_i^0 \in \{t_x^0, t_y^0, t_z^0, m^0, \omega^0, \varphi^0, \kappa^0\} \tag{3.19}$$

After the solution vector (3.14) has been solved for, the search surface is transformed to a new state using the updated set of transformation parameters, and the design matrix $\mathbf{A}$ and the discrepancies vector l are re-evaluated. The iteration stops if each element of the alteration vector $\hat{x}$ in Equation (3.14) falls below a certain limit:

$$\left| \mathrm{d}\, p_i \right| < c_i \quad , \quad \mathrm{d}\, p_i \in \{ \mathrm{d}\, t_x, \mathrm{d}\, t_y, \mathrm{d}\, t_z, \mathrm{d}\, m, \mathrm{d}\, \omega, \mathrm{d}\, \varphi, \mathrm{d}\, \kappa \} \tag{3.20}$$

Adopting the parameters as stochastic variables allows adapting the dimension of the parameter space in a problem specific manner. In the case of insufficient a priori information on the geometric deformation characteristics of the template and search surfaces, the adjustment could be started employing a transformation model with more than 7 parameters, e.g. a 12-parameter 3D affine transformation. However, this approach very often leads to an over-parameterization problem. Therefore, during the iterations an appropriate test procedure that is capable to exclude non-determinable parameters from the system should be performed. For a suitable testing strategy we refer to Gruen (1985c).

3.2. Surface representation and numerical derivatives

The terms $\{g_x, g_y, g_z\}$ are numeric 1st derivatives of the unknown surface $g(x, y, z)$. Their calculation depends on the analytical representation of the surface elements.
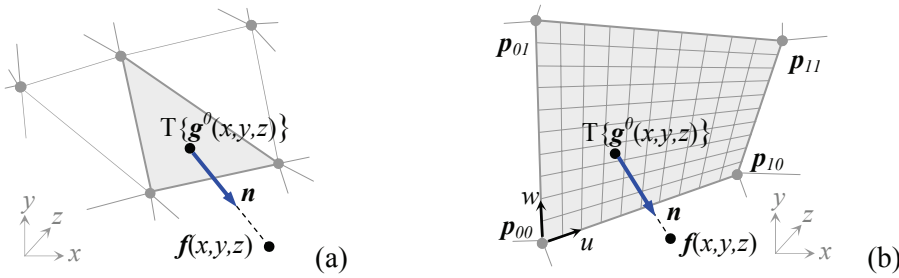
Figure 1. Representation of surface elements in planar (a), and bi-linear (b) forms. Note that T{} stands for the transformation operator.

As a first method, let us represent the search surface as composite of planar elements (Figure 1a), which are constituted by fitting a plane to 3 neighboring knot points, in the non-parametric implicit form

$$g^0(x, y, z) = Ax + By + Cz + D = 0 \tag{3.21}$$

where A, B, C, and D are the parameters of the plane. The numeric 1st derivation according to the x-axis is

$$g_x = \frac{\partial g^0(x, y, z)}{\partial x} = \lim_{\Delta x \to 0} \frac{g^0(x + \Delta x, y, z) - g^0(x, y, z)}{\Delta x} \tag{3.22}$$

where the numerator term of the equation is simply the distance between the plane and the off-plane point $(x + \Delta x, y, z)$. Then using the point-to-plane distance formula,

$$g_x = \frac{A(x + \Delta x) + By + Cz + D}{\Delta x \sqrt{A^2 + B^2 + C^2}} = \frac{A}{\sqrt{A^2 + B^2 + C^2}} \tag{3.23}$$

is obtained. Similarly g_y and g_z are calculated numerically:

$$g_y = \frac{B}{\sqrt{A^2 + B^2 + C^2}} \quad , \quad g_z = \frac{C}{\sqrt{A^2 + B^2 + C^2}} \tag{3.24}$$

Actually, these numeric derivative values $\{g_x, g_y, g_z\}$ are x-y-z components of the local surface normal vector $\boldsymbol{n}$ at the exact correspondence location on the search surface:

$$\begin{bmatrix} g_x & g_y & g_z \end{bmatrix}^{\mathrm{T}} = \boldsymbol{n} = \begin{bmatrix} n_x & n_y & n_z \end{bmatrix} = \frac{\begin{bmatrix} A & B & C \end{bmatrix}^{\mathrm{T}}}{\sqrt{A^2 + B^2 + C^2}} \tag{3.25}$$

For the representation of the search surface as parametric bi-linear elements (Figure 1b), a bi-linear surface is fitted to 4 neighboring knot points $\boldsymbol{p}_{ij}$:

$$g^0(u,w) = \begin{bmatrix} x(u,w) & y(u,w) & z(u,w) \end{bmatrix}^{\mathrm{T}} \tag{3.26}$$

$$g^0(u,w) = \boldsymbol{p}_{00}(1-u)(1-w) + \boldsymbol{p}_{01}(1-u)w + \boldsymbol{p}_{10}u(1-w) + \boldsymbol{p}_{11}uw \tag{3.27}$$

where $u, w \in [0,1]^2$ and $g^0(u,w)$, $\boldsymbol{p}_{ij} \in \Re^3$. The vector $g^0(u,w)$ is the position vector of any point on the bi-linear surface. Again the numeric derivative terms $\{g_x, g_y, g_z\}$ are calculated from components of the local surface normal vector $\boldsymbol{n}$ on the parametric bi-linear surface:

$$\begin{bmatrix} g_x & g_y & g_z \end{bmatrix}^{\mathrm{T}} = \boldsymbol{n} = \frac{\partial g^0(u,w)}{\partial u} \times \frac{\partial g^0(u,w)}{\partial w} \left/ \left\| \frac{\partial g^0(u,w)}{\partial u} \times \frac{\partial g^0(u,w)}{\partial w} \right\| \right. \tag{3.28}$$

where $\times$ stands for the vector cross product. With this approach a slightly better a posteriori sigma value could be obtained due to better surface modeling.

Conceptually, derivative terms $\{g_x, g_y, g_z\}$ constitute a normal vector field with unit magnitude $\|\boldsymbol{n}\|=1$ on the search surface. This vector field slides over the template surface towards the final solution, minimizing the Least Squares objective function.

The surface representation is carried out in two different forms optionally: a TIN form, which gives planar surface elements, and a grid mesh form, which gives bi-linear surface elements. Both of these are first degree C^0 continuous surface representations. Surface topology is established simply by reading the standard range scanner output files in ASCII format and loading them in the scan-line order. For the pointclouds which have an irregular or unconventional sampling principle (or pattern), a more complex surface mesh generation algorithm can be utilized.

In the case of multi-resolution data sets, in which point densities are significantly different on the template and search surfaces, higher degree C^1 continuous composite surface representations, e.g. bi-cubic Hermit surface (Peters, 1974), should give better results, of course increasing the computational expenses.

3.3. Numerical derivatives on the template surface

In the case of insufficient initial approximations, the numerical derivatives can also be calculated on the template surface $f(x,y,z)$ instead of on the search surface $g(x,y,z)$ in order to speed-up the convergence. This speed-up version apparently decreases the computational effort of the design matrix $\mathbf{A}$ as well, since the derivative terms $\{f_x, f_y, f_z\}$ are calculated only once in the first iteration, and the same values are used in the following iterations.

The functional model of this version is given below.

$$\begin{aligned} -e(x,y,z) = &f_x \, \mathrm{d}t_x + f_y \, \mathrm{d}t_y + f_z \, \mathrm{d}t_z + (f_x a_{10} + f_y a_{20} + f_z a_{30}) \, \mathrm{d}m \\ &+ (f_x a_{11} + f_y a_{21} + f_z a_{31}) \, \mathrm{d}\omega \\ &+ (f_x a_{12} + f_y a_{22} + f_z a_{32}) \, \mathrm{d}\varphi \\ &+ (f_x a_{13} + f_y a_{23} + f_z a_{33}) \, \mathrm{d}\kappa - (f(x,y,z) - g^0(x,y,z)) \end{aligned} \tag{3.29}$$

As opposed to the basic model, the number of the observation equations contributing to the design matrix $\mathbf{A}$ is here defined by the number of elements on the search surface $g(x,y,z)$. In other words, the correspondence is searched on the template surface $f(x,y,z)$ for each surface element of the search surface $g(x,y,z)$.

However, this is not a fully strict model. The derivative terms are approximated from the template surface. Comparisons against the strict model, given in Equation (3.10), show that the numerical differences of the solution vectors are not statistically significant.

Depending on the resolution or quality of the template or the search surfaces, either Equation (3.10) or Equation (3.29) can be selected for the functional model. Hence, the design matrix is established from the better surface, while the search surface is still floating and the template is fixed.

3.4. Precision, reliability and error detection

The standard deviations of the estimated transformation parameters and the correlations between them may give useful information concerning the stability of the system and quality of the data content (Gruen, 1985a):

$$\hat{\sigma}_p = \hat{\sigma}_0 \sqrt{q_{pp}} \quad , \quad q_{pp} \in \mathbf{Q}_{xx} = (\mathbf{A}^\mathrm{T}\mathbf{PA} + \mathbf{P}_b)^{-1} \tag{3.30}$$

where $\mathbf{Q}_{xx}$ is the cofactor matrix for the estimated parameters.

The estimated standard deviations of the transformation parameters are optimistic, mainly due to the stochastic properties of the search surfaces that have not been considered as such in the estimation model, as is typically done in Least Squares matching (Gruen, 1985a). The omissions are expected to be minor and do not disturb the solution vector significantly. However, the a posteriori covariance matrix will be affected by the neglected uncertainty of the function values $g(x, y, z)$. This deteriorates the realistic precision estimates. More details on this issue can be found in Gruen (1985a), Maas (2000), Gruen and Akca (2005) and Kraus et al. (2006).

Detection of false correspondences with respect to the outliers and occlusions is a crucial part of every surface matching method. We use the following strategies in order to localize and eliminate the outliers and the occluded parts.

A median type of filtering is applied prior to the matching. For each point, the distances between the central point and its k-neighborhood points are calculated. In our implementation, k is selected as 8. If most of those k-distance values are much greater than the average point density, the central point is likely to be an erroneous point on a poorly reflecting surface (e.g. window or glass) or a range artifact due to surface discontinuity (e.g. points on the object silhouette). The central point is discarded according to the number of distances, which are greater than a given distance threshold.

In the course of iterations a simple weighting scheme adapted from Robust Estimation Methods is used:

$$(\mathbf{P})_{ii} = \begin{cases} 1 & \text{if} \quad |(\mathbf{v})_i| < K\hat{\sigma}_0 \\ 0 & \text{else} \end{cases} \tag{3.31}$$

In our experiments K is selected as >10, since it is aimed to suppress only the large outliers. It can be changed according to a desired confidence level. Because of the high redundancy of a typical data set, a certain amount of occlusions and/or smaller outliers do not have significant effect on the estimated parameters. As a comprehensive strategy, Baarda's (1968) data-snooping method can be favorably used to localize the occluded or gross erroneous measurements.

Finally, the correspondences coinciding to mesh boundaries are excluded from the estimation. The mesh boundaries represent the model borders, additionally the data holes inside the model. The data holes are possibly due to occlusions. Rejecting the correspondences on the mesh boundaries effectively eliminates the occlusions.

3.5. Convergence behavior

In a standard Least Squares adjustment calculus, the function of the unknowns is unique, exactly known, and analytically continuous everywhere. Here the function $g(x, y, z)$ is discretized by using a finite sampling rate, which leads to slow convergence, oscillations, even divergence in some cases with respect to the standard adjustment. The convergence behavior of the proposed method basically depends on the quality of the initial approximations and quality of the data content. For a good data configuration, it usually achieves the solution after 5 or 6 iterations (Figure 2), which is typical for the Least Squares matching.
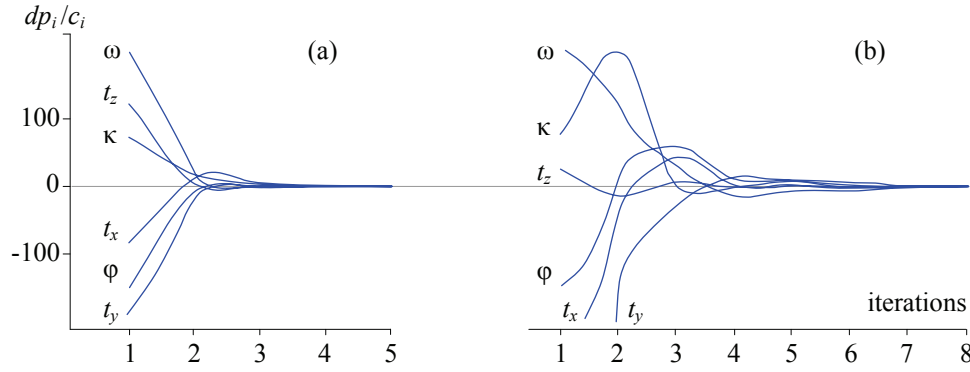
Figure 2. Typical examples for fast (a) and slow (b) convergence. Note that here the scale factor m is fixed to unity.

3.6. Computational aspects

The computational effort increases with the number of points in the matching process. The main portion of the computational complexity is to search the corresponding elements of the template surface patch on the search surface, whereas the parameter estimation part is a small system, and is quickly solved using Cholesky decomposition followed by back-substitution. Searching the correspondence is guided by an efficient boxing structure (Chetverikov, 1991), which partitions the search space into cuboids. For a given surface element, the correspondence is searched only in the box containing this element and in the adjacent boxes. The details are given in Chapter 3.8.1.

3.7. The Generalized Gauss-Markoff versus Levenberg-Marquardt

In Neugebauer (1997) and Szeliski and Lavallee (1996) two gradient descent type of algorithms are given. They calculate the Euclidean distances as evaluation function value by interpolation using point-to-projection and octree spline methods respectively. They adopt the Levenberg-Marquardt method, in which diagonal elements of the normal matrix $\mathbf{N}$ are augmented by a damping matrix $\mathbf{D}$ in order to prevent numerical problems: $(\mathbf{N}+\lambda\mathbf{D})\boldsymbol{\delta} = \boldsymbol{n}$ where $\lambda > 0$ is the stabilization factor that varies during the iterations. The damping matrix $\mathbf{D}$ is often chosen as an identity matrix $\mathbf{I}$ or a diagonal matrix containing the diagonal elements of the normal matrix (diag($\mathbf{N}$)).

The Generalized Gauss-Markoff model might be seen as identical to the Levenberg-Marquardt, as the weight matrix $\mathbf{P}_b$ has a damping effect on the normal matrix. But, it is a thorough statistical approach considering the a priori stochastic information (Equation 3.13), and a straightforward result of the Least Squares formulation (Equation 3.14). The Levenberg-Marquardt method is rather a numerical approach with no direct stochastical justification.

Assume that two planes are the subject of the matching process. During the solution of a standard Least Squares adjustment, the normal matrix becomes singular, since there is not a unique solution geometrically. This numerical reflex issues a warning to the user. On the other hand, Levenberg-Marquardt will give one of the solutions out of the infinite number. Geometrically ill-configured data sets are reasons for the near-singularity cases. When singularity or ill-conditioning occurs, one must carefully inspect the system and diagnose the data, instead of doing arbitrary numerical manipulations.

3.8. Acceleration strategies

3.8.1. Fast correspondence search with boxing structure

Let points $\boldsymbol{a}_i = \{x_i, y_i, z_i\} \in S$, $i = 0,1,\ldots, N$-1, represent the object $S \in \mathfrak{R}^3$, and be kept in list $\mathbf{L}_1$ in spatially non-ordered form. The boxing data structure (Figure 3) consists of a rearranged point list $\mathbf{L}_2$ and an index matrix $\mathbf{I} = I_{u,v,w}$ whose elements are associated to individual boxes: $u,v,w = 0,1,\ldots, M$-1.

The items of $\mathbf{L}_2$ are coordinates of N points placed in the order of boxes. The index matrix $\mathbf{I}$ contains integers indicating the beginnings of the boxes in $\mathbf{L}_2$.

Initialization. Defining the box size.
Step 1. Recall min, max $\{x_i, y_i, z_i\}$ of data volume.
Step 2. Define number of boxes along x-y-z axes. For the sake of simplicity, they are given the same (M) here.

Pass 1. Computing $\mathbf{I}$.
Step 1. Allocate an M x M x M size accumulator array $\mathbf{B} = B_{u,v,w}$ which is to contain the number of points in each box.
Step 2. Scan $\mathbf{L}_1$ and fill $\mathbf{B}$. For any point $\boldsymbol{a}_i$ the box indices are as follows:

$$u_i = \left\lfloor \frac{x_i - x_{\min}}{D_X} \right\rfloor, \quad v_i = \left\lfloor \frac{y_i - y_{\min}}{D_Y} \right\rfloor, \quad w_i = \left\lfloor \frac{z_i - z_{\min}}{D_Z} \right\rfloor \tag{3.32}$$

where $\lfloor \ \rfloor$ stands for the truncation operator, and D_X, D_Y and D_Z are dimensions of any box along the x-y-z axes respectively.
Step 3. Fill $\mathbf{I}$ using the following recursive formula:

$I_{0,0,0} = 0.$
For all $(u,v,w) \neq (0,0,0)$

$$I_{u,v,w} = \begin{cases} I_{u,v,w-1} + B_{u,v,w-1} & \text{if} \quad w > 0 \\ I_{u,v-1,M-1} + B_{u,v-1,M-1} & \text{else if} \quad v > 0 \\ I_{u-1,M-1,M-1} + B_{u-1,M-1,M-1} & \text{else} \end{cases} \tag{3.33}$$

Pass 2. Filling $\mathbf{L}_2$.
Step 1. For all u, v and w, set $B_{u,v,w} = 0$.
Step 2. Scan $\mathbf{L}_1$ again. Use Equation (3.32), $\mathbf{I}$ and $\mathbf{B}$ to fill $\mathbf{L}_2$. In $\mathbf{L}_2$, the first point of the (u,v,w)-th box is indexed by $\mathbf{I}$ while the address of the subsequent points is controlled via $\mathbf{B}$ whose value is incremented each time a new point enters the box. Finally, release the memory area of $\mathbf{B}$.

The memory requirement is of order O(N) for $\mathbf{L}_2$ and O(M^3) for $\mathbf{I}$. For the sake of clarity of the explanation, $\mathbf{L}_2$ is given as a point list containing the x-y-z coordinate values. If one wants to keep the $\mathbf{L}_1$ in the memory, then $\mathbf{L}_2$ should only contain the access indices to $\mathbf{L}_1$ or pointers, which directly point to the memory locations of the point coordinates.

Access procedure.
Step 1. Using Equation (3.32), compute the indices u_i, v_i and w_i of the box that contains point $\boldsymbol{a}_i$.
Step 2. Use the boxing structure to retrieve the points bounded by the (u,v,w)-th box. In $\mathbf{L}_2$, $\mathbf{I}$ indexes the first point, while the number of points in the box is given by the following formula:

$$\begin{cases} I_{u,v,w+1} - I_{u,v,w} & \text{if} \quad w < M-1 \\ I_{u,v+1,0} - I_{u,v,M-1} & \text{else if} \quad v < M-1 \\ I_{u+1,0,0} - I_{u,M-1,M-1} & \text{else if} \quad u < M-1 \\ N - I_{M-1,M-1,M-1} & \text{else} \end{cases} \tag{3.34}$$

The access procedure requires O(q) operations, where q is the average number of points in the box. One of the main advantages of the boxing structure is a faster and easier access mechanism than the tree search-based methods provide.
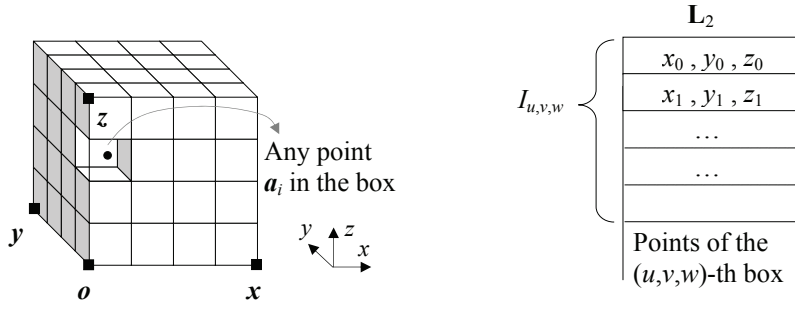
Figure 3. 3D Boxing. (left) Boxing binds all the data points, (right) the boxing data structure.

The boxing structure, and in general all search structures, are designed for searching the nearest neighborhood in the static pointclouds. In the LS3D surface matching case, the search surface, which the boxing structure is established for, is transformed to a new state by the current set of transformation parameters. Nevertheless there is no need neither to re-establish the boxing structure nor to update the $\mathbf{I}$ and $\mathbf{L}_2$ in each iteration. Only positions of those four points (Figure 3) are updated in the course of iterations: $\boldsymbol{o} = \{x_{min}, y_{min}, z_{min}\}$, $\boldsymbol{x} = \{x_{max}, y_{min}, z_{min}\}$, $\boldsymbol{y} = \{x_{min}, y_{max}, z_{min}\}$, $\boldsymbol{z} = \{x_{min}, y_{min}, z_{max}\}$. They uniquely define the boxing structure under the similarity transformation. The access procedure is the same, except the following formula is used for the indices calculation:

$$u_i = \left\lfloor \frac{oa_i \cdot ox}{\|ox\| D_X} \right\rfloor, \quad v_i = \left\lfloor \frac{oa_i \cdot oy}{\|oy\| D_Y} \right\rfloor, \quad w_i = \left\lfloor \frac{oa_i \cdot oz}{\|oz\| D_Z} \right\rfloor \tag{3.35}$$

where $\cdot$ stands for vector dot product. If the transformation is a similarity rather than a rigid body, the D_X, D_Y and D_Z values must also be updated in the iterations.

In our implementation, the correspondence is searched in the boxing structure during the first few iterations, and in the meantime its evolution is tracked across the iterations. Afterwards the searching process is carried out only in an adaptive local neighborhood according to the previous position and change of correspondence. In any step of the iteration, if the change of correspondence for a surface element exceeds a limit value, or oscillates, the search procedure for this element is returned to the boxing structure again.

3.8.2. Simultaneous multi-subpatch matching

The basic estimation model can be implemented in a multi-patch mode, that is the simultaneous matching of two or more search surfaces $g_i(x, y, z)$, $i = 1, \ldots, k$ to one template $f(x, y, z)$.

$$
\begin{aligned}
-\boldsymbol{e}_1 &= \mathbf{A}_1 \boldsymbol{x}_1 - \boldsymbol{l}_1 \quad, \quad \mathbf{P}_1 \\
-\boldsymbol{e}_2 &= \mathbf{A}_2 \boldsymbol{x}_2 - \boldsymbol{l}_2 \quad, \quad \mathbf{P}_2 \\
&\vdots \qquad\qquad \vdots \\
-\boldsymbol{e}_k &= \mathbf{A}_k \boldsymbol{x}_k - \boldsymbol{l}_k \quad, \quad \mathbf{P}_k
\end{aligned} \tag{3.36}
$$

Since the parameter vectors $\boldsymbol{x}_1, \ldots, \boldsymbol{x}_k$ do not have any joint components, the sub-systems of Equation (3.36) are orthogonal to each other. In the presence of auxiliary information, those sets of equations could be connected via functional constraints, e.g. as in the geometrically constrained multiphoto matching (Gruen, 1985a; Gruen and Baltsavias, 1988) or via appropriate formulation of multiple (>2) overlap conditions.

An ordinary pointcloud includes enormously redundant information. A straightforward way to register such two pointclouds could be matching of the whole overlapping areas. This is computationally expensive. We propose multi-subpatch mode as a further extension to the basic model, which is capable of simultaneous matching of sub-surface patches, which are interactively selected in cooperative surface areas. They are joined to the system by the same 3D transformation parameters. This leads to the observation equations

$$-e_1 = \mathbf{A}_1\,x - l_1 \quad, \quad \mathbf{P}_1$$
$$-e_2 = \mathbf{A}_2\,x - l_2 \quad, \quad \mathbf{P}_2$$
$$\vdots \qquad\qquad \vdots$$
$$-e_k = \mathbf{A}_k\,x - l_k \quad, \quad \mathbf{P}_k \tag{3.37}$$

with $i =1,\ldots, k$ subpatches. They can be combined as in Equation (3.11), since the common parameter vector x joints them to each other. The individual subpatches may not include sufficient information for the matching of whole surfaces, but together they provide a computationally effective solution, since they consist of only relevant information rather than using the full data set.

3.9. Multiple surface matching

When more than two surfaces with multiple overlaps exist, the procedure is split into two steps: sequential pairwise registrations and a final global registration. The pairwise registrations establish the correspondences between the overlapping pairs of surfaces. The global registration distributes the residual errors evenly among all of the surfaces, and also considers the multiple overlap conditions and the closure condition, i.e. matching of the last surface to the first one.

One of the surfaces is selected as the reference, which defines the datum of the common coordinate system. The pairwise LS3D matching processes are run on every possible overlapping surface pairs, starting from the datum one. Each matched surface is incrementally added to the union of the previously registered surfaces. If the search surface is already in the union, i.e. surface has multiple overlaps, the transformation is not applied.

Each pairwise registration gives the 3D transformation parameters of the search surface and additionally the correspondences between the template and the search surfaces. These final correspondences are saved to separate files. Every individual correspondence gives a (fictitious) tie point. The numbers of tie points are thinned out by selecting of every n-th correspondence.

Then, all these files are given as input to the block adjustment by independent models software BAM7, which is an in-house software based on a 7-parameter 3D similarity transformation. The block adjustment by independent models, which is a well-known orientation procedure in photogrammetry (Ackermann et al., 1973), was formerly proposed for the global registration of laser scanner pointclouds, but for the case of retro-reflective targets as tie points (Scaioni and Forlani, 2003).

In the BAM7 software, (fictitious) points of the datum surface are treated as the control points. This leads the transformation parameters of the datum surfaces fixed in the procedure. The transformation parameters of all the other surfaces will be optimized regarding the global agreement of the whole data.

4

SIMULTANEOUS MATCHING OF SURFACE GEOMETRY AND INTENSITY

When there is a lack of sufficient geometric information (homogeneity or isotropicity of curvatures), the procedure may fail, since there is not a unique solution geometrically, e.g. when matching two planes or spherical objects. An object surface may have some attribute information attached to it. Intensity, color and temperature are well known examples. Most of the laser scanners can supply intensity information in addition to the Cartesian coordinates for each point, or an additional camera may be used to collect texture. A solution is proposed that can simultaneously match intensity information and geometry under a combined estimation model. In this approach the intensity image of the pointcloud also contributes observation equations to the system, considering the intensities as supplementary information to the range image.

4.1. Formation of quasisurfaces

Rather than adopting a feature-based or step-wise approach, this method sets up quasisurfaces from intensity information in addition to the actual surfaces.

A hypothetical example of forming the quasisurfaces is given in Figure 4. The procedure starts with the calculation of surface normal vectors at each data point. The actual surface will include noise and surface spikes (Figure 4b), which lead to unrealistic calculations for the normal vectors. To cope with the problem, a moving average or median type filtering process could be employed. But still some noise would remain depending on the window size.
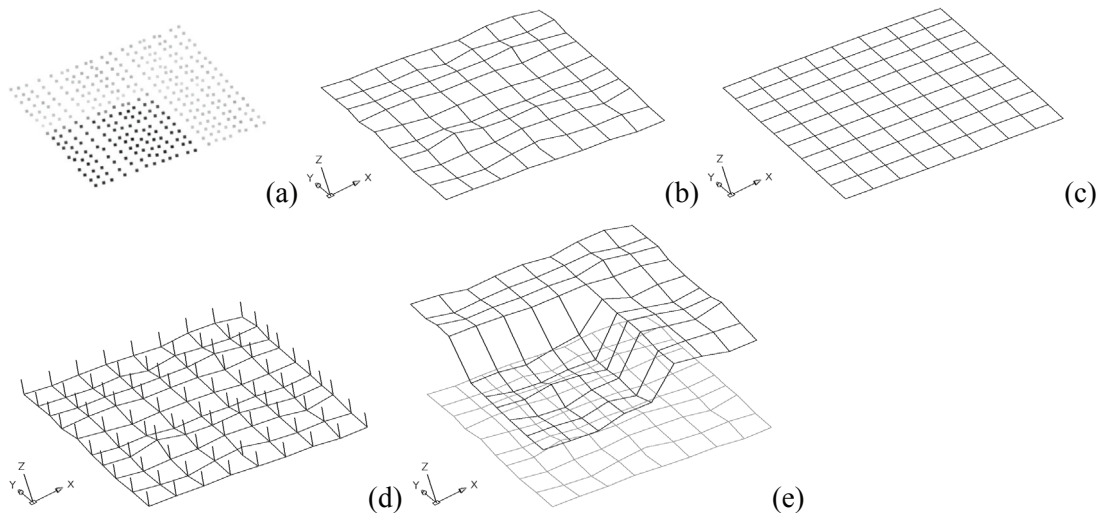

Figure 4. Forming the quasisurface. (a) Pointcloud with intensity information, (b) meshed surface of the pointcloud, (c) trend surface fitted to the pointcloud, (d) normal vectors attached onto the actual surface, (e) generated quasisurface in addition to the actual one.

An optimum solution is the Least Squares fitting of a global trend surface to the whole pointcloud (Figure 4c). It will suppress the noise component and preserve the global continuity of the normal vectors along the surface. The parametric bi-quadratic trend surface was chosen, which is sufficient to model the quadric type of surfaces, e.g. plane, sphere, ellipsoid, etc.

For the template surface patch $f(x, y, z)$ we obtain:

$$F(u, w) = \sum_{i=0}^{2} \sum_{j=0}^{2} \boldsymbol{b}_{ij} u^i w^j \tag{4.1}$$

where $u, w \in [0,1]^2$, $F(u,w) \in \Re^3$ is the position vector of any point on the trend surface, and $\boldsymbol{b}_{ij} \in \Re^3$ are the algebraic coefficients, which are estimated by Least Squares fitting.

For each point, the normal vector $\boldsymbol{n}_f$ is calculated on the trend surface $F(u,w)$ and attached to the actual surface $f(x, y, z)$ (Figure 4d):

$$\boldsymbol{n}_f = \boldsymbol{n}_f(u, w) = \frac{\boldsymbol{F}_u \times \boldsymbol{F}_w}{\|\boldsymbol{F}_u \times \boldsymbol{F}_w\|} \tag{4.2}$$

where $\boldsymbol{F}_u$ and $\boldsymbol{F}_w$ are the tangent vectors along the u and w-axes, respectively.

Finally, the quasisurface $f_c(x, y, z)$ is formed in such a way that each point of the actual surface $f(x, y, z)$ is mapped along its normal vector $\boldsymbol{n}_f$ up to a distance proportional to its intensity value c_f (Figure 4e).

$$f_c(x, y, z) = f(x, y, z) + \boldsymbol{n}_f \lambda c_f \tag{4.3}$$

where λ is an appropriate scalar factor for the conversion from the intensity range to the Cartesian space.

Rather than the actual surface $f(x, y, z)$, the trend surface $F(u,w)$ can also be defined as the datum, which leads to

$$f_c(x, y, z) = F(u, w) + \boldsymbol{n}_f \lambda c_f \tag{4.4}$$

This isolates the geometric noise component from the quasisurface $f_c(x, y, z)$, but strongly smoothes the geometry.

Equations (4.3) and (4.4) assume a fairly simplistic radiometric model (intensities are mapped perpendicular to the geometric surface). This model can be refined by considering an appropriate illumination model.

The same procedure is performed for the search surface $g(x, y, z)$ as well:

$$g_c(x, y, z) = g(x, y, z) + \boldsymbol{n}_g \lambda c_g \tag{4.5}$$

4.2. Estimation model

Equation (3.2) should also be valid for the quasisurfaces under the assumption that similar illumination conditions exist for both the template and search surfaces:

$$f_c(x, y, z) - e_c(x, y, z) = g_c(x, y, z) \tag{4.6}$$

The random errors of the template and search quasisurfaces are assumed to be uncorrelated. The contrast and brightness differences or in the extreme case specular reflection will cause model errors, and deteriorate the reliability of the estimation. The radiometric variations between the template and search surface intensities should be reduced before matching by pre-processing or appropriate modeling in the estimation process by the use of extra parameters.

For two images of an object acquired by an optical-passive sensor, e.g. a CCD camera, an intensity transfer function such as $(c_f = r_0 + c_g r_1)$ could be suitable for the radiometric adaptation, where r_0 (shift) and r_1 (scale) are radiometric correction parameters. In the case of laser scanner derived

intensity images, the radiometric variations are strongly dependent on both the incident angle of the signal path with respect to the normal to the object surface and the object-to-sensor distance. Thus, for a plane type of object, the radiometric variations can be modeled in first approximation as in the following:

$$f_c(x,y,z) - e_c(x,y,z) = g_c(x,y,z) + r_0 + ur_1 \tag{4.7}$$

where u is the abscissa of the search trend surface $G(u,w)$, considering that the u-axis is the horizontal direction. In other words, the u-axis is the principal direction of change of the incident angles. Depending on the characteristics of the scan data, it can be replaced by the ordinate value w, or another type of parameterization. In general a second order bivariate polynomial ($r_0 + ur_1 + wr_2 + uwr_3 + u^2r_4 + w^2r_5 + u^2wr_6 + uw^2r_7 + u^2w^2r_8$) or an appropriate subpart of it can be used.

Although the radiometric parameters r_0 and r_1 are linear a priori, they are also expanded using the Taylor series. Equation (4.7) in linearized form gives:

$$-e_c(x,y,z) = \frac{g_c^0(x,y,z)}{\partial x}\,dx + \frac{g_c^0(x,y,z)}{\partial y}\,dy + \frac{g_c^0(x,y,z)}{\partial z}\,dz + dr_0 + u\,dr_1$$
$$- (f_c(x,y,z) - g_c^0(x,y,z) - \{r_0^0 + ur_1^0; \boldsymbol{n}_g\}) \tag{4.8}$$

with notations

$$g_{cx} = \frac{\partial g_c^0(x,y,z)}{\partial x} \quad , \quad g_{cy} = \frac{\partial g_c^0(x,y,z)}{\partial y} \quad , \quad g_{cz} = \frac{\partial g_c^0(x,y,z)}{\partial z} \tag{4.9}$$

where the terms $\{g_{cx}, g_{cy}, g_{cz}\}$ stand for the numerical derivatives of the search quasisurface function. The first approximations of the radiometric parameters are $r_0^0 = r_1^0 = 0$. At the end of each iteration, the search quasisurface $g_c^0(x, y, z)$ is transformed to a new state using the updated set of transformation parameters, and subsequently re-shaped by the current set of radiometric parameters $r_0^0 + ur_1^0$ along the normal vectors $\boldsymbol{n}_g$, which are calculated on the search trend surface $G(u,w)$.

The terms $\{dx, dy, dz\}$ relate the Equations (3.4) and (4.8) to each other.

The quasisurfaces are treated like actual surfaces in the estimation model. They contribute observation equations to the design matrix, joining the system by the same set of transformation parameters. After further expansion and with the assumptions $E\{\boldsymbol{e}_c\} = 0$ and $E\{\boldsymbol{e}_c \boldsymbol{e}_c^T\} = \sigma_0^2 \mathbf{P}_c^{-1}$, Equation (4.8) becomes

$$-\boldsymbol{e}_c = \mathbf{A}_c \boldsymbol{x} - \boldsymbol{l}_c \quad , \quad \mathbf{P}_c \tag{4.10}$$

where $\boldsymbol{e}_c$, $\mathbf{A}_c$, $\boldsymbol{x}$, and $\mathbf{P}_c$ are the true error vector, the design matrix, the parameter vector, and the associated weight coefficient matrix for the quasisurface observations, respectively, and $\boldsymbol{l}_c$ is the constant vector that contains the Euclidean distances between the template and corresponding search quasisurface elements. Here, the vector $\boldsymbol{x}$ is extended to include the radiometric parameters in addition to the transformation parameters.

The hybrid system in Equations (3.11), (3.13) and (4.10) is of the combined adjustment type that allows simultaneous matching of geometry and intensity. The Least Squares solution of the system gives

$$\hat{\boldsymbol{x}} = (\mathbf{A}^T\mathbf{P}\mathbf{A} + \mathbf{P}_b + \mathbf{A}_c^T\mathbf{P}_c\mathbf{A}_c)^{-1}(\mathbf{A}^T\mathbf{P}\boldsymbol{l} + \mathbf{P}_b\boldsymbol{l}_b + \mathbf{A}_c^T\mathbf{P}_c\boldsymbol{l}_c) \tag{4.11}$$

In the experiments, weights for the quasisurface observations are selected as $(\mathbf{P}_c)_{ii} < (\mathbf{P})_{ii}$, and the intensity measurements of the (laser) sensor are considered to be uncorrelated with the distance measurements ($E\{\boldsymbol{e}_c \boldsymbol{e}^T\} = 0$) for the sake of simplicity of the stochastic model.

5

FURTHER CONCEPTUAL EXTENSIONS

5.1. Least squares 3D curve matching

Assume that two 3D curves of the same object are either directly measured by use of a contact measurement device, photogrammetric method, etc. or derived using any other technique. They can be matched in 3D space, since they represent the same object (Figure 5). The curves may have been measured or extracted in a point by point fashion, but can also be in different sampling patterns. Matching is established, if the sum of the squares of the Euclidean distances between the two curves is minimized by applying a 3D transformation to the search curve.

The analytical representation of the curves is carried out in cubic spline form, but any other piecewise representation scheme can also be considered. In general, a parametric space curve is expressed, e.g. for the template curve, as:

$$f(u) = \begin{bmatrix} x(u) & y(u) & z(u) \end{bmatrix}^{\mathrm{T}} \tag{5.1}$$

where $u \in [0,1]$ and $f(u) \in \Re^3$ is the position vector of any point on the curve. It has three components $x(u)$, $y(u)$, and $z(u)$ which are considered as the Cartesian coordinates of the position vector (Rogers and Adams, 1976).
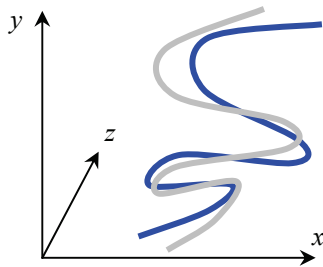
Figure 5. Matching of free-form space curves.

In the cubic spline representation

$$f(u) = \sum_{i=1}^{4} \boldsymbol{b}_i u^{i-1} = \boldsymbol{b}_1 + \boldsymbol{b}_2 u + \boldsymbol{b}_3 u^2 + \boldsymbol{b}_4 u^3 \tag{5.2}$$

the coefficient vectors $\boldsymbol{b}_i \in \Re^3$ are determined by specifying the boundary conditions for the spline segments. The expanded form shows a 4th order 3rd degree analytical definition. A cubic degree ensures the second-order continuity (C^2). This implies that the first (slope) and second (curvature) order derivatives are continuous across the joints of the composite curve. Similar expressions are also valid for the search curve:

$$g(u) = \boldsymbol{d}_1 + \boldsymbol{d}_2 u + \boldsymbol{d}_3 u^2 + \boldsymbol{d}_4 u^3 \tag{5.3}$$

Using the parametric 3D space curve definition, the observation equations are formulated in the same manner as explained in Chapter 3:

$$f(u) - e(u) = g(u) \tag{5.4}$$

Considering the same assumptions, which have been made in Chapter 3, with respect to the stochastic model, the geometric relationship between the template and search curves, and the Taylor expansion, the linearized functional model evolves as:

$$f(u) - e(u) = g^0(u) + \frac{\partial g^0(u)}{\partial u} \, \mathrm{d} u \tag{5.5}$$

$$f(u) - e(u) = g^0(u) + \frac{\partial g^0(u)}{\partial u} \frac{\partial u}{\partial x} \, \mathrm{d} x + \frac{\partial g^0(u)}{\partial u} \frac{\partial u}{\partial y} \, \mathrm{d} y + \frac{\partial g^0(u)}{\partial u} \frac{\partial u}{\partial z} \, \mathrm{d} z \tag{5.6}$$

The relations between the Cartesian coordinate domains of the template and search curves are established via a 7-parameter 3D similarity transformation, where it is also possible to extend or reduce the parameter space of the 3D transformation upon necessity.

The differentiation of the transformation equations results in:

$$\mathrm{d} x = \frac{\partial x}{\partial p_i} \, \mathrm{d} p_i \quad , \quad \mathrm{d} y = \frac{\partial y}{\partial p_i} \, \mathrm{d} p_i \quad , \quad \mathrm{d} z = \frac{\partial z}{\partial p_i} \, \mathrm{d} p_i \tag{5.7}$$

where $p_i \in \{t_x, t_y, t_z, m, \omega, \varphi, \kappa\}$ is the i-th transformation parameter in Equation (3.3).

The expression below

$$\frac{\partial g^0(u)}{\partial u} = \left[\frac{\partial g^0(u)}{\partial u} \frac{\partial u}{\partial x} \quad \frac{\partial g^0(u)}{\partial u} \frac{\partial u}{\partial y} \quad \frac{\partial g^0(u)}{\partial u} \frac{\partial u}{\partial z} \right]^{\mathrm{T}} = \begin{bmatrix} g_x & g_y & g_z \end{bmatrix}^{\mathrm{T}} \tag{5.8}$$

describes the numeric derivative terms. After further expansions, in the same manner as in Chapter 3, considering the parameters of the 3D transformation as fictitious observations, using an appropriate stochastic model, and with the assumptions $\mathrm{E}\{e\} = 0$ and $\mathrm{E}\{e\,e^{\mathrm{T}}\} = \sigma_0^2 \mathbf{P}^{-1}$, the system can be formulated as a Generalized Gauss-Markoff model:

$$-e = \mathbf{A}\,x - l \quad , \quad \mathbf{P} \tag{5.9}$$

$$-e_b = \mathbf{I}\,x - l_b \quad , \quad \mathbf{P}_b \tag{5.10}$$

The Least Squares solution of the joint system Equations (5.9) and (5.10) gives the unbiased minimum variance estimation for the parameters:

$$\hat{x} = (\mathbf{A}^{\mathrm{T}}\mathbf{P}\mathbf{A} + \mathbf{P}_b)^{-1}(A^{\mathrm{T}}\mathbf{P}l + \mathbf{P}_b l_b) \qquad \text{solution vector} \tag{5.11}$$

$$\hat{\sigma}_0^2 = v^{\mathrm{T}}\mathbf{P}v + v_b^{\mathrm{T}}\mathbf{P}_b v_b / r \qquad \text{variance factor} \tag{5.12}$$

$$v = \mathbf{A}\,\hat{x} - l \qquad \text{residual vector for curve observations} \tag{5.13}$$

$$v_b = \mathbf{I}\,\hat{x} - l_b \qquad \text{residual vector for parameter observations} \tag{5.14}$$

The functional model is non-linear, and the solution is iterative. The iteration stops if each element of the alteration vector $\hat{x}$ in Equation (5.11) falls below a certain limit.

Let us assume that the first three derivatives do exist and are linearly independent for a point $g(u)$ on a parametric curve (Figure 6). Then the first three derivatives $g'(u)$, $g''(u)$, and $g'''(u)$ form a local affine coordinate system with origin $g(u)$.
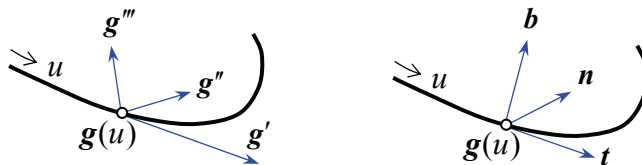
Figure 6. Local affine system (left) and Frenet frame (right) (adapted after Farin, 1997).

From this local affine system, one can easily obtain a local Cartesian system with origin $g(u)$ and axes t, n, b by the Gram-Schmidt process of orthonormalization (Farin, 1997):

$$t = \frac{g'}{\|g'\|} \quad , \quad b = \frac{g' \times g''}{\|g' \times g''\|} \quad , \quad n = b \times t \tag{5.15}$$

The vectors t, n, b are called tangent, (main) normal, and bi-normal vectors, respectively. The frame t, n, b is called moving trihedron or Frenet frame. It varies its orientation as u traces out the curve (Farin, 1997).

Considering this definition, the numeric 1st order derivative terms $\{g_x, g_y, g_z\}$ are the elements of the unit-length normal vector n at point $g(u)$.

$$\begin{bmatrix} g_x & g_y & g_z \end{bmatrix}^{\mathrm{T}} = n \tag{5.16}$$

Using the proper degree and basis for curve representation, our method can handle multi-resolution and multi-sensor data sets, including multi-scale curves. It can be straightforwardly re-formulated in 2D for the matching of free-form image features.

5.2. Matching of 3D curves with a 3D surface

The same formulation allows matching of one or more 3D curve(s) with a 3D surface simultaneously (Figure 7). The problem is finding the correspondence of a 1D geometric definition (curve) on a 2D geometric definition (surface), where both of them are parametrically represented in 3D space.
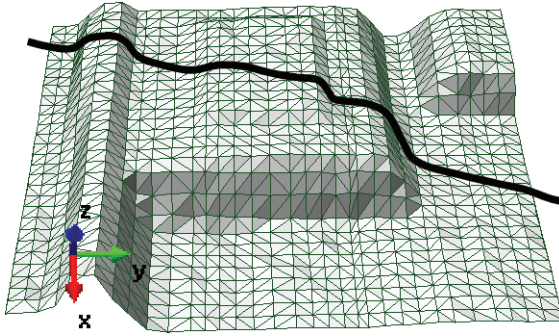
Figure 7. Matching of a 3D space curve with a 3D surface.

5.3. Matching of 3D sparse points with a 3D surface

The LS3D method can match a 3D surface to a sparse set of 3D points provided that they have sufficiently good distribution. A set of ground control points (GCP) could be a good example for this case. This extension can be especially useful for the orientation or georeferencing of digital surface models.

5.4. Generalized multiple 3D surface and intensity matching

Here, a method for the simultaneous co-registration and georeferencing of multiple 3D pointclouds and intensity information is proposed. It is a generalization of the 3D surface matching problem. The simultaneous co-registration provides for a strict solution to the problem, as opposed to sequential pairwise registration. The problem is formulated as the Least Squares matching of overlapping 3D surfaces. The parameters of 3D transformations of multiple surfaces are simultaneously estimated, using the Generalized Gauss-Markoff model, minimizing the sum of squares of the Euclidean distances among the surfaces. An observation equation is written for each surface-to-surface correspondence. Each overlapping surface pair contributes a group of observation equations to the design matrix.

The parameters are introduced into the system as stochastic variables, as a second type of (fictitious) observations. This extension allows to control the estimated parameters. Intensity information is introduced into the system in the form of quasisurfaces as the third type of observations. Reference points, defining an external (object) coordinate system, which are imaged in additional intensity images, or can be located in the pointcloud, serve as the fourth type of observations. They transform the whole block of "models" to a pre-defined reference system. The total system is solved by applying the Least Squares technique, provided that sufficiently good initial values for the transformation parameters are given.

5.4.1. Least squares multiple 3D surface matching

Assume a set of n surfaces of an object: $g_1(x, y, z)$,…, $g_n(x, y, z)$. The object is defined in a 3D Cartesian coordinate system, whereas the n surfaces are located in arbitrary local coordinate systems. The n surfaces are discrete 3D approximations of continuous function of object surface. They are digitized according to a sampling principle.

There are m mutual spatial overlaps between the surfaces $g_i(x, y, z)$. Every overlap satisfies a pairwise matching:

$$g_i(x, y, z) - e_i(x, y, z) = g_j(x, y, z) \quad , \quad i, j = 1,...,n \quad , \quad i \neq j \tag{5.17}$$

where $e_i(x, y, z)$ is a true error vector. It is assumed that i-th surface's noise is independent of j-th one.

Equations (5.17) are considered as nonlinear observation equations which model the observation vector $g_i(x, y, z)$ with functions $g_j(x, y, z)$. The Least Squares matching of the j-th surface to the i-th one is to be satisfied while the i-th surface is also subject to a 3D transformation (with respect to a predefined datum). This is the 3D case of the X-Y constraint version (i.e. grid sampling mode) of the multiphoto geometrically constrained matching (MPGC) (Gruen and Baltsavias, 1987) where both the template and the search image patches are transformed.

Both surfaces are transformed to an object coordinate system while minimizing a goal function, which measures the sum of the squares of the Euclidean distances between them. The geometric relationships are established via 7-parameter similarity transformations. They can be replaced by another type if needed.

In order to prevent the duplication, Equations (5.17) are written for every possible i-j pair where $i < j$.

Because Equations (5.17) are nonlinear, they are linearized by Taylor series expansion. They result in the following linear systems in matrix form

$$-e_1 = \mathbf{A}_1 x - l_1 \quad , \quad \mathbf{P}_1$$

$$-e_2 = \mathbf{A}_2 x - l_2 \quad , \quad \mathbf{P}_2 \tag{5.18}$$

$$\vdots \qquad \qquad \vdots$$

$$-e_m = \mathbf{A}_m x - l_m \quad , \quad \mathbf{P}_m$$

Equations (5.18) consist of m groups of observation equations. They can be combined under one sub-system as

$$-e = \mathbf{A}x - l \quad , \quad \mathbf{P} \tag{5.19}$$

where $\mathbf{A}$ is the design matrix, x is the parameter vector which contains n sets of transformation parameters, $\mathbf{P} = \mathbf{P}_{ll}$ is the a priori weight matrix, l is the discrepancies vector that consists of the Euclidean distances between the overlapping surfaces.

Provided that $m \geq n$ is satisfied, the sub-system (of the design matrix) consisting of m Equations (5.18) implicitly contains the multiple overlap conditions. However, the normal equation matrix explicitly shows all the spatial relationships by non-zero off-diagonal elements.

With the statistical expectation operator E{}, it is assumed that

$$E\{e\} = 0 \quad , \quad E\{ee^{\mathrm{T}}\} = \sigma_0^2 \mathbf{P}_{ll}^{-1} \tag{5.20}$$

The parameters are introduced into the system as observables with the associated weight coefficient matrix $\mathbf{P}_b$ as

$$-e_b = \mathbf{I}x - l_b \quad , \quad \mathbf{P}_b \tag{5.21}$$

where $\mathbf{I}$ is the identity matrix and l_b is the (fictitious) observation vector. The weight matrix $\mathbf{P}_b$ has to be chosen appropriately, considering a priori information of the parameters.

5.4.2. The generalized model with intensity matching and georeferencing

When some surfaces lack sufficient geometric information, their intensity information, if available, is introduced to the system. The intensity information is used to form the quasisurfaces in addition to the actual ones. The formation of the quasisurfaces is given in Chapter 4. The quasisurfaces are treated like actual surfaces in the estimation model. They contribute observation equations to the design matrix, joining the system by the same set of transformation parameters

$$-e_c = \mathbf{A}_c x - l_c \quad , \quad \mathbf{P}_c \tag{5.22}$$

where e_c, $\mathbf{A}_c$ and $\mathbf{P}_c$ are the true error vector, the design matrix, and the associated weight coefficient matrix for the quasisurface observations, respectively, and l_c is the constant vector that contains the Euclidean distances between the corresponding quasisurface elements.

Reference points whose coordinates are defined in an external (object) coordinate system, which are imaged in additional intensity images, or can be located in the pointcloud, serve as the fourth type of observations. They are formulated as 3D transformations from local pointcloud systems to the object coordinate system in linearized matrix form

$$e_d = \mathbf{A}_d x - l_d \quad , \quad \mathbf{P}_d \tag{5.23}$$

where $\mathbf{A}_d$ is the design matrix, $\mathbf{P}_d$ is the associated weight matrix, and l_d is the discrepancies vector which contains the coordinate value differences of the reference points between the transformed local system and object coordinate system.

Equations (5.23) eliminate the datum deficiency existing in Equations (5.19). Alternatively, the datum constraints can be imposed by fixing the minimal number of parameters in Equations (5.21).

The hybrid system in Equations (5.19), (5.21), (5.22) and (5.23) is of the combined adjustment type that allows simultaneous matching of geometry and intensity and additionally georeferencing of multiple 3D surfaces. The Least Squares solution of the system gives the solution vector as

$$\hat{x} = (\mathbf{A}^{\mathrm{T}}\mathbf{P}\mathbf{A} + \mathbf{P}_b + \mathbf{A}_c^{\mathrm{T}}\mathbf{P}_c\mathbf{A}_c + \mathbf{A}_d^{\mathrm{T}}\mathbf{P}_d\mathbf{A}_d)^{-1}(\mathbf{A}^{\mathrm{T}}\mathbf{P}l + \mathbf{P}_b l_b + \mathbf{A}_c^{\mathrm{T}}\mathbf{P}_c l_c + \mathbf{A}_d^{\mathrm{T}}\mathbf{P}_d l_d) \tag{5.24}$$

and the variance factor as

$$\hat{\sigma}_0^2 = \frac{v^{\mathrm{T}}\mathbf{P}v + v_b^{\mathrm{T}}\mathbf{P}_b v_b + v_c^{\mathrm{T}}\mathbf{P}_c v_c + v_d^{\mathrm{T}}\mathbf{P}_d v_d}{r} \tag{5.25}$$

where r is the system redundancy, v, v_b, v_c and v_d are residual vectors for actual surface observations, parameter observations, quasisurface observations and reference point observations, respectively.

The estimation model is the Generalized Gauss-Markoff, which can accommodate any kind of functional constraint flexibly, e.g. concentric scans, certain rotational differences, parallel or perpendicular objects in the scan data, etc.

6

EXPERIMENTAL RESULTS

Empirical results are given to verify the theory of the proposed approach. All experiments were carried out using self-developed C/C++ software (called LS3D) that runs on Microsoft Windows® OS.

In most experiments (except the examples "human face", "Tucume", "SRTM TerrainScape", "DMC", "deforestation" and "SRTM C-Band DEMs") the initial approximations of the unknowns were provided by interactively selecting 3 common points on both surfaces before matching. Since in all data sets there was no scale difference, the scale factor was fixed to unity. The iteration criteria values were given in Table 1. They vary according to the unit and resolution of the data and size of the object volume.

Table 1. The iteration criteria values for the elements of the translation vector and the rotation angles.

Experiment name	dω, dφ, dκ	dt_x , dt_y , dt_z
6.1.1. Human face	1.0e−3 grad	1.0e−2 millimeters
6.1.2. Industrial plant	1.0e−3 grad	1.0e−4 meters
6.1.3. Newspaper	1.0e−3 grad	1.0e−3 millimeters
6.1.4. Tucume	1.0e−3 grad	1.0e−1 meters
6.1.5. Bas-relief	1.0e−3 grad	1.0e−4 meters
6.2.1. Ball	5.0e−3 grad	2.0e−4 millimeters
6.2.2. Wall painting	5.0e−3 grad	2.0e−4 millimeters
6.3.1. Chapel	1.0e−3 grad	1.0e−4 meters
6.3.2. Weary Herakles	1.0e−3 grad	1.0e−4 millimeters
6.3.3. Khmer head	1.0e−3 grad	1.0e−4 millimeters
6.3.4. Pinchango Alto	1.0e−3 grad	1.0e−3 meters
6.3.5. SRTM TerrainScape	Na	Na
6.3.6. DMC DSM accuracy evaluation	1.0e−3 grad	1.0e−2 meters
6.3.7. Deforestation analysis	1.0e−3 grad	1.0e−4 meters
6.3.8. Validation of SRTM C-Band DEMs	1.0e−3 grad	1.0e−2 meters

6.1. Experiments for the basic algorithm

6.1.1. Human face

The first experiment is the registration of three surface patches, which were photogrammetrically measured 3D pointclouds of a human face from multi-images (Figure 8). The average point spacing is 1.5 millimeters. For the mathematical and implementation details of this automatic surface measurement method, the author refers to D'Apuzzo (2002).

Left and right surfaces (Figure 8a and 8c) were matched to the center surface (Figure 8b) by use of the basic algorithm of the LS3D method. Since the data set already came in a common coordinate system, the rotation angles (ω, φ, κ) were deteriorated by ~10^g prior to the first iteration. Numerical results of the matching of the left and the right surfaces are given in parts I and II of Table 2, respectively. In Table 2, "No. of points" column stands for the number of the remaining correspondences at the last iteration, resulting from a simple robust estimation principle (Equation 3.31), which aims to eliminate only the large outliers and occlusions.
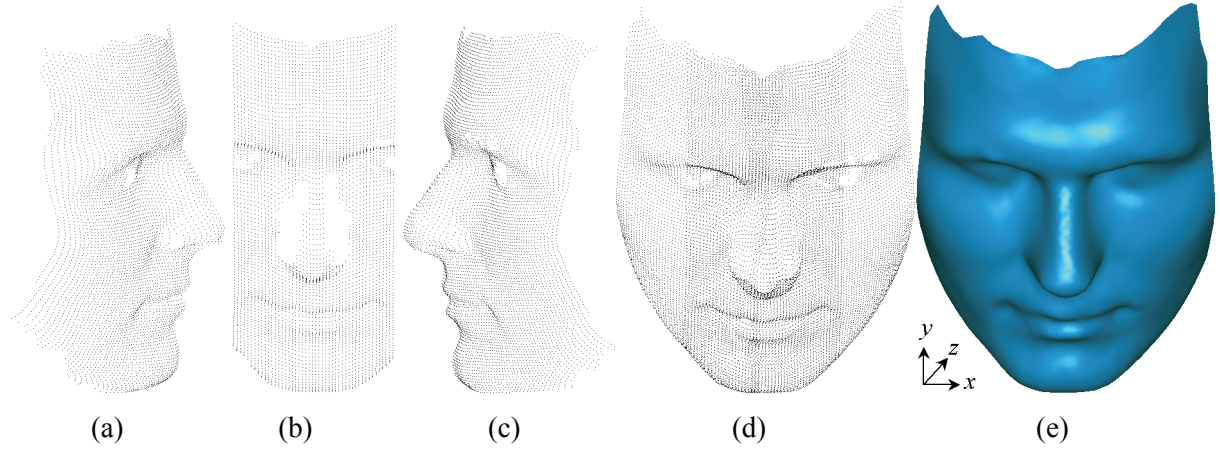
Figure 8. Experiment "human face". (a) Left-search surface, (b) center-template surface, (c) right-search surface, (d) obtained 3D pointcloud after LS3D surface matching, (e) shaded view of the final composite surface.

Relatively high standard deviations for the estimated t_x and φ (note that a high physical correlation between t_x and φ due to axes configuration occurs) are due to the narrow overlapping area along the *x*-axis. Nevertheless, the matching result is good. The estimated σ_0 values prove the accuracy potential of the surface measurement method, given as 0.2 mm by D'Apuzzo (2002). Since the LS3D surface matching method reveals the sensor noise level and accuracy potential of any kind of surface measurement method or device, it can also be used for comparison and validation studies.

Table 2: Numerical results of "human face" experiment.

#	Surface type	No. of points	No. of observation equations $(n_l + n_b + n_c)$	No. of iterations	$\hat{\sigma}_0$ (mm)	$\hat{\sigma}_{tx} / \hat{\sigma}_{ty} / \hat{\sigma}_{tz}$ (mm)	$\hat{\sigma}_\omega / \hat{\sigma}_\varphi / \hat{\sigma}_\kappa$ (1.0e-02 gon)
I	P	2 497	2 497 + 7 + 0	7	0.19	0.15 / 0.07 / 0.05	0.96 / 2.44 / 1.90
	B			7	0.19	0.15 / 0.07 / 0.05	0.96 / 2.42 / 1.91
II	P	3 285	3 285 + 7 + 0	6	0.21	0.13 / 0.03 / 0.05	0.68 / 2.25 / 1.73
	B			6	0.21	0.13 / 0.03 / 0.05	0.69 / 2.26 / 1.75

P: Plane surface representation in triangle mesh form.
B: Bi-linear surface representation in grid mesh form.
n_l, n_b, n_c: Number of observation equations for actual surfaces, parameters and quasisurfaces, respectively.

6.1.2. Industrial plant

The second experiment is the registration of three pointclouds of an industrial plant (Figure 9). The scanning was performed by the HDS 2500 (Leica Geosystems) laser scanner. The average point spacing is 12 millimeters. The data set is courtesy of Leica Geosystems.

The first and third pointclouds (Figure 9a and 9c) were matched to the second one (Figure 9b) using the basic algorithm of the LS3D surface matching method. The numerical results of the matching of the first and third pointclouds are given in parts III and IV of Table 3, respectively.

Even though it is a very complex environment with many occlusions, the matching process is successful. Small magnitudes of the theoretical precisions of the parameters indicate a proper fit along all directions. This example shows that the basic algorithm can successfully find the solution in the presence of sufficient surface geometry.

However, the theoretical precisions are optimistic. They are much beyond the accuracy limit of the sensor. In order to see the effect of the redundancy on the theoretical precision values, a further matching process was carried out. Rather than the whole overlapping areas, occlusion-free cooperative subpatches (5 subpatches on the first pointcloud and 7 subpatches on the third pointcloud) were matched. The results are given in parts III" and IV" of Table 3. Although the precision values increased, they are still optimistic, mainly due to the stochastic properties of the search surfaces that

have not been considered as such in the estimation model, as is typically done in Least Squares matching. The explanation is given in Chapter 3.4.

(a)   (b)   (c)

(d)
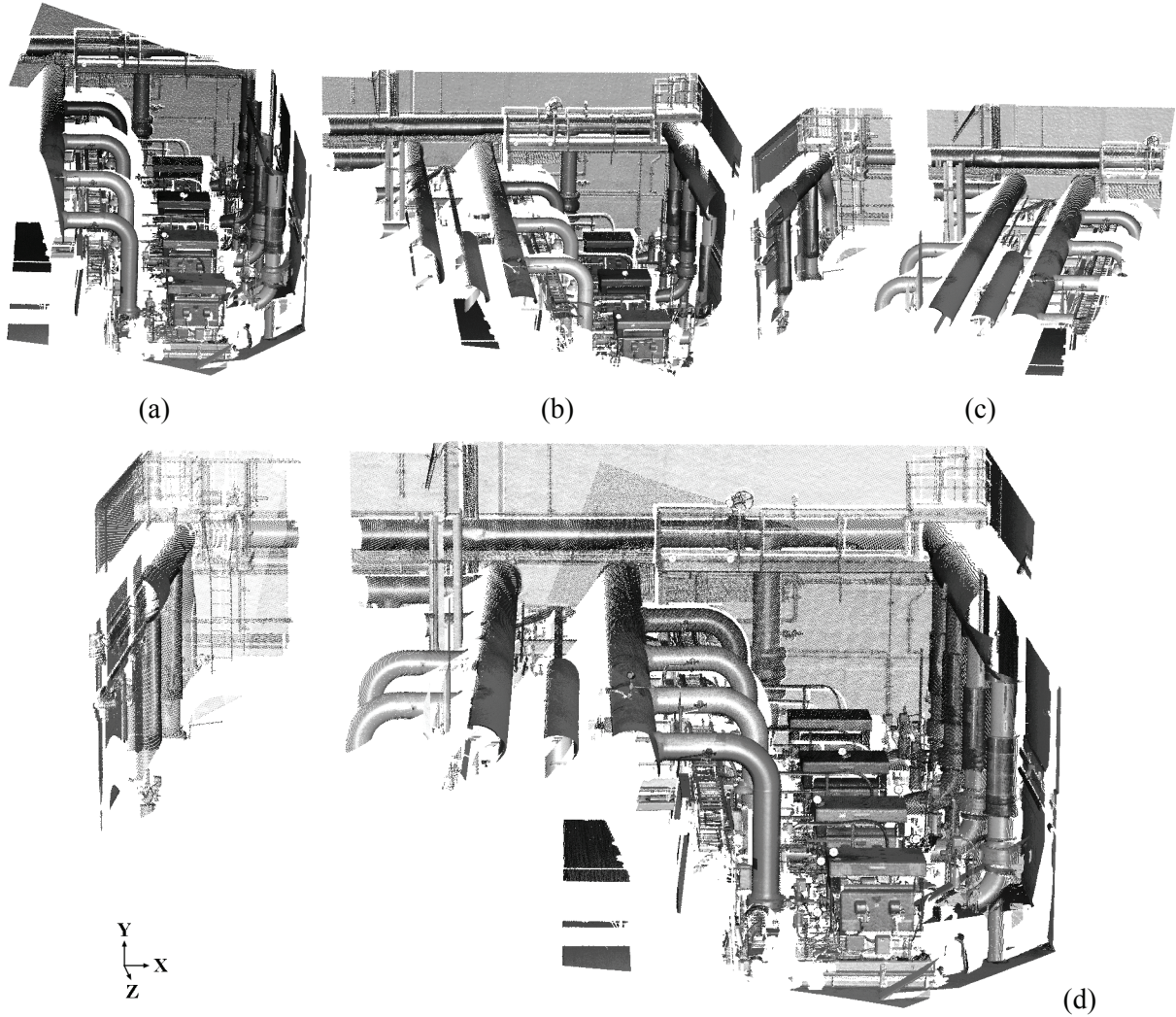
Figure 9. Experiment "industrial plant". (a), (b), (c) First, second and third pointcloud, (d) composite pointcloud after the LS3D surface matching. Note that laser scanner derived intensities are back-projected onto the pointclouds only for the purpose of visualization.

Table 3: Numerical results of "industrial plant" experiment.

#	Surface type	No. of points	No. of observation equations $(n_l + n_b + n_c)$	No. of iterations	$\hat{\sigma}_0$ (mm)	$\hat{\sigma}_{tx}$ / $\hat{\sigma}_{ty}$ / $\hat{\sigma}_{tz}$ (mm)	$\hat{\sigma}_{\omega}$ / $\hat{\sigma}_{\varphi}$ / $\hat{\sigma}_{\kappa}$ (1.0e-02 gon)
III	P	245 041	245 041 + 7 + 0	6	2.78	0.03 / 0.03 / 0.01	0.01 / 0.01 / 0.03
	B			5	2.79	0.03 / 0.03 / 0.01	0.01 / 0.01 / 0.03
IV	P	323 936	323 936 + 7 + 0	7	2.54	0.02 / 0.02 / 0.01	0.01 / 0.01 / 0.02
	B			6	2.52	0.02 / 0.02 / 0.01	0.01 / 0.01 / 0.02
III"	P	20 407	20 407 + 7 + 0	6	2.11	0.09 / 0.09 / 0.04	0.05 / 0.04 / 0.08
	B			5	2.09	0.09 / 0.09 / 0.04	0.05 / 0.04 / 0.08
IV"	P	37 983	37 983 + 7 + 0	8	2.01	0.04 / 0.04 / 0.02	0.03 / 0.03 / 0.07
	B			8	2.00	0.04 / 0.05 / 0.02	0.03 / 0.03 / 0.07

6.1.3. Newspaper

The third experiment is the registration of two pointclouds of a newspaper page (Figure 10). The scanning was performed by using the stereoSCAN[3D] system developed by Breuckmann GmbH (Germany). It is a high accurate scanner system based on the fringe projection technique

(Breuckmann, 2003). The average point spacing is 150 ~ 170 microns. The surface of Figure 10b was matched to the one in Figure 10d by use of LS3D surface matching. The numerical results of the matching are given in part V of Table 4. The data set is courtesy of Breuckmann GmbH.

Figure 10. Experiment "newspaper". The search surface textured (a) and grey-shaded (b), the template surface textured (c) and grey-shaded (d), shaded view of the final composite surface after the LS3D surface matching (e). Zoom-in part of (e) shows the range artifacts due to intensity discontinuities. Note that the scanner derived intensities are back-projected onto the surfaces (a) and (c) only for the visualization purposes.
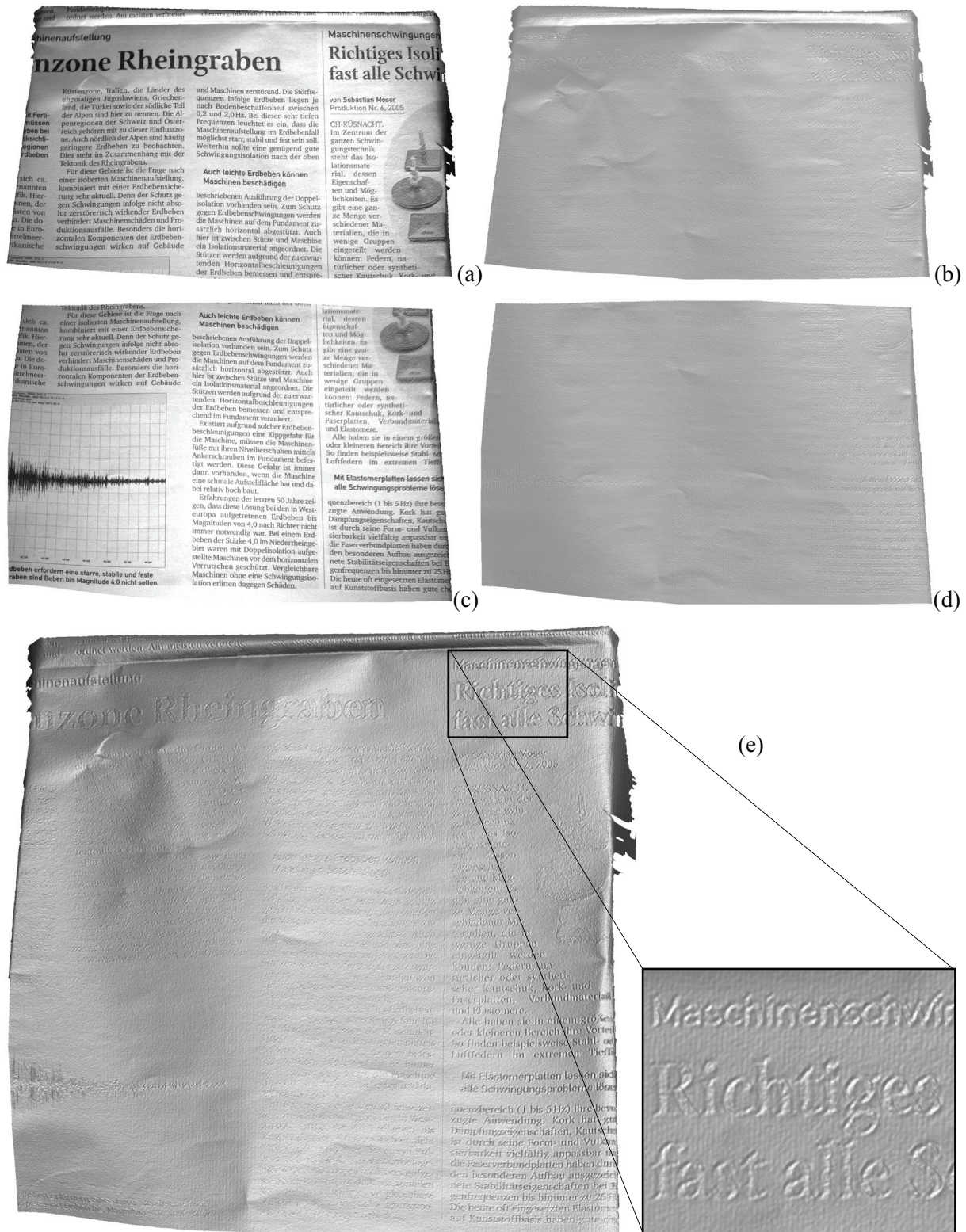
Although it is a difficult example due to very little changes in surface curvature, the matching is successful (Figure 10e). The a posteriori sigma value was 11.3 microns, with 13 iterations in 36.7 seconds (for the triangle mesh type of surface representation) on an Intel® P4 2.53 GHz PC. Interestingly, the letters are clearly visible on the surface model (Figure 10e). However, they are due to range artifacts created by the pixel-discretization on the chip level, leading to intensity discontinuities. For a detailed discussion of the range artifacts we refer to Blais et al. (2005).

Table 4: Numerical results of "newspaper" experiment.

#	Surface type	No. of points	No. of observation equations ($n_l + n_b + n_c$)	No. of iterations	$\hat{\sigma}_0$ (µm)	$\hat{\sigma}_{tx} / \hat{\sigma}_{ty} / \hat{\sigma}_{tz}$ (µm)	$\hat{\sigma}_\omega / \hat{\sigma}_\varphi / \hat{\sigma}_\kappa$ (1.0e-03 gon)
V	P	377 234	377 234 + 7 + 0	13	11.3	0.3 / 0.4 / 0.1	0.10 / 0.03 / 0.41
	B			12	11.3	0.3 / 0.4 / 0.1	0.10 / 0.03 / 0.42

A comparison against the non-accelerated version was made. The non-accelerated version exhaustively searches the correspondence in a large portion of the search surface during the first few iterations. In the following iterations it uses the same adaptive local neighborhood search as in the accelerated version. For a fair comparison, the same number of points was employed in the matching. The non-accelerated version found the same solution in 106.1 seconds. As seen in this experiment, the accelerated version speeds the computation up typically by a factor 2 to 3. This is the sole effect of the space partitioning technique.

6.1.4. Tucume

The forth experiment is the matching of two photogrammetrically derived DTMs of an area in Tucume (Peru). The horizontal resolution of the DTMs is 5 meters. The DTMs were manually measured as two independent models from 1:10 000 scaled B/W aerial images in one strip at an overlap of 60% in-flight direction. The mass points, in parallel profiles mode with a sampling distance of 20 meters, and breaklines were measured on an analytical stereoplotter WILD S9, and subsequently interpolated to a regular grid with a mesh size of 5 meters. More details are given in Sauerbier et al. (2004).

Although it is only a 2.5D model, it is a good example for the weak data configuration case since the overlapping area is relatively narrow with little information regarding to the surface geometry (Figure 11a). The numerical results of the basic algorithm of the LS3D matching are given in Table 5.

The large number of iterations and high standard deviations for the estimated parameters t_y, ω and κ obviously reflect the existence of the configuration problem, nevertheless the matching process is successful. Note that the theoretical precision of the y element of the translation vector is comparable to the DTM resolution. The residuals between the fixed and transformed surfaces show a random distribution pattern, except some occasional measurement and modeling errors (Figure 11b). In this experiment surface geometry alone is enough to obtain an acceptable solution, even if it contains only little information.

Table 5: Numerical results of "Tucume" experiment.

#	Surface type	No. of points	No. of observation equations ($n_l + n_b + n_c$)	No. of iterations	$\hat{\sigma}_0$ (m)	$\hat{\sigma}_{tx} / \hat{\sigma}_{ty} / \hat{\sigma}_{tz}$ (m)	$\hat{\sigma}_\omega / \hat{\sigma}_\varphi / \hat{\sigma}_\kappa$ (1.0e-02 gon)
VI	P	12 660	12 660 + 7 + 0	17	1.38	0.16 / 2.74 / 0.20	1.83 / 0.29 / 2.11
	B			15	1.38	0.16 / 2.85 / 0.20	1.84 / 0.30 / 2.19

A comparison study between the LS3D and ICP was carried out. The registration module of the Geomagic Studio v.6 (Raindrop Geomagic, Inc.) was used as the ICP implementation. Since a statistical evaluation was not available from Geomagic Studio, we compared the residuals between the fixed and transformed surfaces (Figure 11b and 11c). Both methods show a similar distribution pattern of residuals, but the LS3D gives a slightly better RMS error (1.34 meters) than the ICP (1.42 meters).

(a)

(b)

(c)

(d)
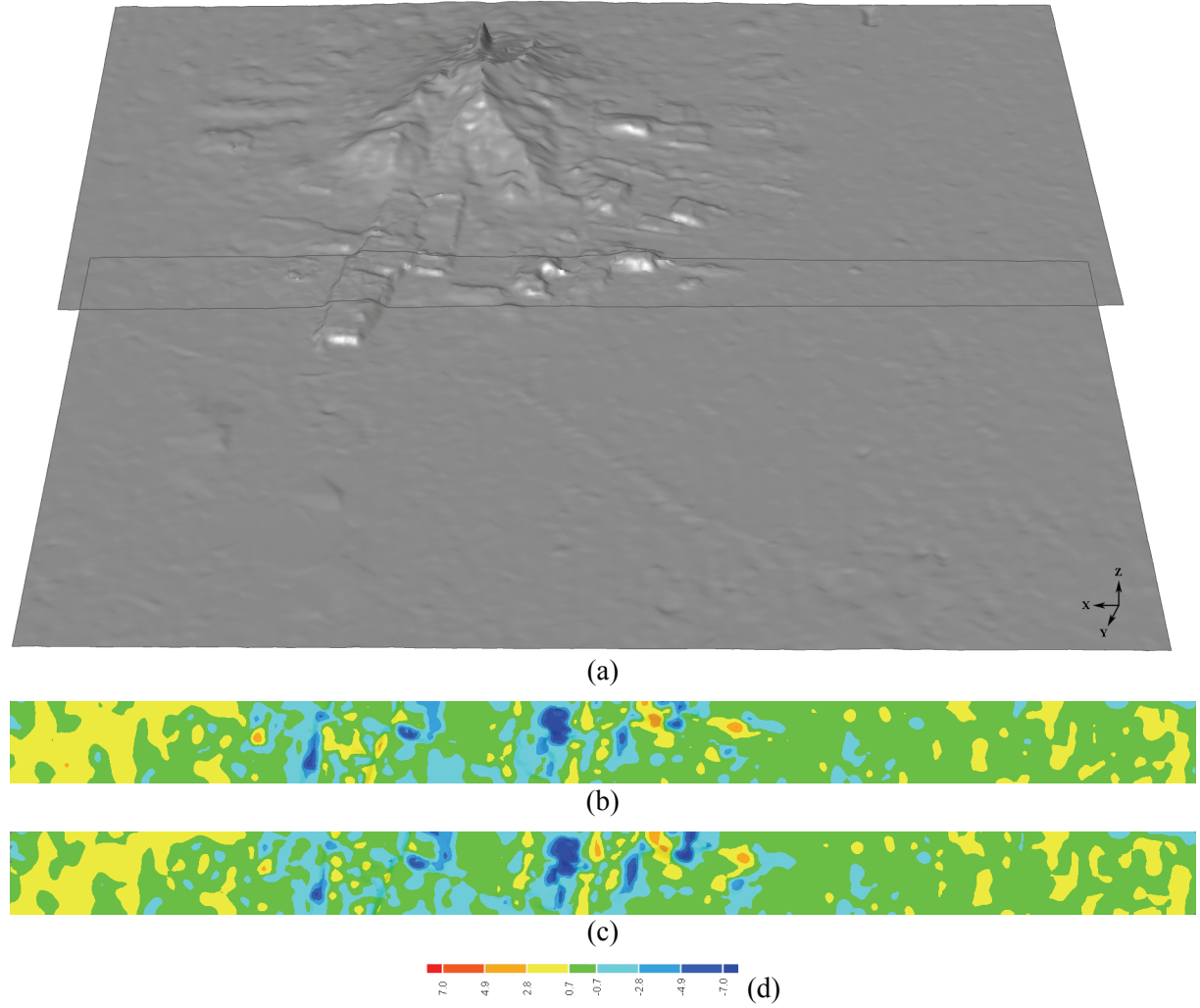
Figure 11. Experiment "Tucume". (a) The shaded view of the final composite surface after the LS3D surface matching. Note that the overlapping area is delineated by gray borderlines. The colored residuals between the fixed and transformed surfaces after the LS3D matching (b) and the ICP matching (c). The residuals bar unit is meter (d).

6.1.5. Bas-relief

The fifth experiment refers to the matching of two overlapping 3D point clouds (Figure 12), which represent a bas-relief on the wall of a chapel in Wangen, Germany. They were scanned using the IMAGER 5003 terrestrial laser scanner (Zoller+Fröhlich, Germany). Obtained results are given in part VII of Table 6. The data set is courtesy of Zoller+Fröhlich.

In the depth direction, matching can be easily achieved, but in the lateral direction it is problematic due to little change in surface geometry, which is around 3-4 cm. In spite of this difficult data configuration, the matching is successful. Relatively low theoretical precisions of the κ angle and the x, y elements of the translation vector reveal the presence of the problem. On the other hand, good theoretical precision for t_z proves the excellent fit along the depth direction.

Table 6: Numerical results of "bas-relief" experiment.

#	Surface type	No. of points	No. of observation equations ($n_l + n_b + n_c$)	No. of iterations	$\hat{\sigma}_0$ (mm)	$\hat{\sigma}_{tx} / \hat{\sigma}_{ty} / \hat{\sigma}_{tz}$ (mm)	$\hat{\sigma}_{\omega} / \hat{\sigma}_{\varphi} / \hat{\sigma}_{\kappa}$ (1.0e-02 gon)
VII	P	31 520	31 520 + 7 + 0	10	2.45	0.22 / 0.16 / 0.07	0.24 / 0.27 / 0.48
	B			9	2.46	0.22 / 0.16 / 0.07	0.25 / 0.27 / 0.53

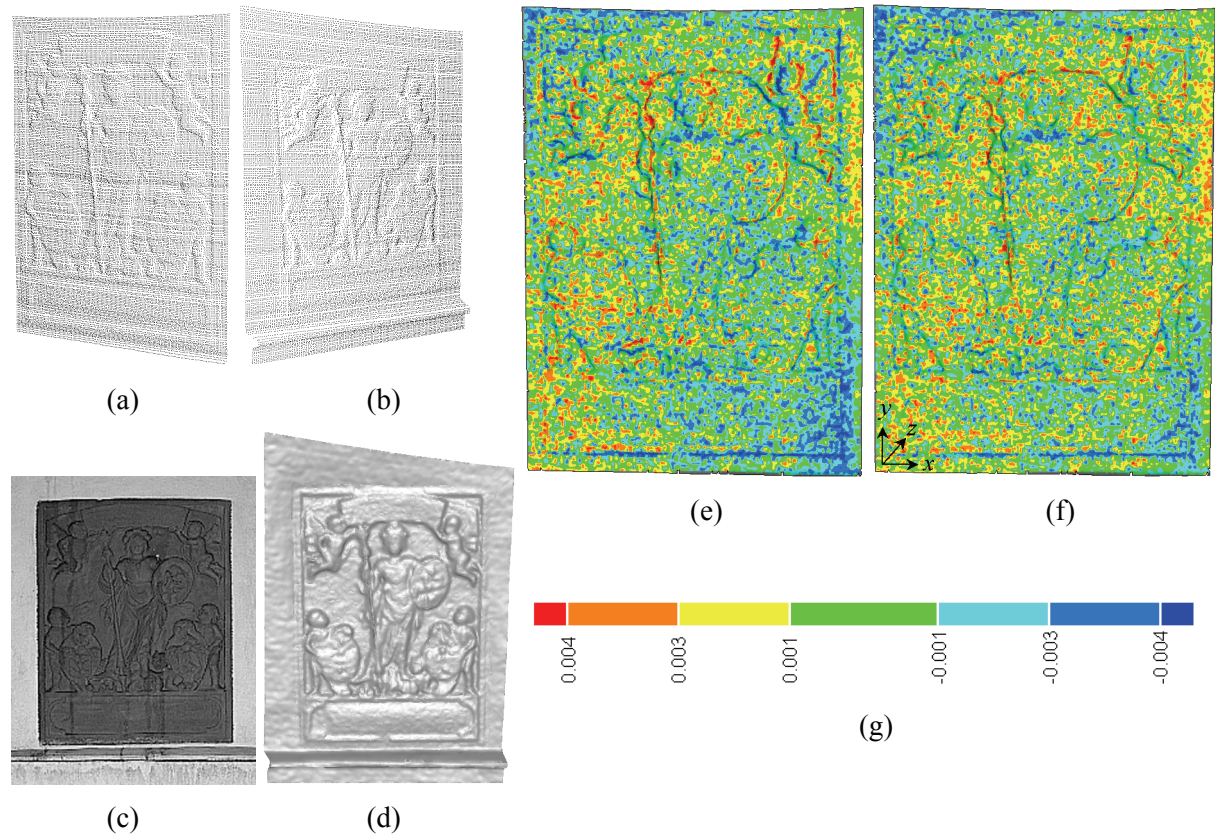Figure 12. Example "bas-relief". (a) Template surface, (b) search surface, (c) intensity image of the bas-relief (not used in matching), (d) final composite of the template and search surfaces after the LS3D matching method, (e) colored residuals between the fixed and transformed surfaces after the ICP method and (f) the LS3D surface matching method, (g) the residual bar unit is millimeter.

A comparison between the LS3D and ICP methods was carried out as well. The "registration" module of the Geomagic Studio v.6 (Raindrop Geomagic, Inc.) was used as the ICP implementation. The fixed and floating (to be transformed) surfaces were selected as template and search surfaces, respectively. The initial approximations were given by interactively selecting 3 common points on both surfaces as identical to both procedures. Since statistical results regarding the quality of the registration were not available from the Geomagic Studio, we compared the residuals between fixed and transformed surfaces using the "3D compare" module of the same software (Figure 12e and 12f). Our proposed method gives a slightly better result than the ICP considering the distribution pattern and the magnitudes of the residuals. The RMS error between the surfaces after the ICP matching is 2.55 mm, and after the LS3D matching 2.40 mm.

6.2. Experiments on the simultaneous matching of surface geometry and intensity

6.2.1. Ball

The sixth experiment refers to simultaneous matching of surface geometry and intensity. A soccer ball (Figure 13) was scanned using the IMAGER 5003 (Zoller+Fröhlich) laser scanner. The average point spacing is 2 millimeters.

Laser scanner derived reflectance values were used as intensity information. The intensities of the template and search surfaces were adapted by pre-processing prior to the matching. However, it was not possible to fully adjust the radiometric variations. This degrades the quality of the quasisurfaces. The actual surface observations were considered as having the unit weight $(\mathbf{P})_{ii} = 1$. Consequently, weights for the quasisurfaces observations were selected as $(\mathbf{P}_c)_{ii} = 0.2$. The numerical results are

given in part VIII of Table 7. In Table 7, the numbers of equations for the actual surface and quasisurface observations differ. Although they are the same at the beginning, during the iteration observations of the actual and quasisurfaces containing gross errors are excluded by the aforementioned robust estimation principle, resulting in a different number of equations for the two surfaces.
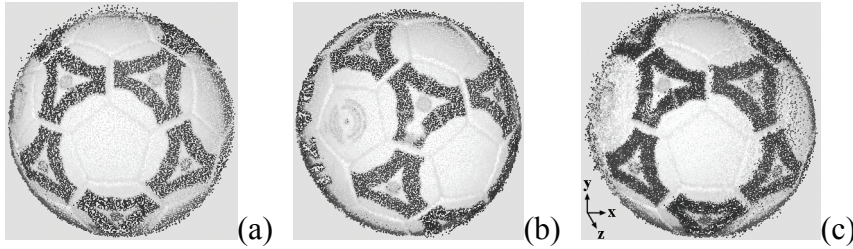

Figure 13. Experiment "ball". (a) The search pointcloud, (b) the template pointcloud, (c) the composite pointcloud after the combined matching of geometry and intensity. Note that laser scanner derived intensities are back-projected onto the pointclouds.

The slow convergence and slightly high standard deviation values are the result of the low data quality. Actually, the test object is not suitable for measuring by a medium-range laser scanner due to its non-diffuse reflectance property. This caused noisy and erroneous points in the range data, especially along the object silhouettes, and specular reflections in the intensity data.

For the purpose of comparison, the same experiment was run with only the surface geometry option of the LS3D matching method. An identical solution vector was found but apparently with poorer theoretical precision values: for the translation parameters 2.3, 2.9 and 1.5 millimeters and for the rotation angles 26.7^c, 18.1^c and 16.0^c along the x-y-z axes, respectively (part VIII" of Table 7). In fact, the test object does not have an ideal spherical shape. The shallow slots at the junctions of the pentagon parts of the ball (Figure 13) prevent the failure of only the surface geometry option.

Table 7: Numerical results of "ball" example.

#	Surface type	No. of points	No. of observation equations $(n_l + n_b + n_c)$	No. of iterations	RMSE (mm)	$\hat{\sigma}_{tx} / \hat{\sigma}_{ty} / \hat{\sigma}_{tz}$ (mm)	$\hat{\sigma}_{\omega} / \hat{\sigma}_{\varphi} / \hat{\sigma}_{\kappa}$ (1.0e-02 gon)
VIII [a]	P	2 548	2 548 + 7 + 2 617	12	1.14	1.2 / 1.6 / 0.8	14.5 / 9.7 / 9.3
	B			14	1.11	1.2 / 1.5 / 0.8	13.9 / 9.3 / 8.9
VIII"	P	2 589	2 589 + 7 + 0	21	1.70	2.3 / 2.9 / 1.5	26.7 / 18.1 / 16.0
	B			22	1.50	2.0 / 2.6 / 1.3	24.4 / 15.7 / 13.9

RMSE: root mean square error of the residuals of the actual surface observations.
[a]) datum is the actual surface $f/g (x, y, z)$.

6.2.2. Wall painting

The seventh experiment is the matching of two partial scans of a wall painting in Neuschwanstein Castle in Bavaria, Germany (Figure 14). The scanning was performed using the IMAGER 5003 terrestrial laser scanner. The average point spacing is 5 millimeters. The data set is courtesy of Zoller+Fröhlich.

The search surface (Figure 14a) was matched to the template one (Figure 14b) by simultaneous use of surface geometry and intensity information. Laser scanner derived reflectance values were used as intensity information. The weights were selected for the actual surface observations as $(\mathbf{P})_{ii} = 1$ and for the quasisurface observations as $(\mathbf{P}_c)_{ii} = 0.75$. The numerical results are given in parts IX and X of Table 8.

Since the object is a plane, surface geometry alone is not enough for the matching. Using the combined approach of matching surface geometry and intensity of the LS3D, a successful solution has been achieved. The generated quasisurfaces (Figure 14c and 14d) have been used in addition to the actual ones (Figure 14a and 14b) in the matching process. The radiometric variations between the

template and search surface intensities were modeled in the estimation by two extra parameters r_0 (shift) and r_1 (scale). The use of the trend surface as datum gives a slightly better convergence rate.

(a)	(b)	(c)	(d)

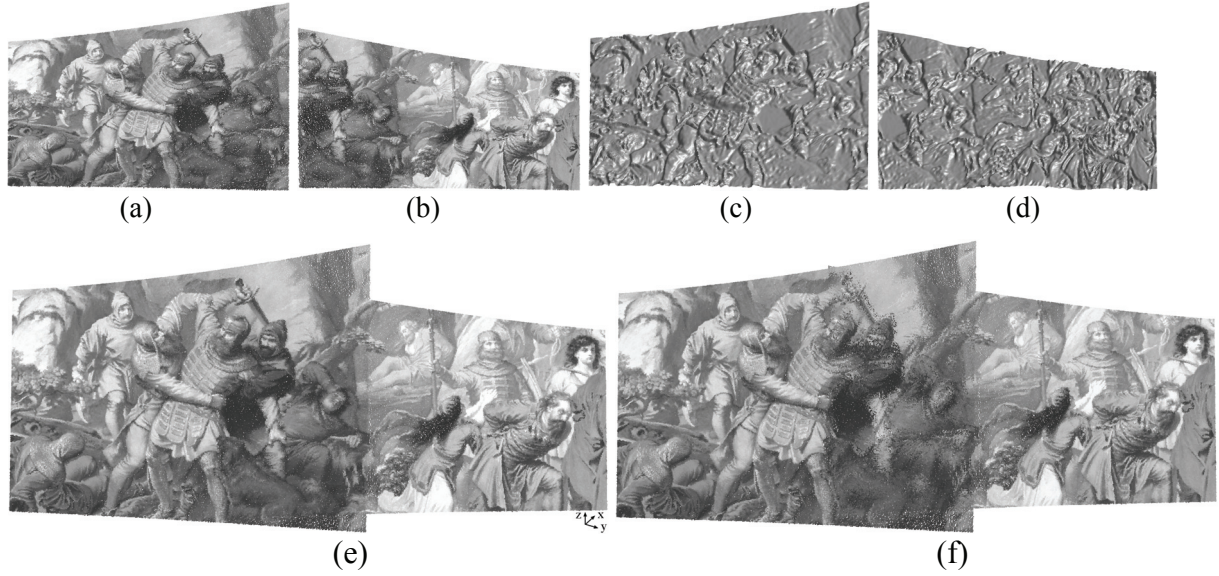|	
(e)	(f)

Figure 14. Experiment "wall painting". Actual (a) search and (b) template surfaces, generated (c) search and (d) template quasisurfaces, (e) composite pointcloud after the simultaneous matching of geometry and intensity by LS3D, (f) result of matching of only surface geometry by LS3D. Note that laser scanner derived intensities are back-projected onto the pointclouds (a), (b), (e) and (f).

Another comparison has been made by matching the same data set using the basic algorithm of the LS3D surface matching method. It immediately converged to the closest local minimum of the initial approximations, hence to a false solution. The existing noise in the data avoids the singularity of the normal equations matrix. Although the matching along the depth direction is correct, there is an incorrect solution along the lateral direction due to ambiguity of the surface information (Figure 14f). The theoretical precisions are slightly worse than those given in parts IX and X of Table 8, i.e. 0.03, 0.22 and 0.16 millimeters for the translation parameters and 0.37^c, 0.35^c and 0.46^c for the rotation angles along the x-y-z axes, respectively (part X" of Table 8). The differences are not significant, but consistent. The depth direction related parameters t_x, t_y and κ show almost the same values with respect to the values produced by the joint use of surface geometry and intensity, as expected, whereas the lateral direction related parameters obviously have greater magnitude.

Table 8: Numerical results of "wall painting" example.

#	Surface type	No. of points	No. of observation equations ($n_l + n_b + n_c$)	No. of iterations	$\hat{\sigma}_0$ (mm)	$\hat{\sigma}_{tx} / \hat{\sigma}_{ty} / \hat{\sigma}_{tz}$ (mm)	$\hat{\sigma}_\omega / \hat{\sigma}_\varphi / \hat{\sigma}_\kappa$ (1.0e-02 gon)
IX [a]	P	31 859	31 859 + 9 + 31 852	14	1.67	0.02 / 0.21 / 0.12	0.28 / 0.25 / 0.46
	B			13	1.72	0.02 / 0.21 / 0.12	0.29 / 0.26 / 0.44
X [b]	P	31 858	31 858 + 7 + 31 843	13	1.68	0.02 / 0.19 / 0.11	0.25 / 0.23 / 0.41
	B			12	1.73	0.02 / 0.19 / 0.11	0.26 / 0.24 / 0.40
X"	P	31 842	31 842 + 7 + 0	4	1.72	0.03 / 0.22 / 0.16	0.37 / 0.35 / 0.46
	B			3	1.77	0.03 / 0.21 / 0.18	0.42 / 0.38 / 0.45

[b]) datum is the actual surface F /G (u, w).

6.3. Diverse applications

6.3.1. Chapel – 3D object modeling

The object is a chapel, which is located in Wangen, Germany. It is around 20x9 meters in size. The data set consists of 14 pointclouds, which were acquired by the IMAGER 5003 terrestrial laser

scanner. Each scan file contains 2.64 million points. The average point spacing is around 1-2 cm. The data set is courtesy of Zoller+Fröhlich. The experiment was carried out on an Intel® P4 2.53 GHz PC.

Fourteen consecutive matching processes were performed using the simultaneous multi-subpatch approach of the LS3D matching method. The results are given in Table 9.

One of the scans was selected as the reference, which defines the datum of the common coordinate system. Since it is a closed object, there is need for a global registration, which distributes the residuals evenly among all of the scans, and also considers the closure condition, i.e. matching of the last scan to the first one. For this purpose we used the block adjustment by independent model solution. In the LS3D matching processes, the final correspondences were saved to separate files. Then all these files were given as input to a block adjustment by independent model procedure, which concluded with 1.6 mm a posteriori sigma value. Visual inspection of the final model showed the success of matching in all overlapping areas. The final model contains ca. 11.5 million triangles (Figure 15).
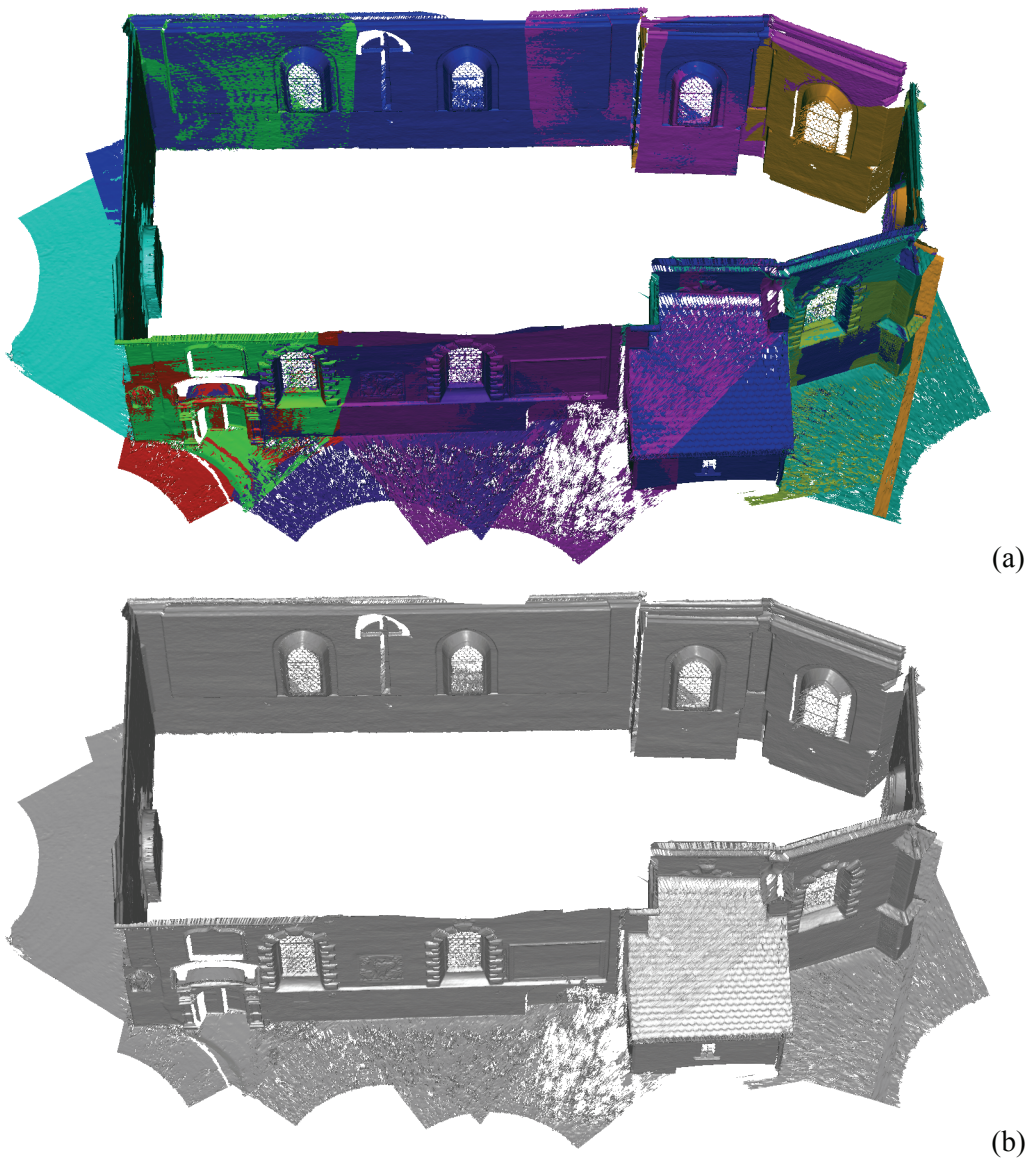

(a)

(b)

Figure 15. The final result of "chapel" experiment. (a) 14 pointclouds are in different color, (b) shaded view of the final composite surface.

Table 9. Numerical results of "chapel" experiment.

#	No. of template points	No. of search points	No. of iterations	No. of subpatches	Time (second)	$\hat{\sigma}_0$ (mm)
1	106 577	458 015	8	9	13.3	3.5
2	12 090	219 732	8	5	3.8	3.3
3	33 929	779 130	7	6	16.5	2.8
4	113 374	144 610	8	7	14.2	2.8
5	189 969	342 388	7	5	22.5	2.8
6	29 432	441 624	7	9	4.6	3.9
7	52 816	243 666	11	7	9.4	3.6
8	117 929	493 070	7	5	27.1	3.3
9	69 756	353 357	8	3	10.6	3.1
10	106 656	271 633	6	4	15.1	2.8
11	40 007	239 615	12	4	5.8	3.7
12	48 384	389 649	8	6	5.9	3.0
13	49 427	471 845	14	4	10.8	3.9
14	7 394	963 379	10	4	4.2	3.8

6.3.2. Weary Herakles – cultural heritage

6.3.2.1. The Story

A part of a Herakles statue, named "Weary Herakles" and located in the Antalya Museum (Turkey), was scanned by a coded structured light system. This is a marble statue of the Greek demigod Herakles, which dates back to the 2nd century AD (Figure 16a). It is a copy of an original bronze statue of Herakles sculptured about 330-320 BC by the Greek master Lysippos of Sikyon. Many artisans devoted their skills to replicating this original around that period. This particular example was probably carved in the Hadrianic or Antonine (Roman) period. The version is identified as the "Herakles Farnese" type on the basis of its similarity to a more complete copy (Figure 16c) in the Museo Archeologico Nazionale Napoli (Naples National Archaeological Museum, Italy).
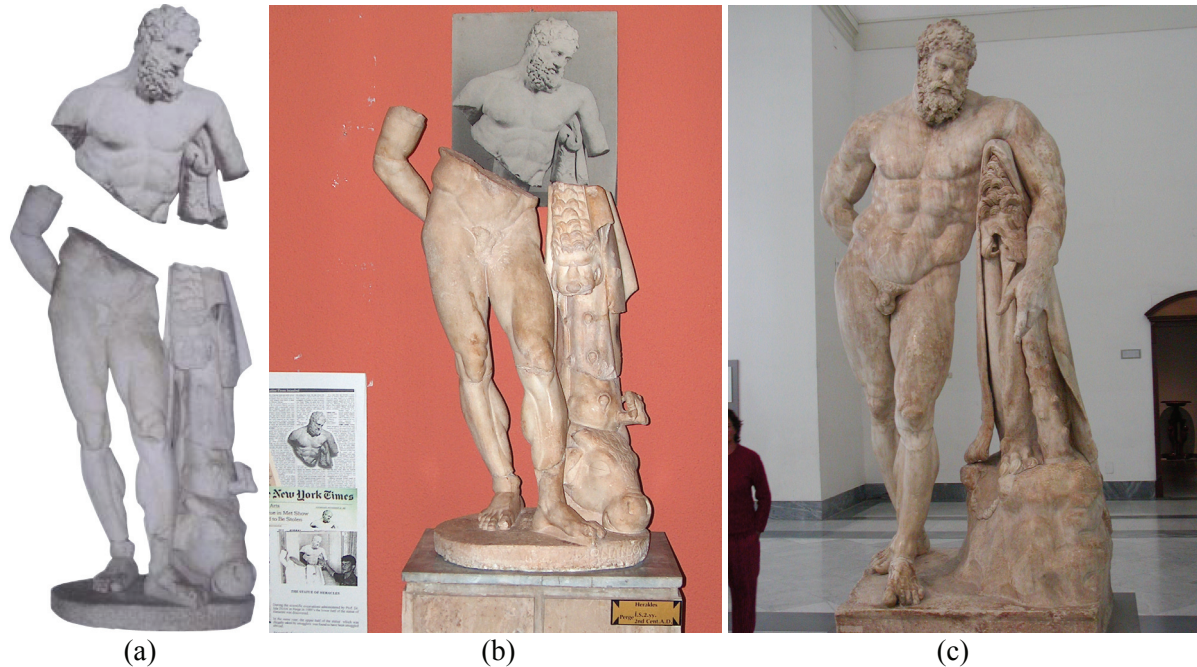

(a)   (b)   (c)

Figure 16. (a) Weary Herakles statue split into upper and lower parts, (b) The lower part in the Antalya Museum, (c) "Herakles Farnese" type located in Naples. Pictures (a) and (c) are courtesy of Ozgen Acar and René Seindal, respectively.

The statue was broken in two parts (Figure 16a). We do not know when and by whom it was done. The upper half was first seen in the USA in the early 1980s. It is currently to be found at the Boston Museum of Fine Arts. The lower part was found by Prof. Jale Inan (Inan, 1981, 1992) at an excavation site in Perge (Antalya, Turkey) in 1980. It is now on display in the Antalya Museum, along with a photograph of the top half (Figure 16b).

According to the Turkish law, Turkish antiques have been state property since Ottoman times 1906. The Turkish government has asked for the hand-over of the upper half so that the two fragments can be joined. The Boston Museum has refused to consider the Turkish petition. In 1992, casts of the two fragments were placed together. They were found to match perfectly. The Boston Museum says the statue may have been broken in ancient times, and the upper torso may have been taken from Turkey before the Turkish law established state ownership of archaeological finds (Rose and Acar, 1995; Brodie et al., 2000; Brodie, 2003; Gizzarelli, 2006).

Since both parts are unfortunately separated geographically, our aim was to record and model both the lower and the upper part and bring these partial models together in the computer, so that at least there the complete statue could be seen, appreciated and analyzed. With the help of the Turkish authorities and the Antalya Museum we were able to complete our work on the lower part, but access to the Boston Museum was denied.

The digitization of the lower part of the statue was done on 19-20 September 2005 in the Antalya Museum with a Breuckmann (http://www.breuckmann.com) optoTOP-HE coded structured light system. The system was kindly provided by the Turkish reseller InfoTRON Co. (http://www.infotron.com.tr), Istanbul.

The project was conducted in cooperation with InfoTRON Co. (Turkey), Breuckmann GmbH (Germany), the Division of Photogrammetry of Yildiz Technical University (Turkey), and the Group of Photogrammetry and Remote Sensing of ETH Zurich (Switzerland). Further information can be found on the project webpage: http://www.photogrammetry.ethz.ch/research/herakles/

6.3.2.2. Data acquisition in the Antalya Museum

The scanning campaign was completed in one and a half days of work. The statue is around 1.1 meters in height. The whole object was covered with 56 scans on the first day work. The remaining 11 scans of the second day were for filling the data holes and occlusion areas. Totally 83.75M points were acquired in 67 scan files. The average point spacing is 0.5 millimeter.

6.3.2.3. Pointcloud registration

Totally 234 consecutive matching processes were performed using the LS3D matching method. In all cases the solution was found. No divergence or failure case occurred. The average of the sigma naught values is 81 micron.

The first scan was selected as the reference, which defines the datum of the common coordinate system. Since multiple overlaps exist among the pointclouds, there is need for a global registration.

In the LS3D matching processes, the final correspondences were saved to separate files. The number of tie points was thinned out by selecting every 24th correspondence. Then all these files were given as input to the block adjustment by independent models software BAM7. It was run in the rigid body transformation mode by fixing the scale factor to unity. The block adjustment concluded with 47 micron a posteriori sigma naught value in 4 iterations. This value is in good agreement with the optoTOP-HE system specifications, whose feature accuracy is given as 45 microns.

6.3.2.4. Surface modeling and texture mapping

After the registration, all scan files were merged into one XYZ file, discarding the scanner detected blunders and background wall or other non relevant parts. This file totally contains 33.9 M points. The editing procedures were carried out in Geomagic Studio 6 (Raindrop Geomagic).

As a first attempt the surface mesh generation was tried at the original data resolution. The operation could not be performed, since the memory request of the software exceeded the physical memory limit of 2 GB of the computer. Therefore, the number of points was down-sampled to 9.0 million. Afterwards, surface triangulation was performed. Because of the complexity of the statue and

occlusions, some inner concave parts could not be seen by the scanner. This resulted in several data holes on the triangulated surface. They were interactively filled. The final model contains 5.2 M triangles. We have achieved a high level of realism, which can make a one-to-one scale production of the statue possible, if required (Figure 17).

Separately taken pictures, with a 4M pixel CCD Leica Digilux 1 camera, were used for the texture mapping (Figure 17a). For the details of the project, the author refers to Akca et al. (2006).
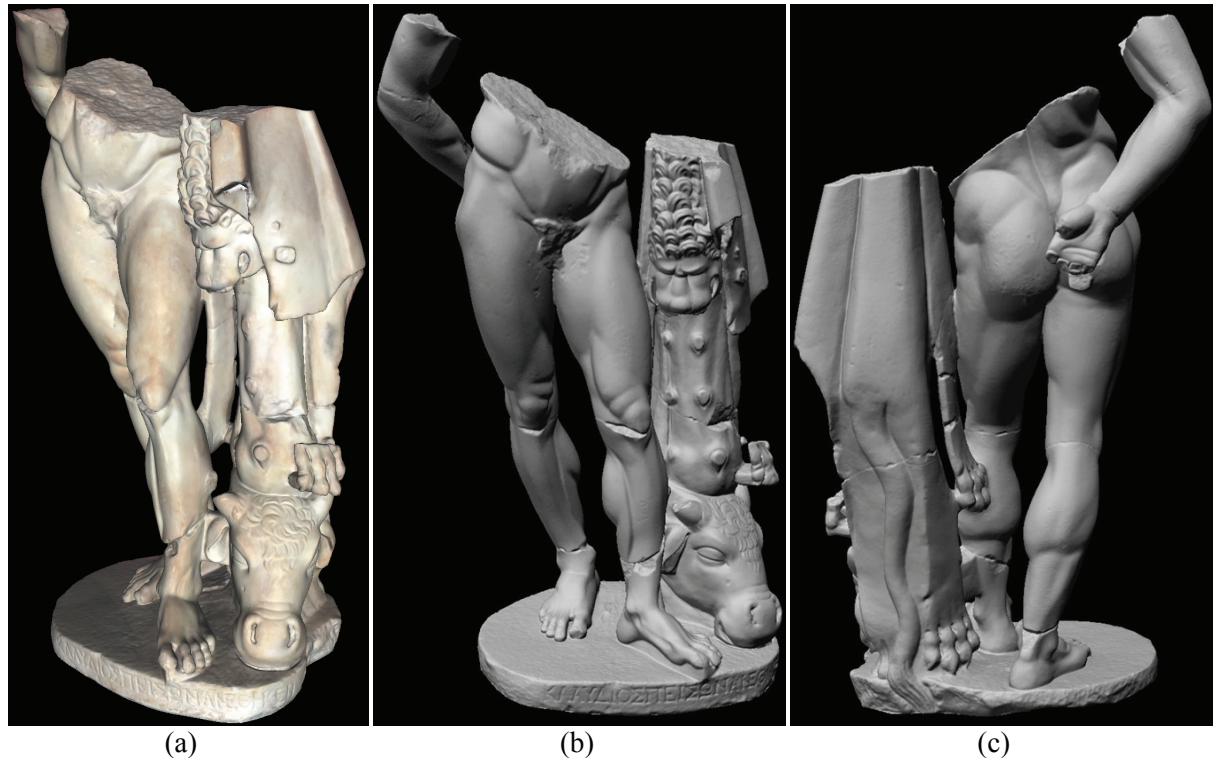

| (a) | (b) | (c) |

Figure 17. (a) Frontal view of the texture mapped model, (b) frontal view and (c) back view of the grey shaded model.

6.3.3. Khmer head – cultural heritage

The earliest examples of Buddhist art on the mainland of Southeast Asia date from the 4th and 5th centuries and emerged under the influence of Indian and Sri Lankan art. During the 6th century the Khmer people established themselves in the fertile tropical plains of Cambodia, and as the dominating power in Southeast Asia in the 12th and 13th centuries. They built the stunning group of temples at Angkor. The Khmer rulers supported both Hinduism, displayed most magnificently at Angkor Vat, and Buddhism, whose most important monument the Bayon (the central temple at Angkor Thom) can still be admired.

A bodhisattva head from the late 12th or early 13th century is carved in the Bayon style (Figure 18a). It is Lokeshvara or Avalokiteshvara, the "Lord of compassion who looks down (on the suffering of the world)," an emanation of the Buddha Amitabha as demonstrated by the seated Buddha on his hair ornament. His serene expression and transcendent smile convey better than any words the sublime essence of the Buddhist teachings (Museum Rietberg, 2006).

This study is about the 3D modeling of this Khmer head sculpture digitized using a Breuckmann optoTOP-SE sensor. More information can be found on the project web page: http://www.photogrammetry.ethz.ch/research/khmer/

6.3.3.1. Data acquisition in Museum Rietberg
The head is made of sandstone and 28 centimeters in height. The data acquisition was done in Museum Rietberg on 4 May 2006. A Breuckmann OptoTOP-SE fringe projection system was used for

this purpose (Figure 18b). The scanning and imaging took four hours on site work. The head was covered with 18 point clouds, totally 23.6 million points.
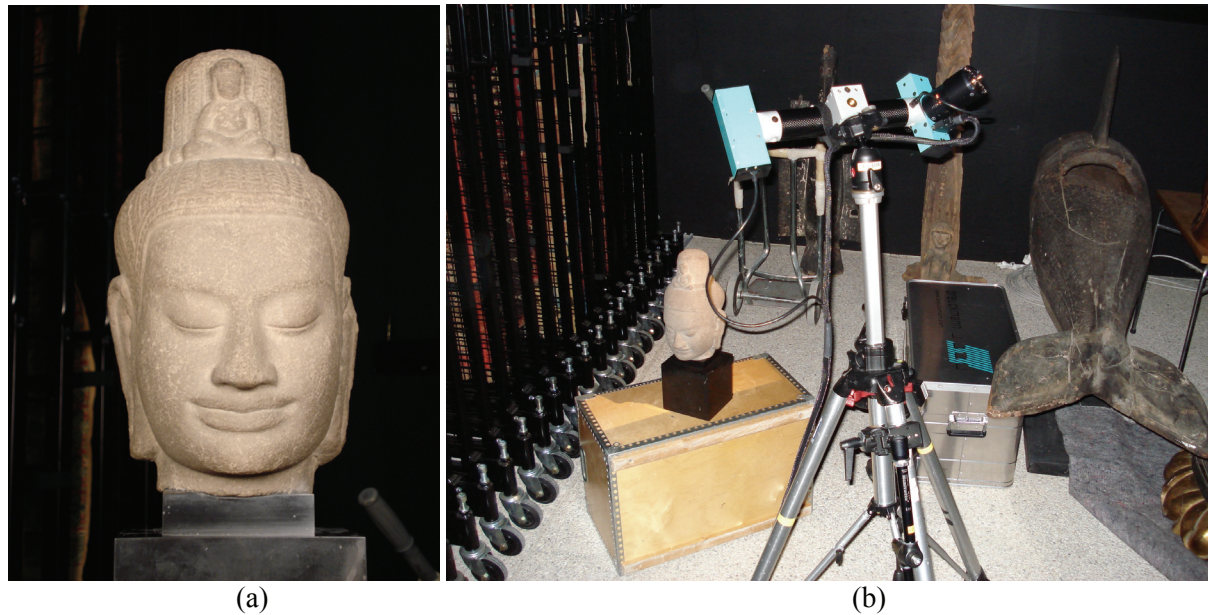

<table>
<tr><td>(a)</td><td>(b)</td></tr>
</table>

Figure 18. (a) The Khmer Head in the Museum Rietberg Zurich, (b) scanning in the Museum Rietberg.

6.3.3.2. Pointcloud registration

The point cloud registration was done again with the LS3D surface matching method. 52 pairwise LS3D matchings for all overlaps gave an average sigma naught value of 60 microns. The global registration with the block adjustment by independent models solution concluded with a 28 microns sigma naught value.

6.3.3.3. Surface modeling

The surface modeling was done by use of two commercial packages, namely Geomagic Studio and Polyworks. The aim was to compare the capabilities of both software. Registered point clouds were imported in the proper formats. Accordingly, the registration steps were skipped in both software. Both software packages have different processing pipelines.

Geomagic Studio offers fully automatic data import functionality provided that data is given in one of the appropriate point cloud formats. Totally 18 point clouds were imported, merged into one, which gave a very dense (denser than 50 microns interpoint distance at some locations) point cloud. After discarding the no data or scanner signed erroneous points and points belonging to background and other non relevant objects, 3.2 million points remained.

The noise reduction ensures that points coming from different views in different quality will finally have the similar signal-to-noise ratio. Here a slight (low level) noise reduction was applied. After this step, the model contains highly redundant points coming from the multiple views. The "Curvature Sampling" function with a 60% reduction rate reduced the number of points to 1.9 millions. Intentionally, a restricted reduction rate was selected, so that small details can be preserved.

The surface triangulation in Geomagic Studio is fully 3D and automatic, with limited user interaction. Hence, the resulting mesh will have topological errors and holes. On the other hand, it can preserve the high frequency details of the object geometry successfully by considering all points in one processing sweep. In general, surface triangulation quality is highly related to the point density and homogeneity.

PolyWorks has a significantly different workflow. Each step is represented as a module inside the package. Data import is not automatically performed. Each point cloud is individually imported, subsequently converted to the surface form by applying a 2.5D triangulation, similar to the terrain modeling case. Therefore, the user should interactively rotate the point cloud to a position where the viewing angle is close to the one at the acquisition instant. It substantially reduces the topological

errors. On the opposite side, such a stepwise surface generation strategy does not utilize all the available information properly. For example, there might be some object parts with thin point distributions in individual views, whereas the combination of all views together provides a good solution.
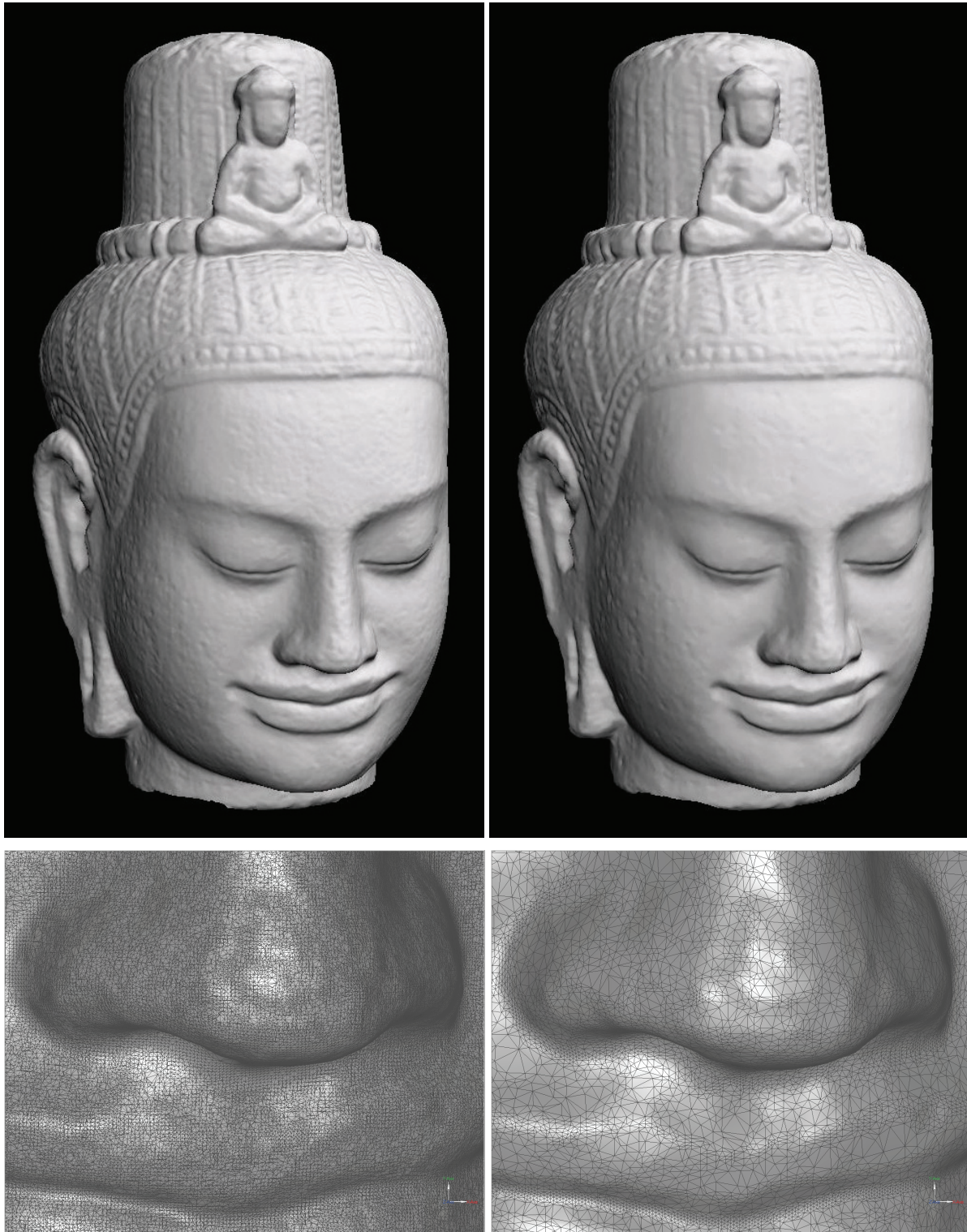

Figure 19. Shaded view of the model from Geomagic Studio (top-left) and PolyWorks (top-right). Zoom into the nose of Geomagic Studio (bottom-left) and PolyWorks (bottom-right) mesh models.

At the next step, separate surfaces were merged as one manifold using the IMMerge module. This part is highly automated, and additionally offers a noise reduction option. During the process, triangulation is also optimized especially at the overlapping regions by associating dense triangles to high curvature areas and sparse at flat areas.

The IMEdit module offers many surface editing functions, e.g. cropping the AOI, filling the data holes, correcting the wrong triangles, boundary cleaning, etc. However, it is less flexible and user friendly than Geomagic Studio.

The resulting models from both software packages meet the project requirements. PolyWorks model (0.6 million triangles) has substantially less number of triangles than Geomagic model (3.9 million triangles), thus having a better and optimized triangulation algorithm. However, the model from Geomagic Studio preserves the small details and structures slightly better than the model of PolyWorks (Figure 19). More details can be found in Akca et al. (2007).

6.3.3.4. Texture mapping

A photographer type of professional illumination system consisting of two diffuse lights on a tripod was used (Figure 20). It reduces the radiometric differences between the images and shadow effects at the complex parts and object silhouettes. Images were taken by a Sony DSC-W30 6 megapixel digital camera. The PolyWorks model was used for the texture mapping in the original resolution.

Figure 20. The illumination system used for the texture mapping.

Internal and external orientations of the images were computed using a photogrammetric bundle adjustment with self-calibration. The object space coordinate system was defined as the coordinate system of the 3D model. The common points were interactively identified both in digital images and in the intensity images of the scanner.

Afterwards we used this information, in addition to the geometric model and the images, to conduct a visibility analysis for every camera position. Partly occluded triangles are subdivided and re-meshed

into fully visible or fully occluded triangles. The resultant list of visible triangles is used to calculate the texture coordinates for every vertex of the mesh. The underlying algorithm uses a "best view" algorithm to evaluate the optimal texture for every triangle. The mesh consists of approximately 295 000 vertices and 585 000 facets (Figure 21).

Figure 21. Picture of the Khmer head (left), and its texture mapped 3D model (right).

6.3.4. Pinchango Alto – terrain modeling

Pinchango Alto is the largest Late Intermediate Period (LIP, AD 1000–1400) site in the Palpa area. The site is located about 3 km north of the modern town of Palpa (Peru) on an elongated rocky spur on the western slope of Cerro Pinchango.

The site was documented under the framework of a research program called NTG ("New methods and technologies in the humanities") funded by the German Ministry of Education and Research (BMBF, Bonn). The project aims to investigate the applicability of the modern surveying techniques to archaeological documentation studies. Two systems, a terrestrial laser scanner and a UAV (Unmanned Aerial Vehicle) system, were employed during the September 2004 field campaign. The field work was conducted in cooperation with Riegl Laser Measurement Systems (Austria), Helicam (Switzerland), the German Institute of Archaeology, Commission for General and Comparative Archaeology (KAVA) in Bonn (Germany) and the Group of Photogrammetry and Remote Sensing of ETH Zurich (Switzerland). Further information can be found on the project webpage: http://www.photogrammetry.ethz.ch/research/pinchango.

6.3.4.1. The scanning campaign
A Riegl LMS-Z420i terrestrial laserscanner was used for data acquisition. The scanning campaign had been completed in 5 days of fieldwork. The site is around 300x150 meters in size. The whole area was covered with 61 scans, only 57 of which were registered. The remaining 4 scans were not used, since they cover the southern cliff part of the site which is not directly of interest, and due to insufficient overlapping with scans of the main area.

The area of the well preserved walls (Area1 in Figure 22a) was scanned in the first 3 days. In the continuing 4th and 5th days the Area2 was scanned with a lower point density level. Totally 144 million of points acquired in 57 scan files. Figure 22b shows the day by day coverage of the site. The point spacing is between 1-35 cm, changing with the range.
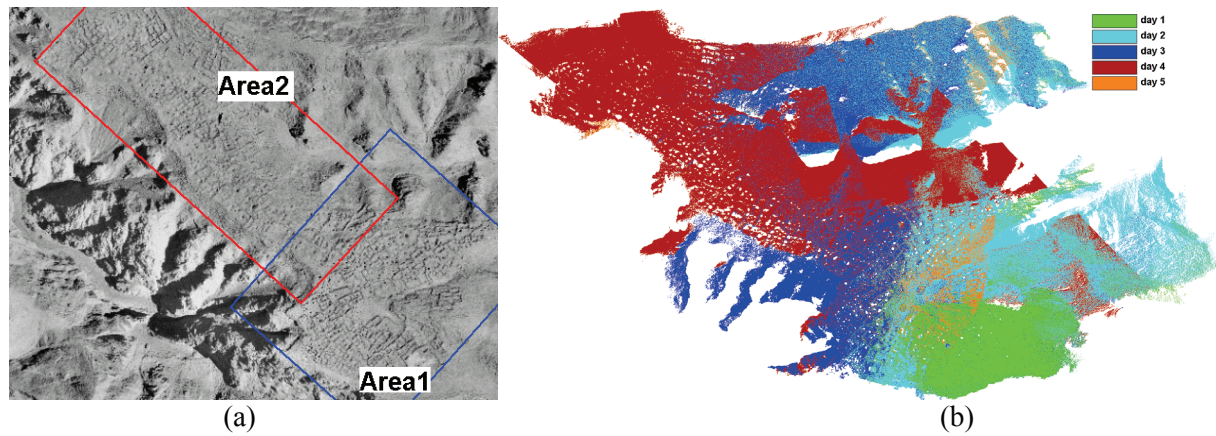

(a)　　　　　　　　　　　　　　　　　　　　(b)

Figure 22. (a) Area1 and Area2, (b) day by day coverage of the site.

6.3.4.2. Pairwise registration with the LS3D surface matcher

Totally 130 consecutive matching processes were performed using the LS3D matching method. The matching 01-19 were done on an Intel® P4 2.53 GHz PC, and the rest 20-130 were done on an Intel® P4 3.40 GHz PC. All the LS3D matching processes were performed in the mono-patch mode. The multi-subpatch mode was not chosen, since interactively selecting of the subpatches is difficult due to low texture property of the site.

Due to the topography of the site and relatively large incident angles of the signal paths, large occlusions occurred in the pointclouds (Figure 23a and 23b). This is a difficult case for the surface registration problem. However our surface matching algorithm LS3D successfully handled this problem.
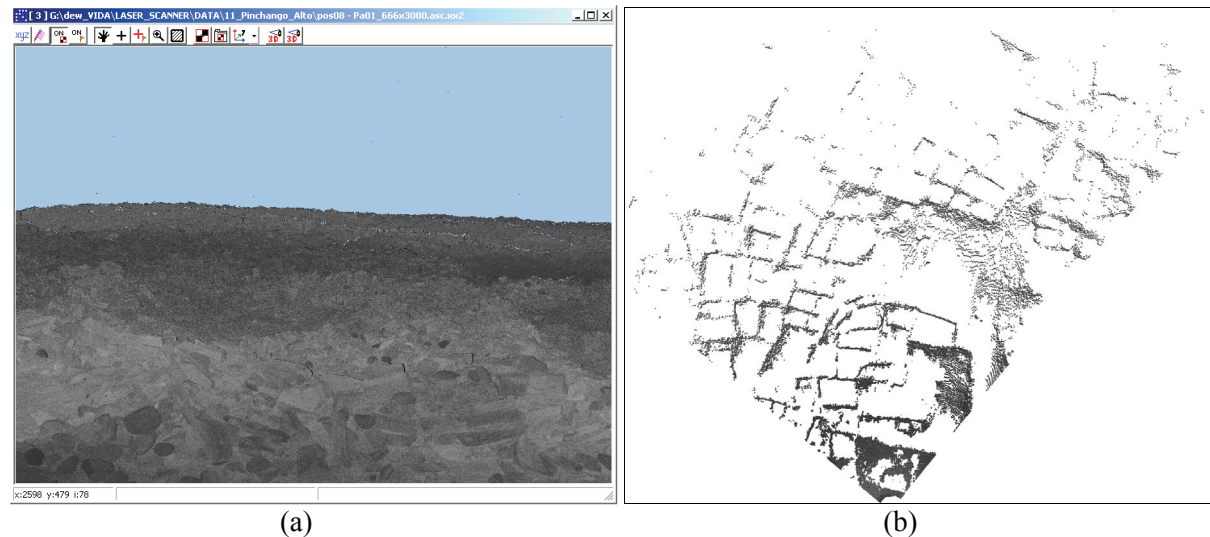

(a)　　　　　　　　　　　　　　　　　　　　(b)

Figure 23. (a) Intensity image of a nearly 90^0 subpart of scan #8, (b) top view of the pointcloud of (a) in 3D.

The numerical results of the LS3D matching processes are given in Table 10. In all cases it successfully found the solution. The average sigma naught value is around 1.0 cm, which confirms the reported accuracy potential of the LMS-Z420i scanner.

Table 10. Numerical results of the LS3D matchings in "Pinchango Alto" experiment.

#	TM scan	SR scan	NoTM (K)	NoSR (K)	NoCO (K)	Iter	Time (sec.)	SIG (cm)	#	TM scan	SR scan	NoTM (K)	NoSR (K)	NoCO (K)	Iter	Time (sec.)	SIG (cm)
1	01	02	2063	1132	502	9	98	1.9	66	36	37	825	923	106	7	37	1.1
2	02	03	1132	1101	731	8	77	1.0	67	37	38	923	829	219	12	49	1.2
3	03	04	1101	1099	531	6	55	0.9	68	38	39	829	875	166	11	50	1.0
4	04	05	1099	1072	631	7	111	0.7	69	39	40	875	874	69	8	24	1.3
5	05	06	1072	1068	841	6	264	0.8	70	40	41	874	860	204	10	53	1.0
6	06	07	1068	1060	789	8	139	1.0	71	41	42	860	886	283	9	86	0.9
7	07	08	1060	1059	738	8	152	1.6	72	42	43	886	788	363	8	78	1.2
8	08	09	1037	1096	556	8	90	2.8	73	43	44	788	737	163	12	42	1.1
9	09	10	1096	1023	292	8	40	2.5	74	44	45	737	826	54	12	22	1.0
10	10	11	1023	1006	613	9	113	1.5	75	45	46	826	851	108	10	34	0.9
11	11	12	1006	980	693	8	260	2.0	76	46	47	851	830	348	8	91	0.8
12	01	03	1926	1085	337	10	58	1.5	77	16	30	819	766	360	8	169	0.8
13	01	05	1926	1045	104	8	37	1.2	78	16	31	819	892	248	6	74	1.2
14	01	07	1926	1037	232	9	47	1.7	79	30	31	766	892	95	6	36	1.2
15	01	09	1926	1096	367	8	119	1.4	80	18	32	937	907	260	8	86	1.0
16	03	09	1085	1096	99	7	25	1.0	81	18	31	937	892	97	10	44	1.1
17	04	07	1077	1037	383	5	61	0.7	82	19	33	967	931	296	6	84	0.6
18	04	06	1077	1043	413	6	59	0.7	83	19	32	967	907	148	6	58	0.6
19	07	12	1037	980	455	11	69	1.6	84	20	33	986	931	221	6	41	1.0
20	12	13	980	939	298	8	85	1.1	85	20	34	986	923	237	7	43	1.0
21	13	14	939	810	359	11	97	1.2	86	21	34	970	923	338	5	54	1.0
22	14	15	810	792	309	11	129	0.9	87	21	35	970	871	135	9	41	0.9
23	15	16	792	819	357	9	186	0.9	88	22	35	924	871	180	6	33	1.0
24	16	17	819	939	220	9	108	1.1	89	22	36	924	825	153	6	29	1.1
25	17	18	939	937	364	8	73	1.3	90	23	36	819	825	79	5	21	1.1
26	18	19	937	967	285	10	66	1.2	91	35	38	871	829	81	7	30	1.1
27	19	20	967	986	303	8	65	0.7	92	34	39	923	875	172	6	53	0.9
28	20	21	986	970	421	10	70	1.1	93	35	39	871	875	90	7	33	1.0
29	21	22	970	924	243	10	59	1.2	94	33	39	931	875	69	10	35	1.1
30	22	23	924	819	270	10	49	1.3	95	32	42	907	886	140	11	81	0.9
31	23	24	819	840	316	5	46	1.3	96	31	42	892	886	107	10	50	1.0
32	24	25	840	926	166	8	44	1.1	97	31	43	892	788	64	15	39	1.0
33	25	26	926	1028	291	10	72	1.2	98	41	43	860	788	148	9	47	0.8
34	26	27	1028	1073	313	11	76	1.1	99	41	44	860	737	184	8	48	0.8
35	27	28	1073	899	521	6	75	1.0	100	40	45	874	826	314	7	133	0.6
36	28	29	899	832	253	7	64	1.3	101	40	46	874	851	78	8	32	0.8
37	07	11	1037	1006	139	10	45	0.9	102	39	46	875	851	231	9	170	0.6
38	09	11	1096	1006	160	7	26	1.3	103	38	46	829	851	86	8	54	0.6
39	08	11	1037	1006	180	10	52	1.6	104	38	47	829	830	174	6	60	0.7
40	07	13	1037	939	150	9	31	1.1	105	41	45	860	826	71	8	29	0.8
41	06	13	1043	939	155	8	37	0.8	106	37	50	923	2349	26	8	14	1.1
42	05	13	1045	939	176	8	39	0.8	107	50	49	2349	3142	332	5	64	0.9
43	14	16	810	819	218	10	58	1.0	108	49	48	3142	2221	238	7	58	0.9
44	13	16	939	819	285	10	55	1.1	109	50	51	2349	3167	74	6	25	0.9
45	13	17	939	939	328	8	87	1.0	110	49	51	3142	3167	45	5	21	0.9
46	12	17	980	939	270	8	68	1.3	111	48	52	2221	2676	91	15	38	0.6
47	11	18	1006	937	381	10	77	1.2	112	52	53	2676	3178	563	10	290	0.8
48	10	19	1023	967	278	6	48	0.8	113	53	54	3178	2457	169	18	98	0.8
49	10	20	1023	986	135	6	21	1.0	114	54	55	2457	3147	41	10	29	1.0
50	01	20	1926	986	67	7	24	1.0	115	01	57	1926	3250	499	7	**574**	0.5
51	01	26	1926	1028	98	8	46	1.0	116	57	56	3250	2703	926	3	**1353**	0.3
52	01	27	1926	1073	102	7	36	1.0	117	37	51	923	3167	382	4	45	1.2
53	22	25	924	926	170	6	36	1.1	118	36	51	825	3167	196	5	35	1.2
54	24	29	840	832	111	5	19	1.2	119	23	51	819	3167	200	6	37	1.2
55	24	28	840	899	146	4	31	1.0	120	38	51	829	3167	147	5	30	1.2
56	25	28	926	899	205	6	35	1.3	121	47	50	830	2349	157	5	28	1.2
57	26	28	1028	899	176	9	31	1.3	122	37	49	923	3142	91	5	29	1.3
58	21	26	970	1028	53	9	22	1.0	123	20	56	986	2703	262	12	48	0.8
59	15	30	792	766	420	11	190	0.9	124	10	56	1023	2703	227	11	55	0.6
60	17	31	939	892	292	10	81	1.1	125	09	56	1096	2703	547	10	81	0.6
61	31	32	892	907	192	10	49	1.2	126	21	56	970	2703	166	13	45	0.7
62	32	33	907	931	188	9	38	1.3	127	21	57	970	3250	236	13	60	0.7
63	33	34	931	923	134	9	38	1.1	128	20	57	986	3250	238	11	47	0.7
64	34	35	923	871	347	6	72	1.1	129	19	57	967	3250	79	10	35	0.5
65	35	36	871	825	172	9	39	1.3	130	01	56	1926	2703	631	3	**432**	0.6

TM: Template surface, SR: search surface, NoTM: No. of TM points, NoSR: No. of SR points, NoCO: No. of corresponding points,
SIG: Sigma naught a posteriori.

The Pinchango Alto laser data set is a good example of large volume data sets with 144 million points from 57 stand points. Only the raw XYZ files in ASCII format occupy 3.83 GB memory area on a hard disk. Owing to our efficient boxing structure, the large data is effectively managed and processed.

As shown in Table 10, our proposed method provided successful matching results in reasonable processing times. Only during the matching of any pair of those three overview scans 01, 56 and 57 the computation times were relatively long, especially for the matching number #116 (matching of scan 56 to scan 57 in Table 10). One reason is the extremely high number of points, i.e. matching of 2.7 million points to 3.2 million points requires heavy computation for the correspondence searching. Secondly scan 56, which the boxing structure was established for in matching #116, covers a large area of 230x350 meters in dimension. This requires a large number of cuboid elements in the boxing structure. But it was only possible to establish the boxing structure with 1200x1200x1200 elements due to the physical memory limit of the PC.
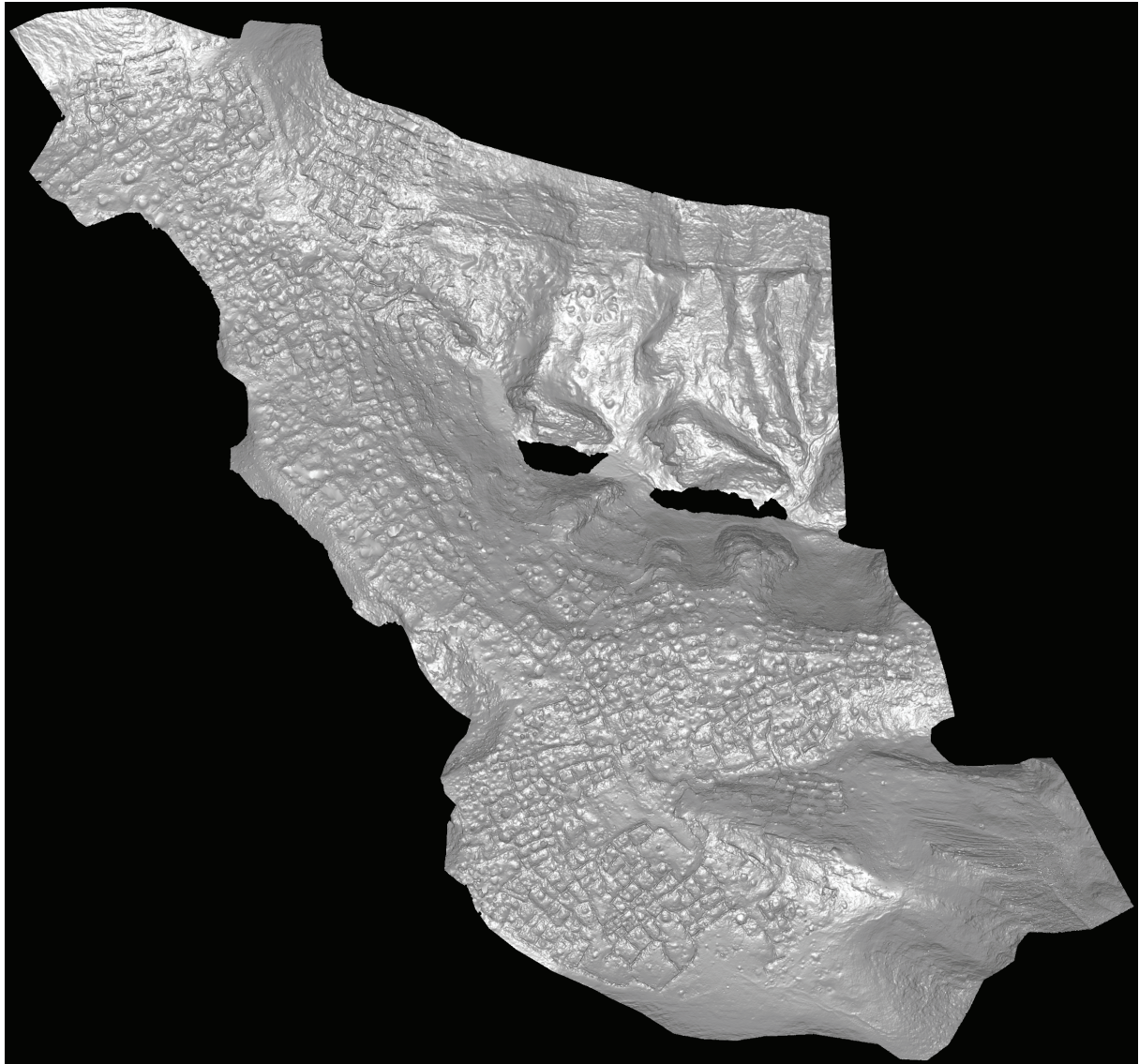
Figure 24. Shaded view of the generated model using Geomagic Studio 6.

6.3.4.3. Global registration
In the LS3D matching processes, the final correspondences were saved to separate files. The number of tie points was thinned out by selecting of every 10th correspondence. Then all these files were given as input to the block adjustment by independent models software BAM7. It was run in the rigid body transformation mode by fixing the scale factor to unity. The block adjustment concluded with 0.5

cm a posteriori sigma value in 4 iterations. Decomposition of the sigma value into the main coordinate axes gives 0.3 cm, 0.3 cm, and 0.4 cm along x-y-z axes respectively. Those relatively homogeneous and small values show the success of the final agreement of all the pointclouds.

6.3.4.4. Surface modeling

After the registration, all scan files were merged into one XYZ file, discarding the no data or the scanner signed erroneous points, e.g. scan points on the sky. This file totally contains 78.1 million points. It was further cropped to contain only the area of interest, finally with 69.2 million points. Geomagic Studio 6 was used for the surface modeling.

The number of points was down-sampled to 14.8 million points, which gives a point spacing around 5 cm. Then the pointcloud file was split to two files to overcome of memory limitation. This was done manually, since the software does not provide any automatic solution. Finally, surface triangulation was done for both parts separately.

All the displaced objects during the 5 days fieldwork, e.g. people, GPS, bags, boxes, etc., produced errors in the generated mesh. Those errors were edited manually. Because of data unavailability, some holes occurred on the meshed surface. Missing data parts are usually due to occlusions of walls and the hollows. They were interactively filled. After the editing step, those two meshed surface parts were merged as one manifold. The final model contains 5.8 million triangles (Figure 24).

6.3.5. SRTM TerrainScape™ - Filling the holes of SRTM C-Band DEMs

Swissphoto AG (Zurich, Switzerland), in cooperation with Jeppesen (Englewood, Denver, USA), generates a worldwide terrain database that will meet aviation quality requirements for autonomous landing and take-off (Norris, 2005). The base DSM is the Shuttle Radar Topography Mission (SRTM) C-SAR DEM, which covers the Earth's surface between latitudes 60^0N and 57^0S at a resolution of 3 arc second for the full coverage and 1 arc second for the USA and its territories. The Shuttle Radar Topography Mission was jointly performed by the National Aeronautics and Space Administration (NASA), the National Geospatial-Intelligence Agency (NGA), the German Aerospace Center (DLR) and the Italian Space Agency (ASI) in February 2000, to generate a near-global DEM of the Earth using radar interferometry operating in C- and X- bands.

The SRTM C-DEM products have some data holes due to typical problems of radar interferometry (InSAR), e.g. shadows, layover and poor reflectivity properties of the Earth's surface. The project aims to fill these data holes by use of the local DEMs wherever they are available in any resolution and characteristic (Figure 25). Because of the difference in production technique and standards, the local DEMs may have translational shift or/and angular rotation with respect to the SRTM DEMs. In the processing chain, the LS3D software is responsible for correcting these geometric differences by applying the Least Squares 3D surface matching technique. Further information can be found on the project webpage: http://www.photogrammetry.ethz.ch/research/srtm/

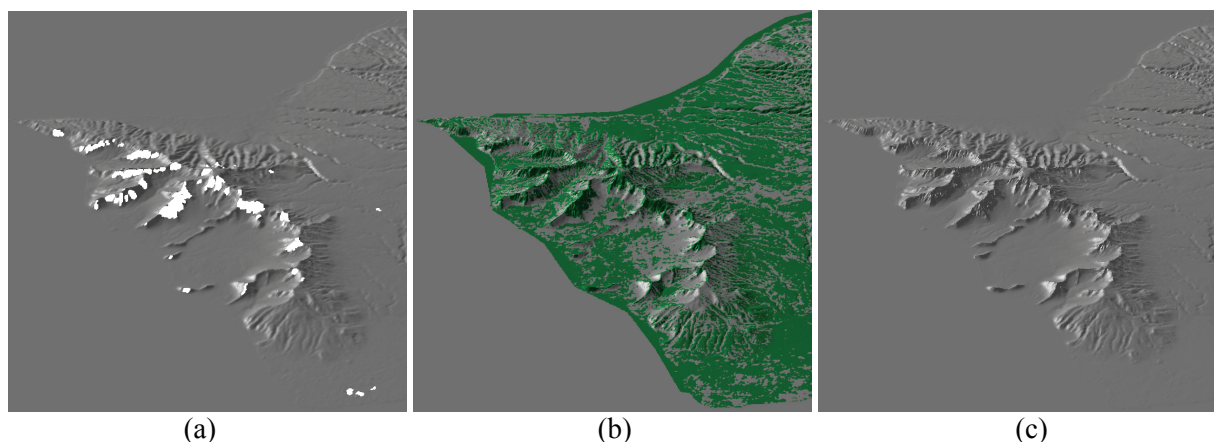| (a) | (b) | (c) |

Figure 25. (a) SRTM C-Band DEM with data holes, (b) registration of a local DEM onto the SRTM C-Band DEM by use of the LS3D matching, (c) filled data holes.

The LS3D software was embedded into the whole package, called SRTM TerrainScape™. The experiments have showed that the LS3D certainly has the capability for the co-registering of multi-resolution and multi-quality data sets. Figure 25 shows the registration of a local DEM with 30 meters resolution to a SRTM C-Band DEM whose resolution is around 90 meters.

6.3.6. Accuracy evaluation of DSMs derived from DMC digital airborne camera

The Cartographic Institute of Catalonia (ICC) has acquired a DMC digital camera (Intergraph) and has performed some first investigations regarding radiometric performance and geometric accuracy potential. In this cooperation with the Institute of Geodesy and Photogrammetry (IGP), ETH Zurich various aspects are analyzed. The investigations make use of recent test flights near Tortosa (Spain), a plane region with varying landcover. For the quantitative analysis of the DMC results, ground control points and LIDAR data exist, which have been simultaneously acquired with the DMC images.

The aerial triangulation was carried out with two different software packages, PAT-B and ACX. Accordingly, two DSMs of the test site were generated. The DSMs were compared with respect to the LIDAR DSM by use of the LS3D surface matching method. For the details, the author refers to Zhang et al. (2006).

6.3.6.1. Image and LIDAR data
The image data consists of 28 DMC images with a ground sampling distance (GSD) of 22 cm arranged in 4 parallel flight strips in E/W direction of 7 images each. They cover an area of about 5km x 5km size located close to the Ebro delta south-west of Barcelona with variable land cover. The images are taken from a large test dataset collected in December 2005 with the goal to check and verify the performance of a second DMC, which the ICC is planning to purchase in 2006. DMC images were acquired together with LIDAR data from 2.500m altitude (1:21,000 image scale). The forward and side overlap of the DMC images was 60% and 75%, respectively. This high side overlap and the presence of simultaneously collected LIDAR data were the major reasons to choose the data from this flight for the present study.

The LIDAR system used was an Optech 3030. There are some gaps in the data due to water surfaces and low reflectance objects (there are rice fields, possibly flooded, in the region). The LIDAR accuracy given by Optech is flying height divided by 2000 in planimetry and 30 cm in height at 2300m flying altitude (2300m is a company defined attitude for the accuracy specifications, not the project flying altitude). The practical experience of ICC is about 50% better, i.e. from 2300m about 50cm in planimetry and better than 15cm in height. The LIDAR data consisted of 4 strips (the 4th strip was flown twice due to clouds) and two cross strips at 45 and 90 deg, which are used for in-flight calibration, since the calibration data of the LIDAR system is not that stable.

6.3.6.2. Aerial triangulation and DSM generation
Automatically extracted tie points (generated by an in-house developed software called Tie Point Extraction Tool with pixel accuracy) and GCP observations were introduced into PAT-B without using GPS and IMU observations and without self-calibration. The sigma a posteriori was 7.3 microns (0.6 pixels). The mean standard deviations of the exterior orientation were (in m and grad): $X0 = 0.36$, $Y0 = 0.43$, $Z0 = 0.23$, $\omega = 0.013$, $\varphi = 0.014$, $\kappa = 0.007$.

In order to produce tie points of higher accuracy, the data was imported into the commercial aerial triangulation software Match-AT of Inpho, while the already existing tie points served as initial positions for tie point search areas. The program yielded 2771 new tie points. The estimated sigma naught was 1.6 micron (0.13 pixels).

The second bundle block adjustment procedure was carried out with the ACX/GeoTex software developed at the ICC. The mean standard deviations of the exterior orientation were (in m and sec): $X0 = 0.06$, $Y0 = 0.07$, $Z0 = 0.05$, $\omega = 0.16$, $\varphi = 0.12$, $\kappa = 0.09$. The results of ACX are expected to be more accurate than those of PAT-B, due to more and more accurate tie points and integration of GPS observations, which may improve the results.

The automated DSM generation was performed using the SAT-PP program developed at the IGP. Its matching algorithm is described in Zhang and Gruen (2004). In order to achieve successful and

reliable matching, the method matches a dense pattern of features with an appropriate matching strategy, making use of all available and explicit knowledge, concerning sensor model, network structure, image content and geometrical constraints such as the epipolar geometry constraint. The approach combines area-based matching (ABM) and feature-based matching (FBM), matching parameter self-tuning, generation of redundant matches and a coarse-to-fine hierarchical matching strategy. The approach essentially consists of 3 mutually connected components: the image preprocessing, the multiple primitive multi-image (MPM) matching and the refined matching procedure.
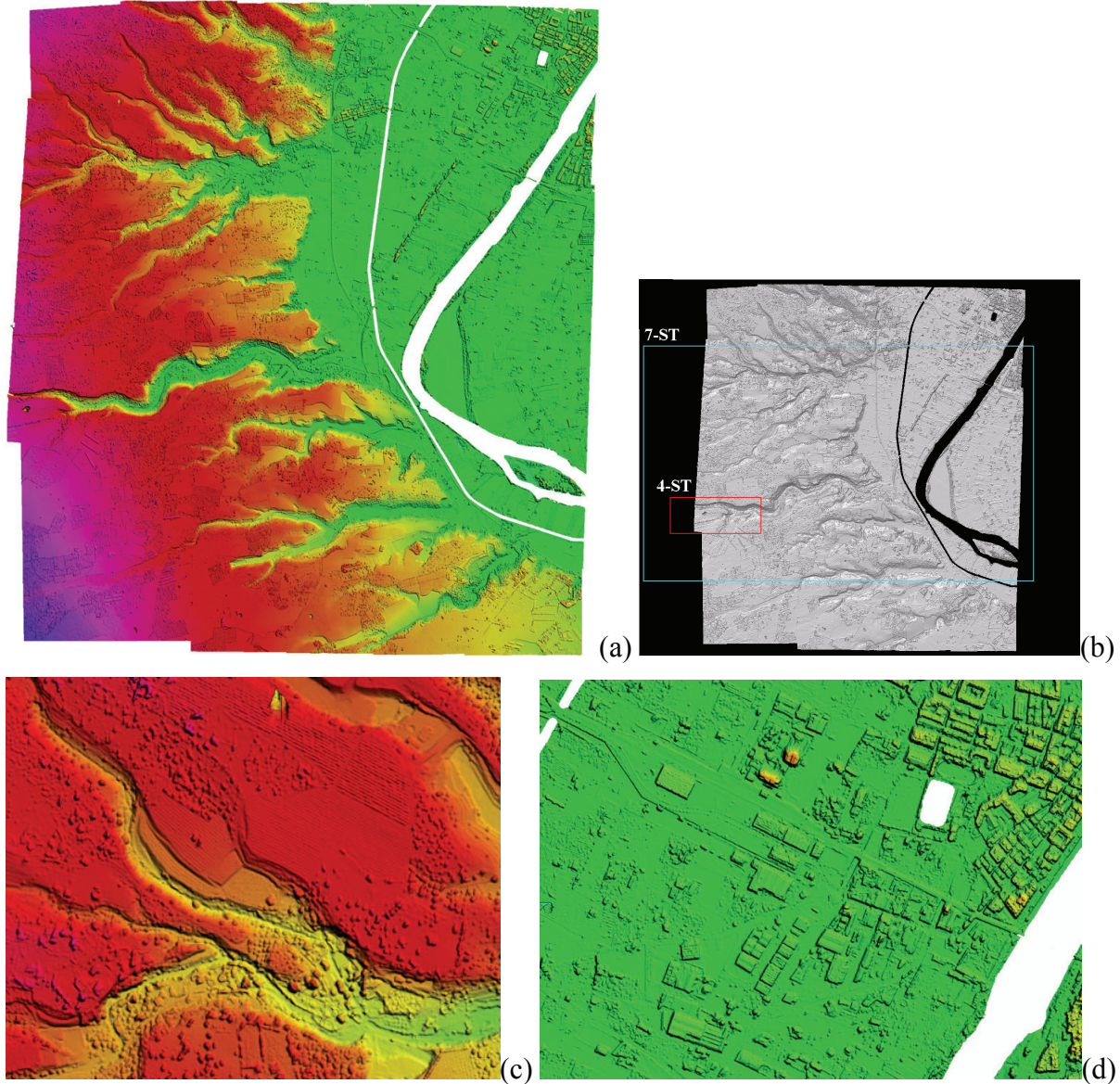
Figure 26. (a) The 1m grid matching DSM using ACX orientation. (b) DSM coverage, grey: matching DSM, blue: 7-strip LIDAR DSM, red: 4-strip LIDAR DSM. (c) and (d) are zoom-ins of (a).

6.3.6.3. DSM results and analysis

Two DSMs were produced by matching, using the orientation from PAT-B and ACX respectively, covering an area of 5.1 (E/W) by 5.7 (N/S) km. The 1m grid DSM using the ACX orientation is presented in Figure 26a. Figures 26c and 26d are zoom-ins showing that the DSM has high resolution in good quality. Building roofs are well modeled, as well as other terrain discontinuities. The same applies to trees, bushes and even fine structures in the fields. White shows water areas that have been masked out manually before matching. The density of the matching DSM is, in this case, better than the density of the laser data. With matching of digital images, a DSM with equal or higher density than

a laser DSM can be generated. The used matching method provides similar results to LIDAR, even regarding accuracy.

For comparison with laser, the first pulse of the unfiltered laser data was used. The average point density of the laser data was 1.2 points/m^2. However, in vegetation areas (and there are quite many in this test site) the laser beam often measures below the top surface, thus leading to differences with the matching DSM.

For quality evaluation of DSMs, often a reference DSM is interpolated in the DSM to be checked. This approach is suboptimal, since a) at surface discontinuities surface modeling errors may lead to large height differences although the measurements are correct, and b) if the reference frames of the two DSMs differ (e.g. shifts and tilts), then again large differences occur, especially at discontinuities although the heights may be correct. The first shortcoming can be overcome by the approach used in Poli et al. (2004), where the shortest 3D distance between each reference point and the produced DSM is used. To avoid also the second shortcoming we used the LS3D surface matching method and the respective semi-commercial program LS3D.

Figure 26b shows the coverage of the DSMs. Two DSMs were interpolated from the LIDAR data, a 2m regular grid DSM covering the whole area called 7-strip LIDAR DSM, and a 1m regular grid DSM covering a smaller area called 4-strip LIDAR DSM. If interpolated to 1m grid spacing, 7-strip LIDAR DSM had 22 million points (and 29 million points for each SAT-PP DSMs from PAT-B and ACX orientations) and could not be processed by the LS3D program due to memory limitation of the computer.

Table 11. The results of the LS3D program. The number of used points is less than the number of valid points, because the overlap was not 100% and some points were additionally excluded. This was performed using a simple robust estimation by binary re-weighting according to sigma a posteriori (Equation 3.31). In all experiments, correspondences whose Euclidean distance is greater than 10xSigma are excluded and regarded as either outliers or occlusions. The a priori sigma is computed after an initial iteration without applying a transformation.

Template surface	Search surface	No. of valid points in template surface	No. of used points in the LS3D matching	Iter.	Sigma a priori (m)	Sigma a posteriori (m)	Tx (m)	Ty (m)	Tz (m)
LID_7ST	DMC_PATB	5,252,411	4,250,745	3	0.96	0.80	-0.00	-0.64	-0.06
LID_7ST	DMC_ACX	5,252,411	4,248,776	3	0.95	0.79	+0.05	-0.62	-0.07
LID_4ST	DMC_PATB	844,734	605,319	3	1.09	0.90	-0.01	-0.37	-0.26
LID_4ST	DMC_ACX	844,734	604,945	3	1.07	0.90	+0.01	-0.39	-0.12

Table 12. Decomposition of values of Table 11 into X, Y and Z components.

| Template surface	Search surface	Sigma a posteriori (m)	Decomposition of sigma a posteriori into components	Std. deviation (m)	Mean (m)	Min (m)	Max (m)
LID_7ST	DMC_PATB	0.80	X	0.32	0.00	-8.04	7.99
			Y	0.31	0.00	-7.55	7.72
			Z	0.66	0.00	-5.81	5.87
LID_7ST	DMC_ACX	0.79	X	0.33	0.00	-8.10	7.61
			Y	0.31	0.00	-7.57	7.46
			Z	0.65	0.00	-5.74	5.72
LID_4ST	DMC_PATB	0.90	X	0.33	0.00	-8.45	8.05
			Y	0.40	0.00	-8.40	7.71
			Z	0.73	0.00	-6.15	6.25
LID_4ST	DMC_ACX	0.90	X	0.33	0.00	-8.45	8.06
			Y	0.41	0.00	-8.24	8.54
			Z	0.73	0.00	-6.33	6.14
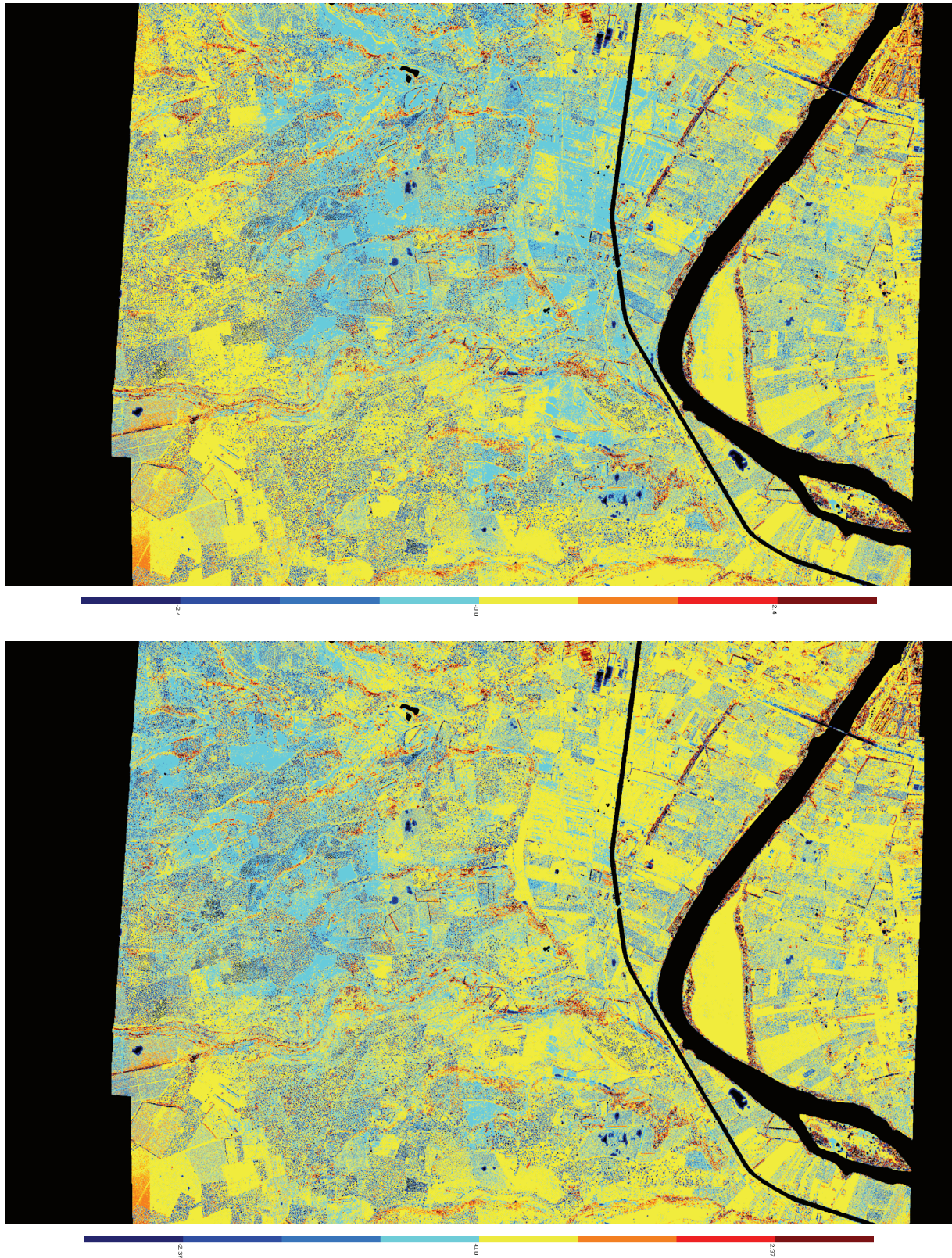
Figure 27. Residuals (3D spatial differences between master and slave DSMs) for PAT-B (top) and ACX (bottom) orientations. Note the residual differences in the upper left and central part, where the two orientations differed most. Larger differences at discontinuities (top right at urban area) and systematic effects at lower left (orange jump) are distinguishable. Each color bar segment is one sigma (about 0.8 m).

Table 11 shows the results of the LS3D matchings. Some preliminary tests showed that only the translations of the 7-parameter transformation were significant. The results for the two orientations are very similar except for Tz in the 4-strip LIDAR area. The reason is that these numbers are global and are not significantly influenced apparently from local differences between the two orientations. The translation values represent the bias between the two DSMs. In planimetry, this bias is due to the different orientation of images and LIDAR, and is significant only in Y (N/S) direction. In height, the bias is possible due to the same reason and additionally due to partial penetration of vegetation by the LIDAR data (note that the matching DSM is higher than the LIDAR heights, as the negative sign of Tz shows).

The sigma a posteriori is the standard deviation of the 3D spatial differences (shown in Figure 27) between slave and master DSMs after performing the translation. Its decomposition in X, Y, Z components is shown in Table 12. Again, there is no significant difference between the two image orientations. The X and Y values are similar and about 0.3 m, while in height it is about 0.65 m. This is actually the difference between the two DSMs after removing the systematic bias in X, Y and Z. The differences are higher at surface discontinuities, possibly also due to modeling errors, i.e. in the upper right urban area (Figure 27). The matching DSM shows a jump in the bottom left part. The possible explanation is the change of matching from the use of 4 images to the use of 3 at this position.

The achieved standard deviation of the height differences was about 0.65m. With a better orientation, usage of APs in the bundle adjustment and DSM generation and without the differences due to vegetation penetration, we expect this difference to drop quite below 0.5 m. It should be noted that the LIDAR data is not as good as to be reference.

6.3.7. Assessing changes of forest area and shrub encroachment

This is an assessment study of change (1997 – 2002) of forest and other wooded areas in a mire biotope in the Pre-alpine zone of Central Switzerland using airborne remote sensing data. The study is a cooperation between the IGP (ETH Zurich) and the Department of Landscape Inventories of Swiss Federal Research Institute WSL. More details are given in Waser et al. (2007).

6.3.7.1. Study area and data sets

The study area is located on a small plateau in the East of the Lake of Zug, a sensitive environmental area in the Pre-alpine zone of Central Switzerland (approx. 47°07' N and 8°32' E). The mire covers an area of 2.61 km2 whereas 1.72 km2 belong to the core area. The altitude varies from 850 m to 1000 m above sea level. The bordering forested area, with an extent of approx. 0.85 km2, is mostly characterized by open mixed forest (40%) and coniferous forest (60%) with some storm losses caused by hurricane Lothar in 1999 and some deforestation in the last years.

Three DSMs generated from two set of CIR-aerial images (year 1997 and 2002) and an airborne laser scanning point cloud (year 2001) were used. There are 4 CIR-aerial images (1 strip) of 1997 and 12 (2 strips) of 2002. Table 13 gives an overview of the image data used in this study.

Table 13. Characteristics of the CIR-aerial images.

Imaging parameters	CIR-aerial images 1997	CIR-aerial images 2002
Camera	RC 30	RC 30
Acquisition date	04/08/1997	08/07/2002
Image scale	1:10,000	1:5,500
Focal length	21 cm	30 cm
Spectral resolution	Green: 500-600, Red: 600-700, NIR: 750-1000 nm	
Scan/Ground pixel size	15 μm / 15 cm	15 μm / 8.25 cm
Radiometric resolution	8 bit	8 bit
Overlap	Forward: 75%	Forward: 75%, Sideward: 30%

All images were digitized with a Vexcel UltraScan scanner. The 1997 film images had severe scratches on the emulsion side, causing artifacts in the digitized images and DSM errors in the automated DSM generation. Image orientation was established with 15 ground control points

measured by a differential GPS survey and with using bundle adjustment of SocetSet V5.2. The sigma naught of orientation was 0.20 pixel and 0.23 pixel for 1997 and 2002, respectively.

Two DSMs were generated automatically from the above images of the years 1997 and 2002 respectively, using SAT-PP (Figure 28). It uses a coarse-to-fine hierarchical matching method with an effective combination of several image matching algorithms and automatic quality control (Zhang and Gruen, 2004). The DSMs have a grid spacing of 0.5 m.

National LIDAR data of the Swiss Federal Office of Topography (Swisstopo) was acquired in 2001 with leaves off. From the raw data, both a DTM and DSM were generated by Swisstopo. The average density of the DSM data was 1-2 points / m2 and the height accuracy (1 sigma) 0.5 m for open areas and 1.5 m for terrain with vegetation. The DTM had an average point density of 0.8 points / m2 and a height accuracy (1 sigma) of 0.5 m. The DSM and DTM were interpolated to a regular grid with 2.5m grid spacing.
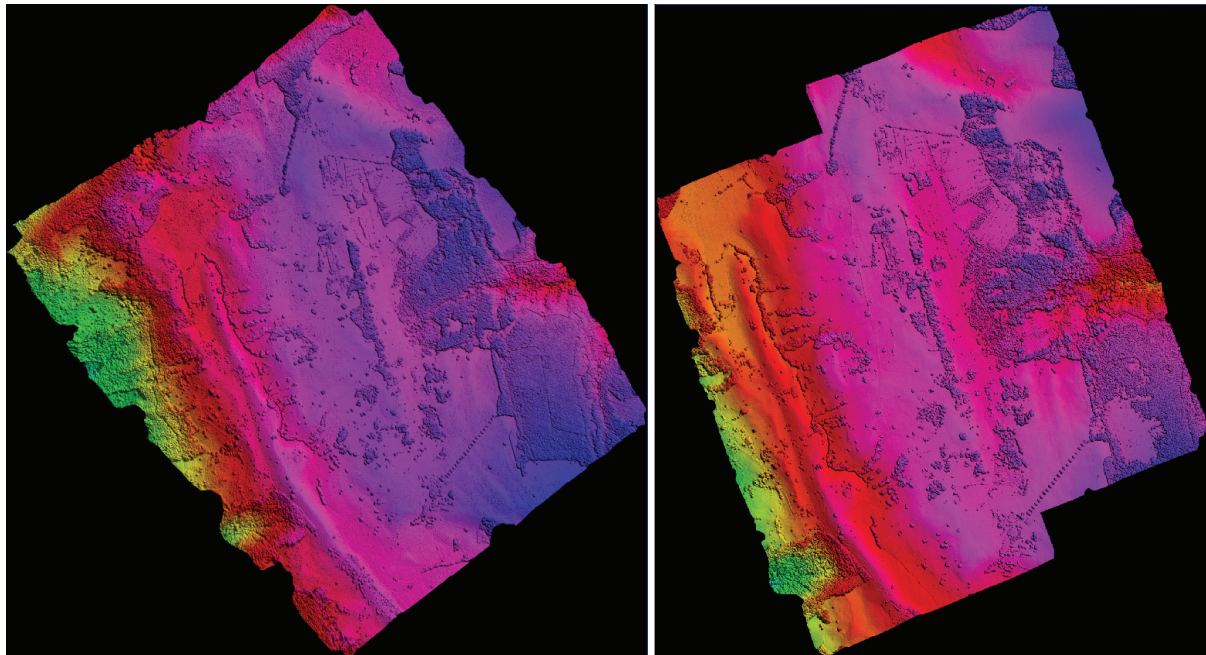
Figure 28. Color coded DSMs from 1997 (left) and 2002 (right). Significant deforestation in 2002 is apparent, especially on the bottom right part of the model.

6.3.7.2. Co-registration and change detection

The matching DSMs of 1997 and 2002, and the LIDAR DSM and DTM were co-registered using the LS3D surface matching method. The co-registration uses a 7-parameter 3D similarity transformation to remove systematic differences (bias) between two datasets, e.g. due to different image orientation. For the estimation of these parameters, we used control surfaces, i.e. DSM parts that did not change in the two datasets, i.e. bare ground, and also removed large differences due to matching errors with a robust filtering. Among the 7 parameters, only the three X, Y, Z shifts were significant in this case. After co-registration, the Euclidian distances between the two datasets are computed as well as the X, Y, Z components, the latter being more important for these investigations. After co-registration, different products could be generated and conclusions drawn. The difference 2002-1997 matching DSM gives the changes between the two epochs, especially regarding vegetation. After co-registration, the Z-component of the Euclidian distances (sigma a posteriori) was 3.4 m, showing a clear reduction of vegetation from 1997 to 2002.

The difference matching DSMs minus LIDAR DTM gives the normalized DSMs, i.e. the 3D objects in the scene and especially the canopy models. The LIDAR DSM was also subtracted from the 2002 DSM, in spite of the small time difference. This could give a comparison between the two DSMs and also an indication to what extent LIDAR penetrates the tree canopy more compared to matching, a characteristic that was observed in previous studies (see Baltsavias et al., 2006 and Chapter 6.3.5).

After co-registration, the Z-component of the Euclidian distances (sigma a posteriori) was 0.8 m, however, there is no indication as to whether the LIDAR or the matching DSM is more accurate. Results are shown in Figures 29 and 30.
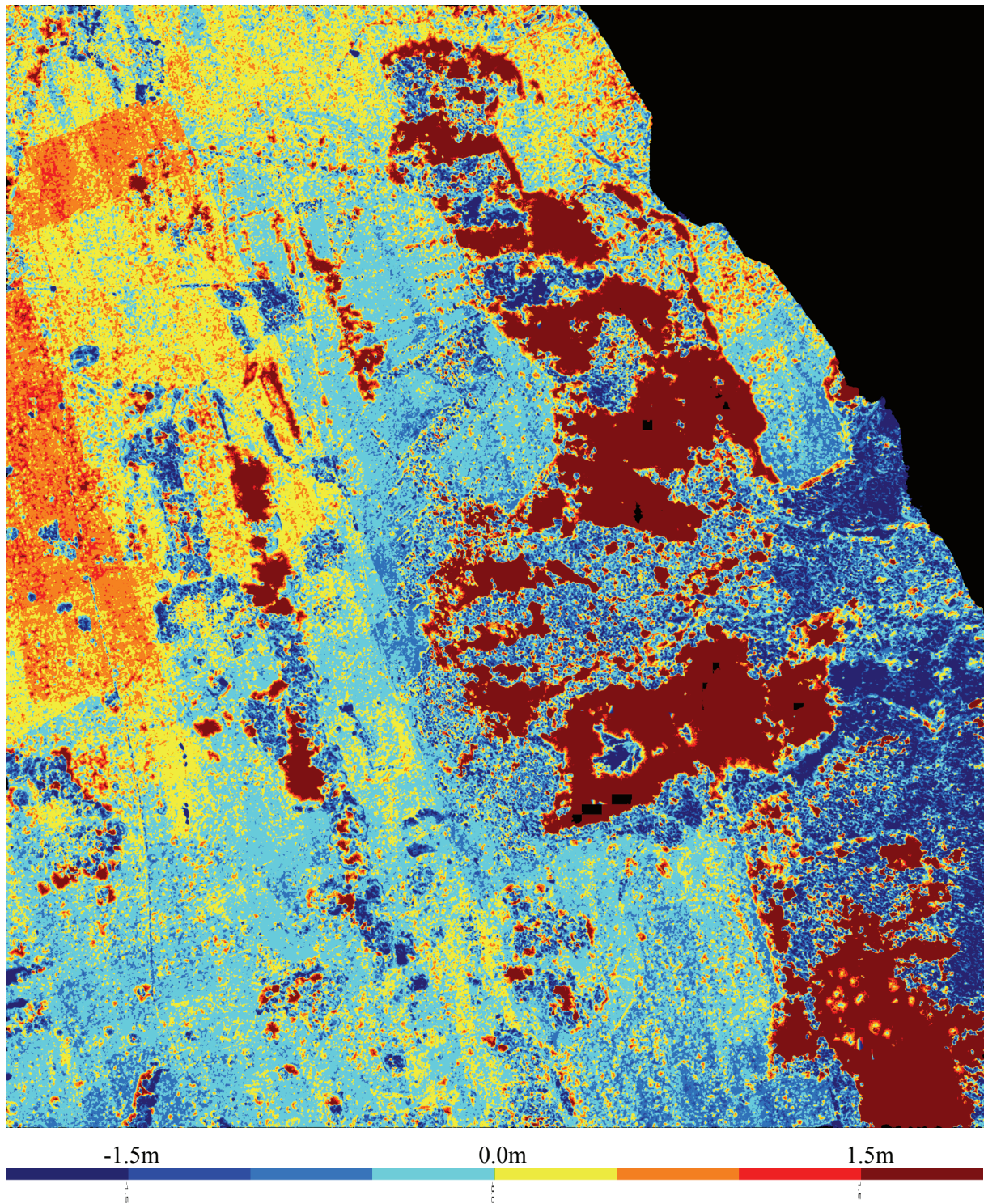

Figure 29. The Z component of the Euclidian distances between 1997 and 2002 matching DSMs shows clearly areas of deforestation and shrub encroachment. The 2002 matching DSM is the reference surface and the 1997 matching DSM is the transformed one. Red areas show the deforestation.
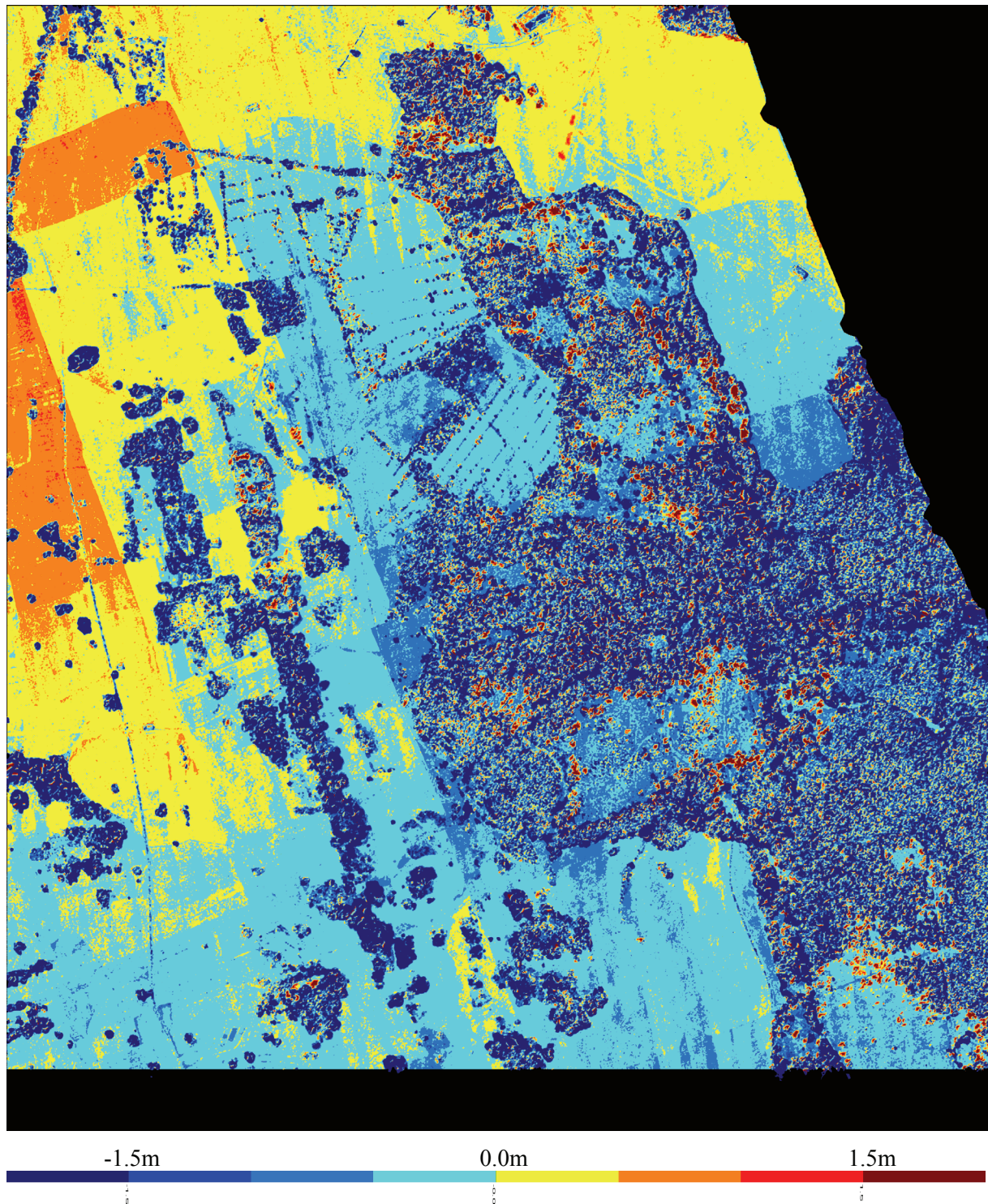
-1.5m   0.0m   1.5m

Figure 30. The Euclidian distances between the 2001 LIDAR DSM (search) and the 2002 matching DSM (template) showing that LIDAR measures tree canopies lower than the image matching. At the top and bottom, the effect of the stripes in the matching DSM, possibly due to film scanner (geometric) miscalibration is visible. The orange areas at the top left are due to differences in image orientation between the two flight strips and within each strip causing discontinuities in the 2002 matching DSM. These areas are also visible in Figure 29 but have less sharp boundaries due to the noise of the 1997 matching DSM. The small red spots, mostly inside the forest, show the loss of individual trees during one year time difference.

6.3.8. Accuracy assessment of the SRTM C-Band DEMs

We compare the SRTM DEM with respect to a reference DEM whose quality and production details are known by us. The reference DEM was generated from optical satellite imagery and processed by use of SAT-PP.

The LS3D is run in three different degree of freedom (DOF) modes, i.e. 6 DOF with rotation and translation parameters, 3 DOF with only translation parameters, and 0 DOF without any transformation. Based on the initial experiments, it was found that the scale factor is not significant. So, the 7 DOF version with the full set of parameters was skipped.

The initial values are given as 0.0 for the rotation and translation parameters. The estimated parameters show the existence of possible rotation and positional shift differences between the coordinate systems. The sigma naught value is a quality measure for the final agreement of the surfaces.

Coordinate values of the template and the search surfaces are not centered before the matching. This leads high (algebraic) correlations between the rotation angles and translation elements, as seen significant differences between the translation elements of the 3 DOF and 6 DOF versions in Tables 15 and 16.

6.3.8.1. Reference DEM - Hobart

The test site (147^0.280E, 42^0.860S) is located in the south part of the island of Tasmania (Australia), close to Hobart city (Figure 31a). It is covered with dense vegetation. The elevation ranges from the mean sea level to 1280 meters. Technical details of the reference DEM are given in Table 14.

Table 14. Technical details of the reference DEM of Hobart.

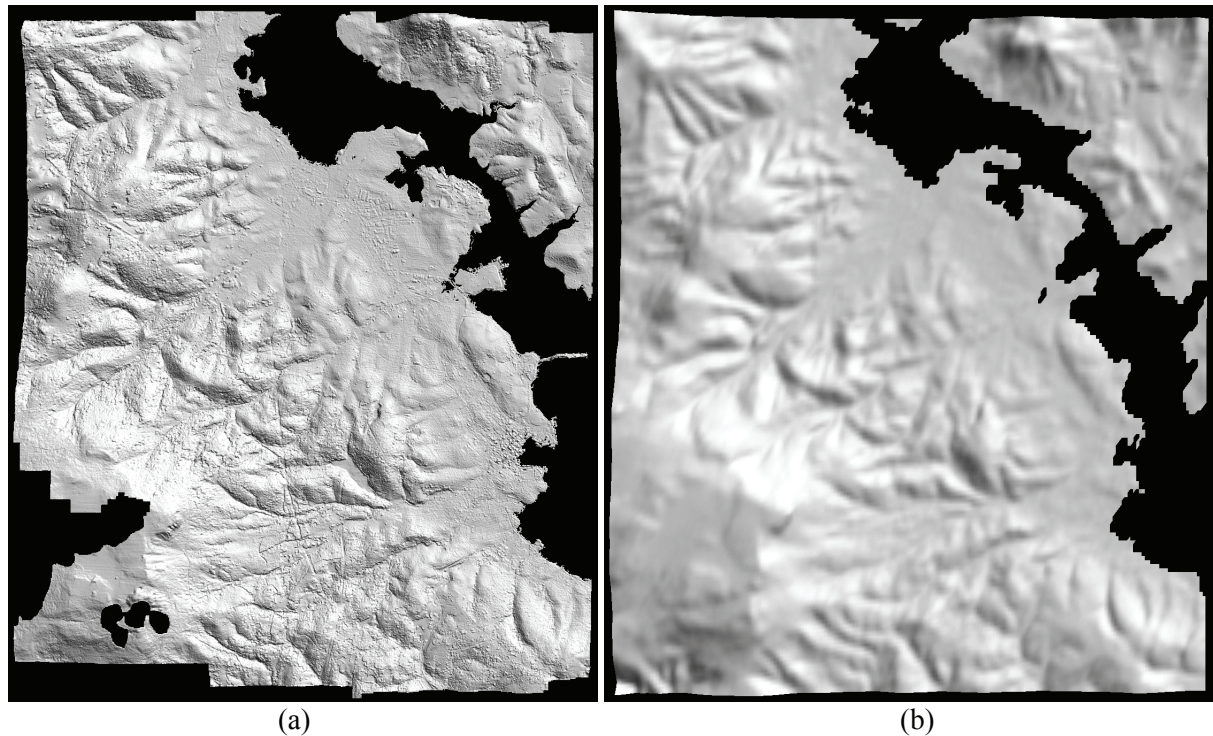| Test site	Area size Lon x Lat (degree)	Sensor	DEM Resolution (meters)	H-datum V-datum	No. cols x rows	H-accuracy V-accuracy (meters)
AUS	0.15 x 0.13	IKONOS	5	WGS84 WGS84	2511 x 3032	1.0 1.0 – 3.0

(a)   (b)

Figure 31. The reference IKONOS DEM (a) and its corresponding SRTM C-Band DEM (b).

6.3.8.2. SRTM C-Band DEM – Hobart

The C-Band DEM (Figure 31b) was downloaded from the FTP server of the Land Process Distribution Active Archive Center (LP DAAC). The C-Band DEMs are organized into individual tiles, each of which is a data file with a *.HGT suffix at the file name. Each tile covers an area of 1^0 x 1^0 in longitude and latitude. The horizontal coordinates are given in Geographical Coordinate System (GCS) defined on the WGS84 (World Geodetic System 1984) ellipsoid, while elevations are in meters referenced to the WGS84 EGM96 (Earth Gravitational Model 1986) geoid, which approximates the mean sea level (MSL).

Firstly, the HGT file was converted to the ESRI ASCII grid (*.ASC) format maintaining the unit and reference system of the point coordinate values. This is basically a step to convert the data from binary to ASCII. In a subsequent step, the elevation values were transformed to the ellipsoidal heights so that they are compatible with the vertical datum of the reference DEM. A 15-minute worldwide geoid height file provided by the National Geospatial-Intelligence Agency (NGA, http://earth-info.nga.mil/GandG/wgs84/gravitymod/) was used in the computation. The geoid undulations were calculated using bi-linear interpolation.

Finally, the ASC files were converted to XYZ point list files (*.XYZ) while transforming the points from the geographical coordinates to the UTM coordinates. This procedure does not perform any resampling. The original resolution is maintained by employing such a conversion strategy. The final XYZ files are in TIN form rather than at a regular grid. The average point spacing is 68 meters along the east direction and 92 meters along the north direction.

The data conversion pipeline is given in Figure 32. All steps of the data conversion were performed using self-developed software.
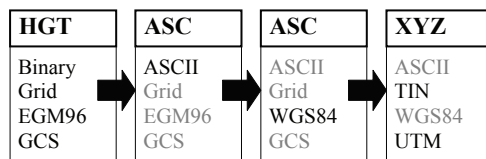
HGT	**ASC**	**ASC**	**XYZ**
Binary Grid EGM96 GCS	ASCII Grid EGM96 GCS	ASCII Grid WGS84 GCS	ASCII TIN WGS84 UTM

Figure 32. The data conversion pipeline for the C-Band DEM.

6.3.8.3. Quantitative results of the Hobart test site

The SRTM C-Band DEM (search surface) of the Hobart area was co-registered to the reference DEM (template surface). The results are given in Table 15.

Table 15. Results of the analysis of the C-Band DEM at the test site Hobart.

DOF	No. of valid points	No. of used points Excluded %	Sigma (m) Sigma x/y/z (m)	Mean (m) Min / Max (m)	Tx / Ty/ Tz (m) ω / φ / κ (grad)
0	6,178,111	5,964,655	6.8	-1.1	Na
		3.5 %	1.5 / 1.5 / 6.5	-92.0 / 44.4	Na
3	6,178,111	5,958,371	6.2	-0.0	-4.58 / -9.66 / 1.59
		3.6 %	1.3 / 1.3 / 6.0	-61.8 / 43.8	Na
6	6,178,111	5,958,310	6.2	-0.0	-1.10 / -11.71 / 12.20
		3.6 %	1.3 / 1.3 / 5.9	-61.8 / 44.6	-0.008 / 0.012 / 0.005

A small portion of the points (as outliers of the C-Band DEM) was excluded by the robust weighting scheme (Equation 3.31). The surface co-registrations with 3 DOF and 6 DOF have not improved the sigma a posteriori values significantly. This shows that there is no coordinate system difference between the reference DEM and the C-Band DEM. They are already in agreement. The surface co-registration cleared the -1.08m bias, which is most probably due to penetration property of C-SAR wavelength into vegetation. In Figure 33a, 33b and 33c, blue color shows the areas where C-Band DEM is below the reference IKONOS DEM.

In spite of excluding the 3.6% of large outliers, there are still very large deviations at some spots in the range of -61.8 to +43.8 meters.
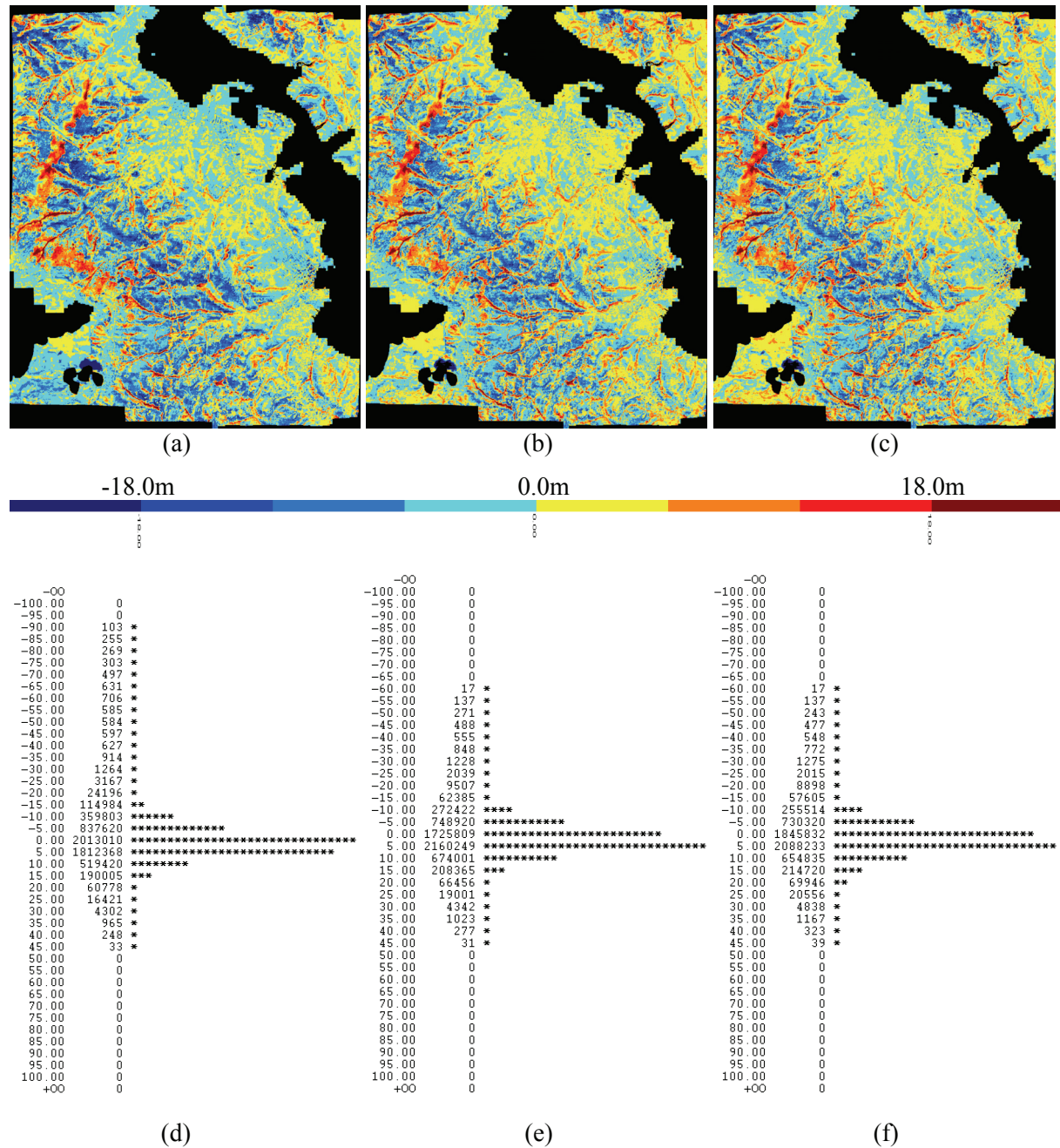
Figure 33. Colored spatial (distance) discrepancies between the reference and C-Band DEMs of the Hobart test site before the LS3D surface matching, i.e. 0 DOF version (a), after the matching of the 3 DOF version (b), and after the matching of the 6 DOF version (c). Frequency distributions of the spatial (distance) discrepancies of the 0 DOF (d), 3 DOF (e) and 6 DOF (f) versions. The residual bar unit is meter.

6.3.8.4. Cross-comparison of the SRTM C- and X-Band DEMs – Neuschwanstein

A SRTM X-Band DEM tile, covering an area of 15' x 15' (arc-minute) around Neuschwanstein (Bavaria, Germany) was downloaded from the DLR website: http://www.dlr.de/srtm/produkte/demo_en.htm . The X-Band DEM is in the Digital Elevation Data (DTED) format with *.DT2 suffix at the file name. The same conversion procedure as given in Figure 32 was applied to the X-Band DEM as well, except the vertical datum transformation.

The average point spacing is 18 x 30 meters (along east x north directions) for X-SAR DEM and 62 x 90 meters for C-SAR DEM. Both the X-Band DEM and C-Band DEMs are given in Figure 34.

(a)   (b)
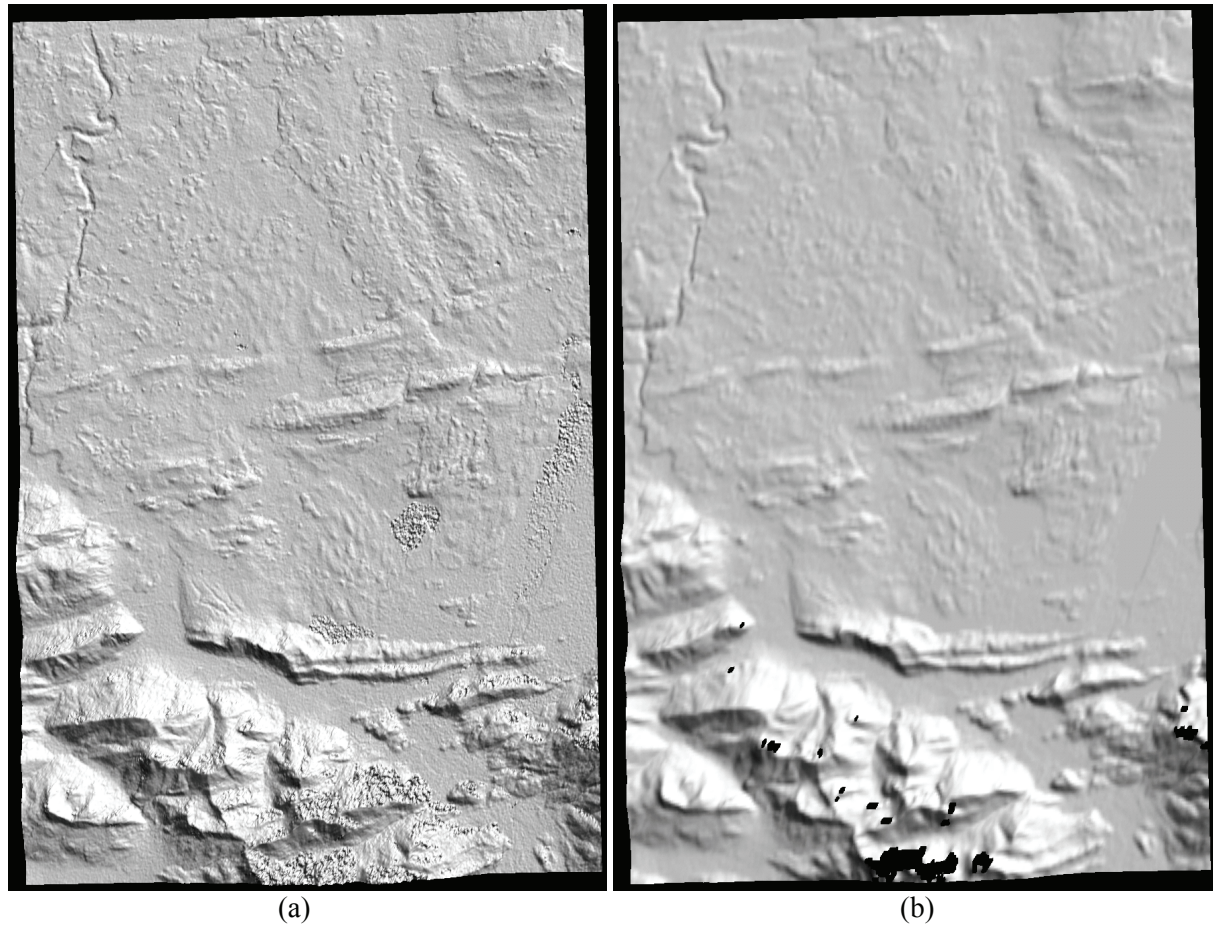
Figure 34. SRTM X-Band DEM of the Neuschwanstein area (a) and its C-Band DEM counterpart (b).

Table 16. Results of the cross-comparison of the X- and C-Band DEMs at the test site Neuschwanstein.

DOF	No. of valid points	No. of used points Excluded %	Sigma (m) Sigma x/y/z (m)	Mean (m) Min / Max (m)	Tx / Ty/ Tz (m) ω / φ / κ (grad)
0	810,000	804,575 0.7 %	10.8 2.7 / 4.6 / 9.4	2.4 -284.8 / 407.8	Na Na
3	810,000	796,325 1.7 %	6.0 1.3 / 1.8 / 5.5	-0.1 -58.9 / 58.9	0.17 / 5.41 / -3.11 Na
6	810,000	793,802 2.0 %	5.5 1.2 / 1.6 / 5.1	-0.0 -54.1 / 54.5	10.29 / 1.93 / 11.13 -0.013 / -0.004 / 0.009

The X-Band DEM is the template surface, and the search surface C-Band DEM is transformed to the template's reference system.

Without co-registration, the C-Band DEM is clearly above the X-Band DEM with a mean bias value of +2.43 meters. The LS3D co-registration clears this shift value (Figure 35). The co-registration improves the a posteriori sigma value by a factor 2.

(a)   (b)   (c)

(d)   (e)   (f)
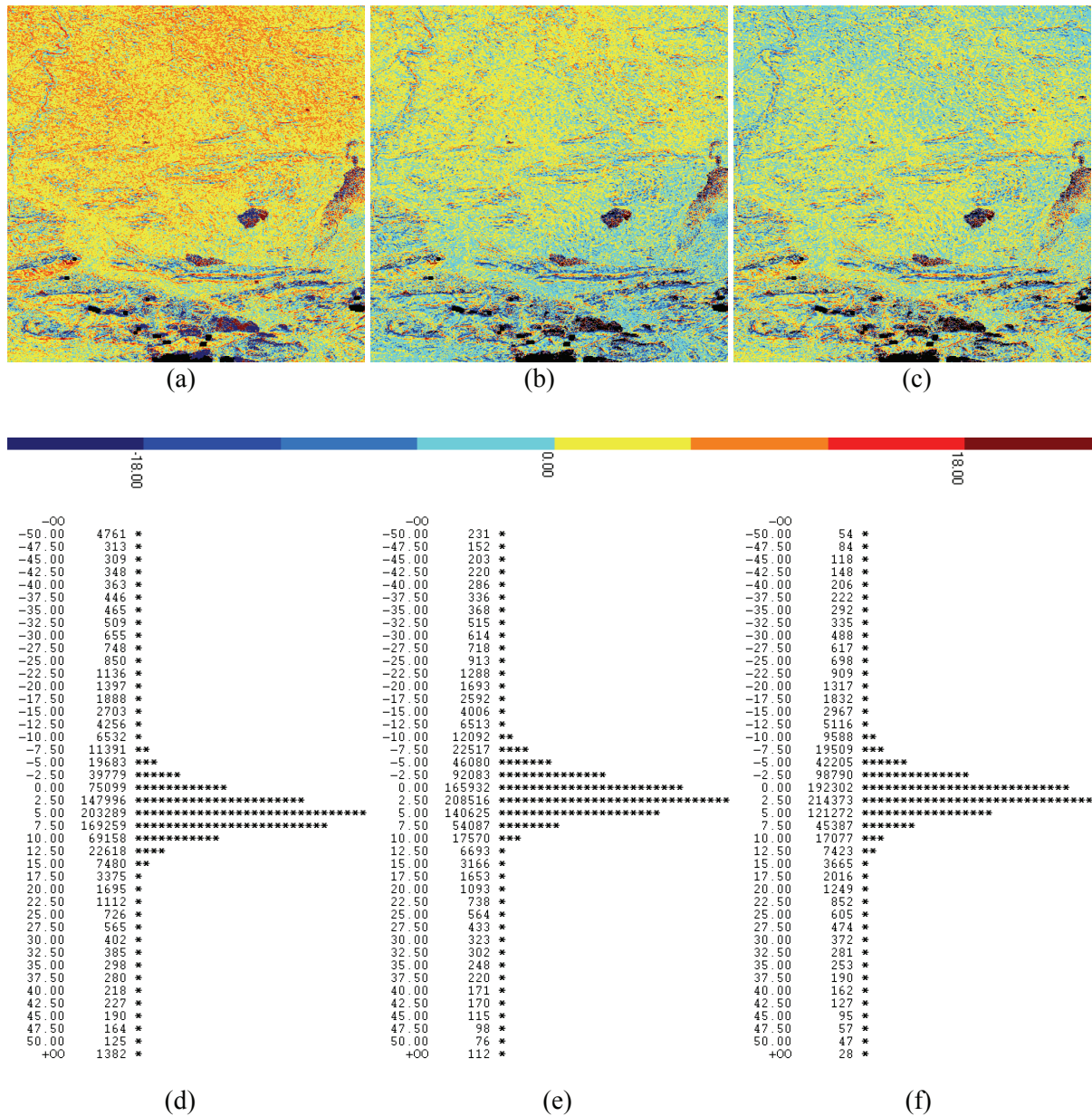
Figure 35. Cross-comparison between the X- and C-Band DEMs at the test site Neuschwanstein. Colored spatial (distance) discrepancies between the X- and C-Band DEMs for the 0 DOF (a), 3 DOF (b) and 6 DOF (c) versions. Frequency distributions of the spatial (distance) discrepancies of the 0 DOF (d), 3 DOF (e) and 6 DOF (f) versions. The residual bar unit is meter.

7

CONCLUSIONS AND OUTLOOK

7.1. Summary

This thesis work introduces an algorithm for the co-registration of 3D surfaces, intensities, curves and sparse pointclouds. The proposed method is mathematically based on the Least Squares matching, which is a fundamental measurement algorithm and a powerful solution for many essential photogrammetric tasks.

It formulates the problem as the Least Squares matching of one or more fully 3D surfaces with a template one. Each template to search surface correspondence gives an observation equation to the design matrix. The observation equations functionally relate the observations of the template to the transformation parameters of the search surface. 3D transformation parameters of the search surface, which satisfy a Least Squares matching to the template, are to be estimated. Although the software implementation uses a 7-parameter 3D similarity transformation, an extension to higher order transformations is possible.

The Least Squares image matching evaluates the grey level differences, whilst the surface matching evaluates the Euclidean distances. The shortest Euclidean distance of each template surface element to the search surface is searched. This correspondence search procedure takes the main part of the computational effort. On the contrary, the correspondence search is very simple in the image matching case. The surface matching uses the 3D transformations as the geometric relationship, while the image matching uses a 2D Affine model for this purpose. These are the basic formulation differences between both techniques.

The transformation parameters are introduced into the system as fictitious observations with a priori weights. The weights are chosen according to a priori knowledge about the parameters. By associating a zero or infinitely large weight, an individual parameter can be assigned as free variable or constant. The software can run in different transformation modes: similarity (full set of parameters), rigid body (3 translations and 3 rotations), tilt (3 translations, ω, and φ), yaw (3 translations and κ), translational bias (3 translations), rotation (only 3 rotations), horizontal shift (t_x and t_y), and depth (t_z), etc.

The basic estimation model uses the Generalized Gauss-Markoff model. In fact, it is a typical Least Squares adjustment with observation equation systems, which is a well-known adjustment calculus method in geodesy and photogrammetry. Here, we are faced with a particular case. The unknown function (the search surface itself) is not analytically continuous. The functional derivations are not applicable, since we do not know the function mathematically. Thus, the numerical derivatives are employed. For this particular mathematical model, they correspond to the local surface normals. The proof of this is given in Chapter 3.2.

The correspondence of each element of the template surface must be identified on the search surface. This requires heavy computation for correspondence search. The computational expense of this task is reduced by employing a 3D boxing structure. It partitions the search domain into 3D cubes, so that the correspondence is only searched in the coincident and neighboring boxes. The 3D boxing structure is designed in a way that it also efficiently works for transforming (floating) data sets by a 7-parameter similarity transformation model. While the solution is refined through the iterations, the correspondence search is turned into a local neighborhood search. In the case of oscillation, it again turns back to the boxing. Both techniques (boxing search and local neighborhood search) together establish a hierarchical and adaptive way for the correspondence search.

When multiple overlaps occur, a two step solution is adopted. The pairwise LS3D matchings are run for every possible combination. In order to prevent repetition, only the forward matchings are applied. Suppose that the *i*-th and *j*-th surfaces have an overlap. Only *i*-to-*j* LS3D matching is applied, not both *i*-to-*j* and *j*-to-*i*. The pairwise co-registrations establish the local geometric relationships among the surfaces. The global consistency is set up by an additional global registration step. For this purpose, the block adjustment by independent models is used.

The intensity matching approach accommodates the available attribute information and surface geometry under a combined estimation model. If available, any kind of functional constraint can also be introduced to the system. The attribute information is utilized by generating the quasisurfaces in addition to the actual ones. Any type of attribute information contributes one more quasisurface layer to the data. Therefore, it generalizes the problem to matching of multiple isosurfaces rather than single layered surfaces.

The mathematical model is flexible. Many relevant problems can be formulated as extensions of the basic model. Some of them are given conceptually: matching of 3D curves with each other or with a 3D surface, matching of 3D sparse points with a 3D surface and simultaneous matching and georeferencing of multiple 3D surfaces and intensity information.

7.2. Conclusions

Our basic estimation model is a generalization of the Least Squares matching concept for the 3D surface matching problem. It is an algorithmic extension of the early 2D image matching version.

The current implementation uses a 3D similarity transformation model for the geometric relationship. The unknown transformation parameters are treated as observables with proper weights, so that sub-versions of the 7-parameters model can be run, i.e. rigid body, tilt, translation, horizontal shift, depth, etc. If a higher order transformation is demanded, it can easily be introduced.

The LS3D fully considers the 3D information by evaluating the Euclidean distances. The 2.5D surface matching algorithms, some of which are given in Chapter 2, evaluate the height differences, which is sub-optimal even for terrain surface applications. They cannot consider modeling errors, whereas the proposed LS3D method can do so.

The estimation model is the Generalized Gauss-Markoff model. It is a strict and rigorous formulation, which describes the physical nature of the problem. It provides a flexible mathematical basis, which makes further algorithmic extensions possible, as given in Chapters 4 and 5.

The Generalized Gauss-Markoff model has a quadratic type of convergence rate. This gives substantially less number of iterations than the ICP variants, whose convergence behavior is monotonic.

The Least Squares concept allows for the monitoring of the quality of the final results by means of precision and reliability criterions. The precision and reliability measures give a quantitative insight into the data content, and help to assess the level of success of the solution. The quality of any individual parameter can be checked via the a posteriori variance-covariance matrix. This feature can be highly important when the data set does not contain sufficient surface information along one or more coordinate directions in order to support the computation of all transformation parameters. The parameters with low precision values help to diagnose and to understand the configuration and content of the data. Examples are given in Chapters 6.1 and 6.2.

A simple but effective error detection module was implemented. It consists of three parts. An optional median type of filtering is carried out at the pre-processing step. It aims to discard the erroneous points on poorly or extremely reflecting surfaces (e.g. black surfaces or glass) or points on the object silhouette due to surface discontinuity, which typically exist in many laserscanning pointclouds. During the iterations, a simple robust weighting principle is applied to the individual observation equations. Any observation with the Euclidean distance (discrepancy) exceeding the limit value given in Equation (3.31) is excluded from the design matrix. The limit value is a constant factor K of the sigma naught a posteriori. It can be set according to a given confidence level. Finally, we reject the

correspondences containing points on the mesh boundaries. The overall strategy successfully eliminates the false correspondence due to occlusions and outliers.

The constant value, K in Equation (3.31), can be altered according to the task. If it is an ordinary surface co-registration work, it should be set to a high value (e.g. $K>8$ or >10) to reduce type I errors confidently. Because of the high redundancy of a typical data set, a certain amount of occlusions and/or smaller outliers, i.e. type II errors, do not have significant effect on the estimated parameters. If it is a change detection or deformation study, the constant value K should be selected based on the a priori knowledge in order that the changed or deformed parts are appropriately excluded from the estimation.

Since the estimation model is non-linear, the method needs initial approximations of the parameters. The initial approximations should be given or should be calculated prior to matching. To define a convergence radius value is extremely difficult. It depends on the geometric information of the object surface. It is our experience that the convergence is more sensitive to the initial values of the rotation angles than the translation elements.

The capability of matching of surfaces of different quality and resolution is another positive aspect of the proposed method. This has two reasons. The first is certainly the rigorous mathematical formulation. The second is the selectivity of construction of the design matrix based on the choice of the better surface, either the template or the search surface, as explained in Chapter 3.3. The SRTM TerrainScape work, in cooperation with Swissphoto AG, proves this capability. Swissphoto AG has matched many DEMs all around the world with the SRTM C-SAR DEMs. The local DEMs are in any accuracy, point spacing and production techniques. According to their report, a complete failure case has not happened, except for some software debugging cases.

The simultaneous multi-subpatch approach (Chapter 3.8.2) can be very useful for the change detection and deformation analysis studies in addition to computational acceleration. Change or deformation free parts (control patches) can be selected as cooperative multi-subpatches. Thus, inspection areas, which are probably deformed or changed, are confidently excluded from the registration. The forestry application exploits this feature.

Experiments show that as long as the object surface has minimal information, e.g. in the case of very small structures on it, the basic algorithm, which uses only surface geometry, can find an acceptable solution. When the object surface is a plane or sphere, the surface geometry approach does not numerically fail as the sensor noise prevents the normal equation matrix from becoming singular. However, it finds a side minimum as the solution. In this case, the proposed method can find a reliable solution by introducing supplementary attribute information into the system. In the experiments, the laser scanner derived intensities were used as the supplementary information. The practical examples demonstrate the capability of the technique. Special attention should be paid to the radiometric variations between the surfaces. Additional radiometric correction parameters have been added to the mathematical model. This gives better results than the pre-processing option. The concept is not restricted to the registration of laser scanner pointclouds. It can find more application areas for cases where diverse types of attribute information are used.

7.3. Outlook

Our experiences were very positive and the procedures worked very well. However, there is still need for further improvements and extensions. These are listed below.

- The iteration can start with a high order 3D transformation or a linear transformation with many terms, e.g. a 3D affine transformation. In the course of the iteration, non-determinable parameters are excluded by an appropriate determinability test. Thus, the parameter vector is adapted to the nature of the data in a self tuning and adaptive way.

- As mentioned in Chapter 3.4, the search surface contains the stochastic properties unless it is an object surface which can be described analytically as a whole (without noise). This fact is neglected in the estimation model. As a more comprehensive model and in order to have

realistic precision estimates, the estimation model can be replaced by an error-in-variables model.

- Due to the non-linear functional model, initial approximations of the parameters are needed. For full automation, a pre-alignment method can be integrated.

- The current implementation uses two first degree surface representations (planar triangle mesh and bi-linear grid mesh). Higher order surface forms theoretically give better surface modeling (in sparse data cases), in consequence better results for the multi-resolution case, but with the cost of additional computational expense.

- For the co-registration of multiple surfaces, a one step simultaneous solution as given in Chapter 5.4.1 should be realized.

- The intensity matching approach uses a simple radiometric model, which maps the intensity values perpendicular to the geometric surface. This model should be improved by a strict model, which applies the mapping along the projection center to object surface considering the data acquisition geometry and radiometry (illumination conditions and sensor properties).

- Implementations and testing of conceptual extensions are needed for

    o Least Squares 3D curve matching

    o matching of 3D curves with a 3D surface

    o matching of 3D sparse points with 3D surfaces

    o generalized multiple 3D surface and intensity matching

- A combined co-registration and georeferencing approach might be very useful for many geodetic and photogrammetric applications. It performs the co-registration and the georeferencing tasks under one mathematical model simultaneously.

BIBLIOGRAPHY

Ackermann, F., Ebner, H., and Klein, H., 1973. Block triangulation with independent models. Photogrammetric Engineering and Remote Sensing 39 (9), 967-981.

Ackermann, F., 1984. Digital image correlation: performance and potential application in photogrammetry. Photogrammetric Record 11 (64), 429-439.

Akca, D., Remondino, F., Novàk, D., Hanusch, T., Schrotter, G., and Gruen, A., 2007. Performance evaluation of a coded structured light system for cultural heritage applictions. Videometrics IX, Proc. of SPIE-IS&T Electronic Imaging, San Jose (California), USA, January 29-30, SPIE vol. 6491, pp. 64910V-1-12.

Akca, D., Gruen, A., Alkis, Z., Demir, N., Breuckmann, B., Erduyan, I., and Nadir, E., 2006. 3D modeling of the Weary Herakles statue with a coded structured light system. International Archives of the Photogrammetry, Remote Sensing and Spatial Information Sciences 36 (5), 14-19.

Al-Manasir, K., and Fraser, C.S., 2006. Registration of terrestrial laser scanner data using imagery. The Photogrammetric Record 21 (115), 255-268.

Arun, K.S., Huang, T.S., and Blostein, S.D., 1987. Least-squares fitting of two 3D point sets. IEEE Transactions on Pattern Analysis and Machine Intelligence 9 (5), 698-700.

Baarda, W., 1968. A testing procedure for use in geodetic networks. Netherlands Geodetic Commission, Delft, Vol. 2, No. 5, 97 p.

Baltsavias, E., Gruen, A., Küchler, M., Thee, P., Waser, L.T., and Zhang, L., 2006. Tree height measurements and tree growth estimation in a mire environment using digital surface models. In Proceedings of Workshop on 3D Remote Sensing in Forestry, 14 – 15 February, Vienna, Austria, 9 p. Available at ftp://igpho.ethz.ch/ ub/manos/papers/vienna06_manos.pdf (accessed 23 October 2006).

Beinat, A., and Crosilla, F., 2001. Generalized Procrustes analysis for size and shape 3D object reconstructions. Optical 3-D Measurement Techniques V, Vienna, October 1-4, pp. 345-353.

Benjemaa, R., and Schmitt, F., 1997. Fast global registration of 3D sampled surfaces using a multi-z-buffer technique. IEEE International Conference on 3D Digital Imaging and Modeling, Ottawa, pp. 113-120.

Bentley, J.L., 1975. Multidimensional binary search trees used for associative searching. Communication of the ACM 18 (9), 509-517.

Bergevin, R., Soucy, M., Gagnon, H., and Laurendeau, D., 1996. Towards a general multi-view registration technique. IEEE Transactions on Pattern Analysis and Machine Intelligence 18 (5), 540-547.

Besl, P.J., and McKay, N.D., 1992. A method for registration of 3D shapes. IEEE Transactions on Pattern Analysis and Machine Intelligence 14 (2), 239-256.

Blais, G., and Levine, M.D., 1995. Registering multiview range data to create 3D computer objects. IEEE Transactions on Pattern Analysis and Machine Intelligence 17 (8), 820-824.

Blais, F., Taylor, J., Cournoyer, L., Picard, M., Borgeat, L., Dicaire, L.G., Rioux, M., Beraldin, J.-A., Godin, G., Lahanier, C., and Aitken, G., 2005. Ultra-high resolution imaging at 50 µm using a portable XYZ-RGB color laser scanner. Int. Workshop on Recording, Modeling and Visualization of Cultural Heritage, Ascona, May 22-27, (on CD-ROM).

Breuckmann, B., 2003. State of the art of topometric 3D-metrology. Optical 3-D Measurement Techniques VI, Zurich, Switzerland, Sept. 22-25, Vol. II, pp. 152-158.

Brinkhoff, T., 2004. Spatial access methods for organizing laserscanner data. International Archives of Photogrammetry, Remote Sensing and Spatial Information Sciences 35 (B4), 98-102.

Brodie, N., Doole, J., and Watson, P., 2000. Stealing history: The illicit trade in cultural material. The McDonald Institute of Archaeological Research, Cambridge, UK, pp. 31-32.

Brodie, N., 2003. Stolen history: looting and illicit trade. Museum International 55 (3-4), 10-22.

Campbell, R.J., and Flynn, P.J., 2001. A survey of free-form object representation and recognition techniques. Computer Vision and Image Understanding 81 (2), 166-210.

Chen, Y., and Medioni, G., 1992. Object modelling by registration of multiple range images. Image and Vision Computing 10 (3), 145-155.

Chetverikov, D., 1991. Fast neighborhood search in planar point sets. Pattern Recognition Letters 12 (7), 409-412.

Chetverikov, D., Stepanov, D., and Krsek, P., 2005. Robust Euclidean alignment of 3D point sets: the trimmed iterative closest point algorithm. Image and Vision Computing 23 (3), 299-309.

Cohen, F.S., and Wang, J.Y., 1994. Part I: Modeling image curves using invariant 3-D object curve models – A path to 3-D recognition and shape estimation from image contours. IEEE Transactions on Pattern Analysis and Machine Intelligence 16 (1), 1-12.

Cunnington, S.J., and Stoddart, A.J., 1999. N-view point set registration: a comparison. British Machine Vision Conference, Nottingham, pp. 234-244.

Dalley, G., and Flynn, P., 2002. Pair-wise range image registration: a case study in outlier classification. Computer Vision and Image Understanding 87 (1-3), 104-115.

Danielsson, P.-E, 1980. Euclidean distance mapping. Computer Graphics and Image Processing 14 (3), 227-248.

D'Apuzzo, N., 2002. Measurement and modeling of human faces from multi images. International Archives of Photogrammetry, Remote Sensing and Spatial Information Sciences 34 (5), 241-246.

Dorai, C., Weng, J., and Jain, A.K., 1997. Optimal registration of object views using range data. IEEE Transactions on Pattern Analysis and Machine Intelligence 19 (10), 1131-1138.

Ebner, H., and Mueller, F., 1986. Processing of Digital Three Line Imagery using a generalized model for combined point determination. International Archives of Photogrammetry and Remote Sensing 26 (3/1), 212-222.

Ebner, H., Fritsch, D., Gillessen, W., and Heipke, C., 1987. Integration von bildzuordnung und objektrekonstruktion innerhalb der digitalen photogrammetrie. BuL 55 (5), 194-203.

Ebner, H., and Strunz, G., 1988. Combined point determination using Digital Terrain Models as control information. International Archives of Photogrammetry and Remote Sensing 27 (B11/3), 578-587.

Ebner, H., Strunz, G., and Colomina, I., 1991. Block triangulation with aerial and space imagery using DTM as control information. ACSM-ASPRS Annual Convention, Technical Papers, Baltimore, March 25-29, vol.5, pp. 76-85.

Ebner, H., and Ohlhof, T., 1994. Utilization of Ground Control Points for image orientation without point identification in image space. International Archives of Photogrammetry and Remote Sensing 30 (3/1), 206-211.

Eggert, D.W., Lorusso, A., and Fisher, R.B., 1997. Estimating 3-D rigid body transformations: a comparison of four major algorithms. Machine Vision and Applications 9 (5-6), 272-290.

Eggert, D.W., Fitzgibbon, A.W., and Fisher, R.B., 1998. Simultaneous registration of multiple range views for use in reverse engineering of CAD models. Computer Vision and Image Understanding 69 (3), 253-272.

Farin, G., 1997. Curves and surfaces for computer-aided geometric design. Fourth edition, Academic Press, USA, pp. 173-174.

Faugeras, O.D., and Hebert, M., 1986. The representation, recognition, and locating of 3-D objects. The International Journal of Robotics Research 5 (3), 27-52.

Feldmar, J., and Ayache, N., 1996. Rigid, affine and locally affine registration of free-from surfaces. International Journal of Computer Vision 18 (2), 99-119.

Fitzgibbon, A.W., 2001. Robust registration of 2D and 3D point sets. British Machine Vision Conference, Manchester, September 10-13, pp. 411-420.

Forkert, G., Kerschner, M., Prinz, R., and Rottensteiner, F., 1995. Reconstruction of free-formed spatial curves from digital images. International Archives of Photogrammetry and Remote Sensing 30 (5/W1), 163-168.

Gizzarelli, C., 2006. 'Weary Herakles': Looters vs. Archaeologists, http://www.bellaonline.com/articles/art28239.asp (accessed 6 April 2006).

Godin, G., Laurendeau, D., and Bergevin, R., 2001. A method for the registration of attributed range images. IEEE International Conference on 3D Digital Imaging and Modeling, Quebec, May 28 – June 1, pp. 179-186.

Golub, G.H., and Van Loan, C.F., 1980. An analysis of the total least squares problem. SIAM Journal on Numerical Analysis 17 (6), 883-893.

Greaves, T., 2005. Laser scanning shaves weeks from failure analysis of parking garage collapse. Spar ViewTM 3 (14), http://www.sparllc.com/archiveviewer.php?vol=03&num=14&file=vol03no14-01 (accessed August 2005).

Gruen, A., 1984. Adaptive least squares correlation – concept and first results. Intermediate Research Project Report to Heleva Associates, Inc., Ohio State University, Columbus, Ohio, March, pp. 1-13.

Gruen, A., 1985a. Adaptive least squares correlation: a powerful image matching technique. South African Journal of Photogrammetry, Remote Sensing and Cartography 14 (3), 175-187.

Gruen, A., 1985b. Adaptive kleinste Quadrate Korrelation und geometrische Zusatzinformationen. Vermessung, Photogrammetrie, Kulturtechnik, 9/85, 309-312.

Gruen, A., 1985c. Data processing methods for amateur photographs. Photogrammetric Record 11 (65), 567-579.

Gruen, A., and Baltsavias, E.P., 1987. High precision image matching for digital terrain model generation. Photogrammetria 42 (3), 97-112.

Gruen, A., and Baltsavias, E.P., 1988. Geometrically Constrained Multiphoto Matching. Photogrammetric Engineering and Remote Sensing 54 (5), 633-641.

Gruen, A., and Stallmann, D., 1991. High accuracy edge matching with an extension of the MPGC matching algorithm. International Conference on Industrial Vision Metrology, Winnipeg, July 11-12, SPIE vol. 1526, pp. 42-55.

Gruen, A., and Agouris, P., 1994. Linear feature extraction by least squares template matching constrained by internal shape forces. International Archives of Photogrammetry and Remote Sensing 30 (3/1), 316-323.

Gruen, A., and Li, H., 1996. Linear feature extraction with LSB-Snakes from multiple images. International Archives of Photogrammetry and Remote Sensing 31 (3B), 266-272.

Gruen, A., 1996. Least squares matching: a fundamental measurement algorithm. In: K. Atkinson (ed.), Close Range Photogrammetry and Machine Vision, Whittles, pp. 217-255.

Gruen, A., and Akca, D., 2005. Least squares 3D surface and curve matching. ISPRS Journal of Photogrammetry and Remote Sensing 59 (3), 151-174.

Greenspan, M., and Godin, G., 2001. A nearest neighbor method for efficient ICP. IEEE International Conference on 3D Digital Imaging and Modeling, Quebec, pp. 161-168.

Greenspan, M., and Yurick, M., 2003. Approximate K-D tree search for efficient ICP. IEEE International Conference on 3D Digital Imaging and Modeling, Banff, pp.442-448.

Guehring, J., 2001. Reliable 3D surface acquisition, registration and validation using statistical error models. IEEE International Conference on 3D Digital Imaging and Modeling, Quebec, May 28-June 1, pp. 224-231.

Gueziec, A., and Ayache, N., 1994. Smoothing and matching of 3-D space curves. International Journal of Computer Vision 12 (1), 79-104.

Helava, U.V., 1988. Object-space least-squares correlation. Photogrammetric Engineering and Remote Sensing 54 (6), 711-714.

Horn, B.K.P., 1987. Closed-form solution of absolute orientation using unit quaternions. Journal of the Optical Society of America A-4 (4), 629-642.

Horn, B.K.P., Hilden, H.M., and Negahdaripour, S., 1988. Closed-form solution of absolute orientation using orthonormal matrices. Journal of the Optical Society of America A-5 (7), 1128-1135.

Inan, J., 1981. Perge kazısı 1980 çalışmaları. III KST, DSİ Basım ve Foto Film İşletme Müdürlüğü Matbaası, Ankara, sayfa 43-48 (in Turkish).

Inan, J., 1992. Heraklesstatue vom Typus des "Herakles Fernese" aus Perge. Festschrift für Max Wegner Zum 90. Geburtstag, Bonn, pp. 223-232.

Jackins, C.L., and Tanimoto, S.L., 1980. Oct-trees and their use in representing three-dimensional objects. Computer Graphics and Image Processing 14 (3), 249-270.

Jaw, J.J., 2000. Control surface in aerial triangulation. International Archives of Photogrammetry and Remote Sensing 33 (B3), 444-451.

Johnson, A.E., and Kang, S.B., 1999. Registration and integration of textured 3D data. Image and Vision Computing 17 (2), 135-147.

Jokinen, O., and Haggren, H., 1998. Statistical analysis of two 3-D registration and modeling strategies. ISPRS Journal of Photogrammetry and Remote Sensing 53 (6), 320-341.

Jokinen, O., 1998. Area-based matching for simultaneous registration of multiple 3-D profile maps. Computer Vision and Image Understanding 71 (3), 431-447.

Jost, T., and Huegli, H., 2003. A multi-resolution ICP with heuristic closest point search for fast and robust 3D registration of range images. IEEE International Conference on 3D Digital Imaging and Modeling, Banff, pp. 427-433.

Karras, G.E., and Petsa, E., 1993. DEM matching and detection of deformation in close-range Photogrammetry without control. Photogrammetric Engineering and Remote Sensing 59 (9), 1419-1424.

Kishon, E., Hastie, T., and Wolfson, H., 1991. 3-D curve matching using splines. Journal of Robotic Systems 8 (6), 723-743.

Kraus, K., Ressl, C., and Roncat, A., 2006. Least squares matching for airborne laser scanner data. 5th International Symposium Turkish-German Joint Geodetic Days, Berlin, March 29-31, (only on CD-ROM).

Krishnan, S., Lee, P.Y., Moore J.B., and Venkatasubramanian, S., 2005. Global registration of multiple 3D point sets via optimization-on-a-manifold. Eurographics Symposium on Geometry Processing, Vienna, July 4-6, pp. 187-197.

Langis, C., Greenspan, M., and Godin, G., 2001. The parallel iterative closest point algorithm. IEEE International Conference on 3D Digital Imaging and Modeling, Quebec, pp. 195-204.

Lavallee, S., Szeliski, R., and Brunie, L., 1991. Matching 3-D smooth surfaces with their 2-D projections using 3-D distance maps. Geometric Methods in Computer Vision, San Diego, July 25-26, SPIE vol.1570, pp. 322-336.

Lu, F., and Milios, E., 1997. Globally consistent range scan alignment for environment mapping. Autonomous Robots 4 (4), 333-349.

Maas, H.G., 1994. A high-speed solid state camera system for the acquisition of flow tomography sequences for 3D least squares matching. International Archives of Photogrammetry and Remote Sensing 30 (5), 241-249.

Maas, H.G., and Gruen, A., 1995. Digital photogrammetric techniques for high resolution three dimensional flow velocity measurements. Optical Engineering 34 (7), 1970-1976.

Maas, H.G., 2000. Least-Squares Matching with airborne laserscanning data in a TIN structure. International Archives of Photogrammetry and Remote Sensing 33 (3A), 548-555.

Maas, H.G., 2001. On the use of pulse reflectance data for laserscanner strip adjustment. International Archives of Photogrammetry, Remote Sensing and Spatial Information Sciences 34 (Part 3/W4), 53-56.

Masuda, T., and Yokoya, N., 1995. A robust method for registration and segmentation of multiple range images. Computer Vision and Image Understanding 61 (3), 295-307.

Mitchell, H.L., and Chadwick, R.G., 1999. Digital Photogrammetric concepts applied to surface deformation studies. Geomatica 53 (4), 405-414.

Museum Rietberg, 2006. Exhibition Brochure.

Neugebauer, P.J., 1997. Reconstruction of real-world objects via simultaneous registration and robust combination of multiple range images. International Journal of Shape Modeling 3 (1-2), 71-90.

Norris, G., 2005. Jeppesen puts synthetic vision system on display. Flight International, 25-31 October, 9-10.

Okatani, I.S., and Deguchi, K., 2002. A method for fine registration of multiple view range images considering the measurement error properties. Computer Vision and Image Understanding 87 (1-3), 66-77.

Pajdla, T., and Van Gool, L., 1995. Matching of 3-D curves using semi-differential invariants. Proc. of IEEE International Conference on Computer Vision, Cambridge (MA), June 20-23, pp. 390-395.

Park, S.-Y., and Subbarao, M., 2003. A fast point-to-tangent plane technique for multi-view registration. IEEE International Conference on 3D Digital Imaging and Modeling, Banff, pp. 276-283.

Parsi, B.K., Jones, J.L., and Rosenfeld, A., 1991. Registration of multiple overlapping range images: Scenes without distinctive features. IEEE Transactions on Pattern Analysis and Machine Intelligence 13 (9), 857-871.

Pertl, A., 1984. Digital image correlation with the analytical plotter Planicomp C-100. International Archives of Photogrammetry and Remote Sensing 25 (3B), 874-882.

Peters, G.J., 1974. Interactive computer graphics application of the parametric bi-cubic surface to engineering design problems. In: R. Barnhill and R. Riesenfeld (Eds.), Computer Aided Geometric Design, Academic Press, pp. 259-302.

Pilgrim, L., 1996. Robust estimation applied to surface matching. ISPRS Journal of Photogrammetry and Remote Sensing 51 (5), 243-257.

Planitz, B.M., Maeder, A.J., and Williams, J.A., 2005. The correspondence framework for 3D surface matching algorithms. Computer Vision and Image Understanding 97 (3), 347-383.

Poli, D., Zhang, L., and Gruen, A., 2004. SPOT-5/HRS stereo images orientation and automated DSM generation. International Archives of Photogrammetry, Remote Sensing and Spatial Information Sciences 35 (B1), 421- 432 (and on DVD).

Postolov, Y., Krupnik, A., and McIntosh, K., 1999. Registration of airborne laser data to surfaces generated by Photogrammetric means. International Archives of Photogrammetry and Remote Sensing 32 (3/W14), 95-99.

Potmesil, M., 1983. Generating models of solid objects by matching 3D surface segments. International Joint Conference on Artificial Intelligence, Karlsruhe, August 8-12, pp. 1089-1093.

Pottmann, H., Leopoldseder, S., and Hofer, M., 2004. Registration without ICP. Computer Vision and Image Understanding 95 (1), 54-71.

Pulli, K., Duchamp, T., Hoppe, H., McDonald, J., Shapiro, L., and Stuetzle, W., 1997. Robust meshes from multiple range maps. IEEE International Conference on 3D Digital Imaging and Modeling, Ottawa, pp. 205-211.

Pulli, K., 1999. Multiview registration for large data sets. IEEE International Conference on 3D Digital Imaging and Modeling, Ottawa, October 4-8, pp. 160-168.

Rogers, D.F., and Adams, J.A., 1976. Mathematical elements for computer graphics. McGraw-Hill Book Company, London, pp. 116-155.

Rose, M., and Acar, O., 1995. Turkey's war on the illicit antiquities trade. Archaeology 48 (2), 45-56.

Rosenholm, D., and Torlegard, K., 1988. Three-dimensional absolute orientation of stereo models using Digital Elevation Models. Photogrammetric Engineering and Remote Sensing 54 (10), 1385-1389.

Roth, G., 1999. Registering two overlapping range images. IEEE International Conference on 3D Digital Imaging and Modeling, Ottawa, October 4-8, pp. 191-200.

Rusinkiewicz, S., and Levoy, M., 2001. Efficient variants of the ICP algorithm. IEEE International Conference on 3D Digital Imaging and Modeling, Quebec, May 28 – June 1, pp. 145-152.

Sauerbier, M., Kunz, M., Fluehler, M., and Remondino, F., 2004. Photogrammetric reconstruction of adobe architecture at Tucume, Peru. International Archives of Photogrammetry, Remote Sensing and Spatial Information Sciences 36 (5/W1), (only on CD-Rom).

Scaioni, M., and Forlani, G., 2003. Independent model triangulation of terrestrial laser scanner data. International Archives of the Photogrammetry, Remote Sensing and Spatial Information Sciences 34 (5/W12), 308-313.

Schaffrin, B., and Felus, Y.A., 2003. On total least-squares adjustment with constraints. In Proceedings of IUGG General Assembly, Sapporo, Japan, June 30-July 11.

Schenk, T., Krupnik, A., and Postolov, Y., 2000. Comparative study of surface matching algorithms. International Archives of Photogrammetry and Remote Sensing 33 (B4), 518-524.

Schoenemann, P.H., and Carroll, R.M., 1970. Fitting one matrix to another under choice of a central dilation and a rigid motion. Psychometrika 35 (2), 245-255.

Schwartz, J.T., and Sharir, M., 1987. Identification of partially obscured objects in two and three dimensions by matching noisy characteristic curves. The International Journal of Robotics Research 6 (2), 29-44.

Sharp, G.C., Lee, S.W., and Wehe, D.K., 2004. Multiview registration of 3D scenes by minimizing error between coordinate frames. IEEE Transactions on Pattern Analysis and Machine Intelligence 26 (8), 1037-1050.

Sternberg, H., Kersten, Th., Jahn, I., and Kinzel, R., 2004. Terrestrial 3D laser scanning – data acquisition and object modeling for industrial as-built documentation and ar-chitectural

applications. International Archives of the Photogrammetry, Remote Sensing and Spatial Information Sciences 35 (B7), 942-947.

Stoddart, A.J., and Hilton, A., 1996. Registration of multiple point sets. IEEE International Conference on Pattern Recognition, Vienna, pp. B40- 44.

Szeliski, R., and Lavallee, S., 1996. Matching 3-D anatomical surfaces with non-rigid deformations using octree-splines. International Journal of Computer Vision 18 (2), 171-186.

Turk, G., and Levoy, M., 1994. Zippered polygon meshes from range images. Proc. of ACM SIGGRAPH'94, Orlando (Florida), July 24-29, pp. 311-318.

Xu, Z., and Li, Z., 2000. Least median of squares matching for automated detection of surface deformations. International Archives of Photogrammetry and Remote Sensing 33 (B3), 1000-1007.

Vanden Wyngaerd, J., and Van Gool, L., 2003. Combining texture and shape for automatic crude patch registration. IEEE International Conference on 3D Digital Imaging and Modeling, Banff, Canada, October 6-10, pp. 179-186.

Wang, J.Y., and Cohen, F.S., 1994. Part II: 3-D object recognition and shape estimation from image contours using B-splines, shape invariant matching, and Neural Networks. IEEE Transactions on Pattern Analysis and Machine Intelligence 16 (1), 13-23.

Wang, J., and Shan, J., 2005. Lidar data management with 3-D Hilbert space-filling curve. ASPRS Annual Meeting, Baltimore, March 7-11, (only on CD-ROM).

Waser, L.T., Küchler, M., Baltsavias, E., Feldmeyer-Christe, E., Eisenbeiss, H., Ginzler, C., Three, P., and Zhang, L., 2007. Assessing changes of forest area and shrub encroachment in a mire ecosystem using digital surface models and CIR-aerial images. Remote Sensing of Environment (accepted for publication).

Weik, S., 1997. Registration of 3-D partial surface models using luminance and depth information. IEEE International Conference on Recent Advances in 3D Digital Imaging and Modeling, Ottawa, Canada, May 12-15, pp. 93-100.

Wendt, A., and Heipke, C., 2006. Simultaneous orientation of brightness, range and intensity images. International Archives of Photogrammetry, Remote Sensing and Spatial Information Sciences 36 (5), 315-322.

Williams, J.A., Bennamoun, M., and Latham, S., 1999. Multiple view 3D registration: A review and a new technique. IEEE International Conference on Systems, Man, and Cybernetics, Tokyo, October 12-15, pp. 497-502.

Williams, J., and Bennamoun, M., 2001. Simultaneous registration of multiple corresponding point sets. Computer Vision and Image Understanding 81 (1), 117-142.

Wrobel, B., 1987. Facets Stereo Vision (FAST Vision) – a new approach to computer stereo vision and to digital photogrammetry. Proceedings of ISPRS intercommission conference on fast processing of photogrammetric data, Interlaken, Switzerland, June 2-4, pp. 231-258.

Yoshida, K., and Saito, H., 2002. Registration of range images using texture of high-resolution color images. IAPR Workshop on Machine Vision Applications (MVA'02), Nara, December 11-13, pp. 150-153.

Zalmanson, G.H., and Schenk, T., 2001. Indirect orientation of pushbroom sensors with 3-D free-form curves. Joint Workshop of ISPRS on High Resolution Mapping from Space, Hannover, September 19-21 (on CD-ROM).

Zhang, Z., 1994. Iterative point matching for registration of free-form curves and surfaces. International Journal of Computer Vision 13 (2), 119-152.

Zhang, L., and Gruen, A., 2004. Automatic DSM Generation from Linear Array Imagery Data. International Archives of Photogrammetry, Remote Sensing and Spatial Information Sciences 35 (B3), 128-133.

Zhang, L., Kocaman, S., Akca, D., Kornus, W., and Baltsavias, E., 2006. Test and performance evaluation of DMC images and new methods for their processing. ISPRS Commission I Symposium, Paris, July 3-6, (only on CD-ROM).

ACKNOWLEDGEMENTS

CURRICULUM VITAE

M.Sc. Mehmet Devrim Akca
Institute of Geodesy and Photogrammetry
ETH Zurich
HIL D52.3
Wolfgang-Pauli-Str. 15
8093 Zurich

Personal
Date of birth: May 27, 1975
Nationality: Turkish

Formation
2003 – 2007: Ph.D. degree, Institute of Geodesy and Photogrammetry, ETH Zurich, Switzerland, Ph.D. Thesis: Least squares 3D surface matching.

2000 – 2002: Ph.D. student (not finished), Department of Geodesy and Photogrammetry, Istanbul Technical University, Turkey.

1997 – 2000: M.Sc. degree, Department of Geodesy and Photogrammetry, Karadeniz Technical University, Trabzon, Turkey, M.Sc. Thesis: Modeling environmental data using GIS: Case study of Trabzon - Degirmendere Valley.

1993 – 1997: B.Sc. degree, Department of Geodesy and Photogrammetry, Karadeniz Technical University, Trabzon, Turkey.

1989 – 1993: Cadastre technician degree, Anatolian Land Registry and Cadastre High School, Ankara, Turkey.

Employment
2003 – 2007: Research assistant, Chair of Photogrammetry and Remote Sensing, Institute of Geodesy and Photogrammetry, ETH Zurich, Switzerland.

2002 – 2003: Academic guest, Chair of Photogrammetry and Remote Sensing, Institute of Geodesy and Photogrammetry , ETH Zurich, Switzerland.

2001 – 2002: Research assistant, Division of Photogrammetry, Department of Geodesy and Photogrammetry, Istanbul Technical University, Turkey.

2000 – 2001: Research and teaching assistant, Department of Geodesy and Photogrammetry, Ondokuz Mayis University, Samsun, Turkey.

1997 – 2000: Surveying engineer, Cadastre Office, Macka (Trabzon), Turkey.

1993 – 1994: Cadastre technician, Cadastre Office, Yenice (Zonguldak), Turkey.

Awards and Honors
- Listing in Marquis Who's Who in Science and Engineering, 9th edition, 2006-2007.
- The ISPRS Prize for Best Papers by Young Authors, 20th ISPRS Congress, 2004.
- Doctoral fellowship, Scientific and Technical Council of Turkey (TUBITAK), 2001-2002.
- Honorary degree in B.Sc. graduation (First rank of the department), Karadeniz Technical University, Turkey, 1997.

Publications
17 publications at conferences and journals and 6 technical reports since 2003. A complete list of publications is available at
http://www.photogrammetry.ethz.ch/general/persons/devrim_publ.html

Languages
Native language: Turkish
Foreign languages: English, German